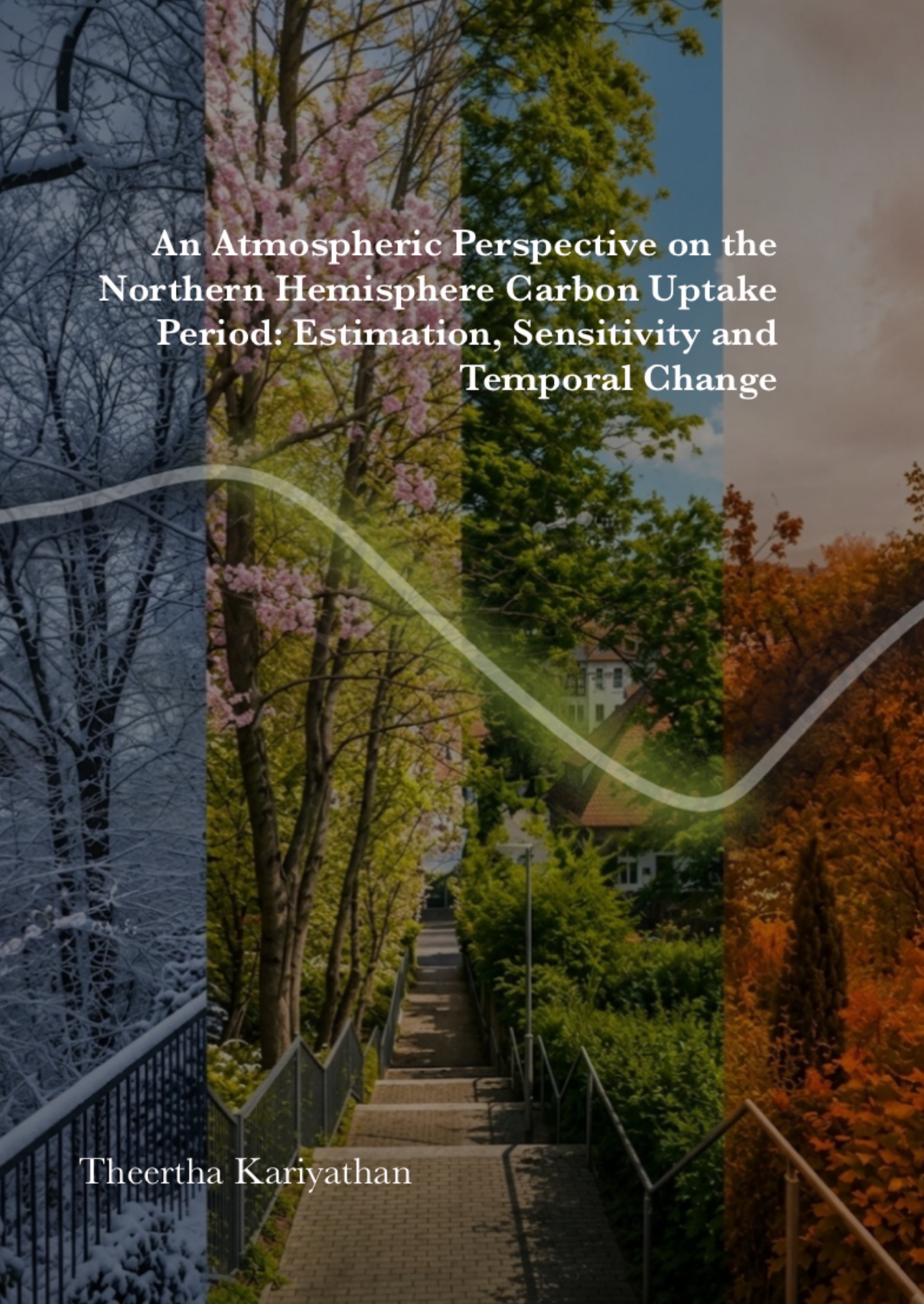


An Atmospheric Perspective on the Northern Hemisphere Carbon Uptake Period: Estimation, Sensitivity and Temporal Change

Theertha Kariyathan

Propositions

1. Atmospheric CO_2 records best indicate long-term ecosystem change when carbon uptake termination exhibits the strongest trends.
   (this thesis)
2. Reproducing seasonal carbon dynamics is an essential benchmark for carbon-cycle model evaluation.
   (this thesis)
3. Expanding atmospheric CO_2 observation networks is currently more important than developing increasingly complex carbon-cycle models.
4. Understanding multiple disciplines moderately well contributes more to scientific research than mastering a single discipline exceptionally well.
5. Parallel pursuits outside academia strengthen resilience during long-term academic pursuits.
6. Individual carbon reduction cannot be an effective climate solution while nations continue environmentally destructive wars.

Propositions belonging to the thesis, entitled

An Atmospheric Perspective on the Northern Hemisphere Carbon Uptake Period: Estimation, Sensitivity, and Temporal Change

Theertha Kariyathan
Wageningen, 19 November 2026

An Atmospheric Perspective on the Northern Hemisphere Carbon Uptake Period: Estimation, Sensitivity, and Temporal Change

Theertha Kariyathan

Thesis committee

Promotors:
Prof.Dr Wouter Peters
Professor in Meteorology and Air Quality
Wageningen University & Research

Prof.Dr Julia Marshall
Leipzig Institute for Meteorology,
Leipzig University, Germany

Prof.Dr Ana Bastos
Institute for Earth System Science and Remote Sensing,
Leipzig University, Germany

Other members:
Prof.Dr *ir.* Gert-Jan Nabuurs, Wageningen University & Research, Netherlands
Dr Ute Karstens, Lund University, Sweden
Prof. Dr Anita Ganesan, University of Bristol, United Kingdom
Dr Gerbrand Koren, Utrecht University,

This research was conducted under the auspices of the Graduate School for
Socio-Economic and Natural Sciences of the Environment (SENSE)

An Atmospheric Perspective on the Northern Hemisphere Carbon Uptake Period: Estimation, Sensitivity, and Temporal Change

Theertha Kariyathan

Thesis
submitted in fulfilment of the requirements for the degree of doctor
at Wageningen University
by the authority of the Rector Magnificus,
Prof. Dr C. Kroeze,
in the presence of the
Thesis Committee appointed by the Academic Board
to be defended in public
on Thursday 19 November 2026
at 3:30 p.m. in the Omnia Auditorium.

Theertha Kariyathan
An Atmospheric Perspective on the Northern Hemisphere Carbon Uptake Period: Estimation, Sensitivity, and Temporal Change
104 pages.

PhD thesis, Wageningen University, Wageningen, the Netherlands (2026)
With references, with summary in English.

https://doi.org/10.18174/681265

Acknowledgements

It is often said that a PhD is not just an academic journey, but a deeply personal one, shaped as much by the people around us as by the questions we seek to answer. In that spirit, I would like to express my heartfelt gratitude to all those who have supported, guided, and stood by me throughout this journey.

First and foremost, I am profoundly grateful to my supervisors. To Prof. Wouter Peters, thank you for being a constant guiding force. The intense, pen-and-paper discussions we shared during my time at Wageningen remain some of the most intellectually stimulating moments of my PhD, shaping not only my research but also my curiosity as a scientist.

To Dr. Julia Marshall, I owe my sincere thanks for your unwavering support from the very beginning of my PhD to its completion. Your thoughtful feedback and steady encouragement have been invaluable at every stage of this journey. To Dr. Ana Bastos, thank you for giving me a research home and a sense of structure during my PhD. Your guidance came at crucial moments, helping me navigate both the scientific and personal challenges that accompanied this path. To Prof. Markus Reichstein, I am deeply grateful for ensuring a smooth transition as I began this journey in a new country. Your support during those initial, often uncomfortable phases meant more than I can fully express and gave me the confidence to find my footing.

Beyond academia, my deepest gratitude belongs to my family. To Achan, Amma, and Vava - your unconditional love and sacrifices have been the foundation of everything I have achieved. You have shaped me into the independent woman I am today, and I carry your values with me in every step I take. To my husband, Ishwar, my partner in every sense of the word. Thank you for being my greatest pillar of strength. You believed in me even during my lowest moments, often more than I believed in myself. Your unwavering support, patience, and love has literally carried me through this journey.

To Eldho, from IISER days to Jena, you have been a constant presence through both academic and life struggles. Thank you for always being the person I could turn to,

and for somehow always finding the right people and moments to remind me to pause, breathe, and enjoy life amidst the chaos. Finally, I extend my gratitude to all my friends and extended family who have supported me in ways big and small. Each conversation, gesture, and moment of encouragement has contributed to this journey more than I can fully acknowledge.

As I look back, I realize that this thesis is not just a culmination of my work, but a collective reflection of everyone who has stood beside me - lifting, guiding, and believing in me along the way.

Summary

Terrestrial ecosystems play a crucial role in regulating atmospheric CO_2 concentration by absorbing a substantial fraction of anthropogenic emissions. This net sink behaviour emerges from the balance between the two dominant terrestrial carbon fluxes: gross primary production (GPP), the uptake of CO_2 through photosynthesis, and total ecosystem respiration (TER), the release of CO_2 from autotrophic and heterotrophic respiration; their difference defines the net ecosystem exchange (NEE). When GPP exceeds TER, photosynthetic carbon uptake exceeds respiratory CO_2 release, and ecosystems function as a net sink of atmospheric CO_2. This period of the year is referred to as the Carbon Uptake Period (CUP). The timing and duration of the CUP are influenced by environmental conditions such as temperature, radiation, and water availability, which regulate the seasonal dynamics of photosynthesis and respiration. In addition to these climatic controls, episodic disturbances and anomalies, such as droughts, heatwaves, or wildfire events, can substantially alter the seasonal balance between uptake and release. By integrating net CO_2 exchange between the land biosphere and the atmosphere, the CUP provides a process-relevant indicator of ecosystem carbon balance and a metric for assessing ecosystem responses to climate variability and long-term change. CUP timing can be estimated from long-term atmospheric CO_2 records, characterised by the annual rise and decline in CO_2 levels driven by ecosystem transitions between net carbon uptake and release. However, extracting reliable CUP timing from atmospheric observations remains challenging, as measurements integrate broad source regions and are influenced by transport, synoptic variability, and methodological uncertainties associated with time-series analysis. This highlights the need to improve CUP estimation methods and better constrain how they reflect changes in surface fluxes.

The overall objective of this thesis is to improve understanding of changes in CUP in the Northern Hemisphere. To achieve this, we primarily use atmospheric CO_2 observations, first developing improved methods to estimate CUP from these records, then assessing the influence of atmospheric transport on these estimates, and finally diagnosing recent changes in CUP timing and their ecological drivers. The thesis addresses three central questions: (1) how CUP metrics can be robustly estimated from atmospheric CO_2 time series, (2) how atmospheric transport affects the relationship

between atmospheric signals and surface carbon fluxes, and (3) what recent changes in CUP timing reveal about regional ecosystem responses to climate variability.

The first chapter of this thesis focuses on improving the estimation of CUP timing from atmospheric CO_2 time series, which are discrete, noisy, and often contain gaps. We developed the Ensemble of the First Derivative (EFD) method, which reduces biases associated with the choice of curve-fitting algorithms and decreases the uncertainty in the estimated CUP metrics compared with traditional proxy definitions, such as the zero-crossing point of the detrended seasonal cycle. The method generates an ensemble of plausible fits to the time series and estimates CUP timing from the first derivative of these fits using a threshold defined relative to the minimum of the derivative. The threshold is selected such that it minimizes uncertainty across the ensemble. When evaluated using two different curve-fitting frameworks, the EFD approach shows that threshold-based CUP estimates exhibit substantially lower uncertainty than traditional zero-crossing metrics. Moreover, while earlier derivative-based approaches (Barlow et al., 2015) relied on relatively high thresholds (25% of the seasonal minimum of the first derivative) to identify the onset of the CUP, the reduced uncertainty achieved with the EFD framework allows the use of a lower threshold (15%). This results in CUP estimates that include a larger portion of the early-season carbon uptake period.

The second chapter of the thesis investigates how atmospheric transport affects the relationship between the CUP derived from atmospheric CO_2 observations (CUP_{MR}) and that derived from NEE fluxes (CUP_{NEE}). Using atmospheric transport model simulations with prescribed surface flux modifications, we assess how changes in surface carbon exchange propagate through the atmosphere and are reflected in the seasonal CO_2 signals observed at monitoring sites. The results show that interannual variability (IAV) in atmospheric transport contributes substantially to variability in the observed CUP_{MR} signals. In addition, atmospheric mixing strongly dampens surface signals: at widely studied sites such as Mauna Loa, Utqiaġvik (formerly Barrow), and Alert, only about 50% of the imposed surface changes are reflected in the CUP derived from atmospheric CO_2 observations, due to the spatial integration of asynchronous regional flux variations.

The third chapter of the thesis applies the developed framework to investigate recent changes in CUP timing across the Northern Hemisphere. Combining atmospheric CO_2 observations with surface flux estimates from atmospheric inversions and data-driven products, the study analyzes spatial and temporal patterns in CUP timing for 2001–2021. The results show a robust and spatially coherent advancement of CUP_{MR} onset across many high-latitude sites ($\approx$ 60°–90° N), with a mean trend of -2.5 ± 0.27 days per decade. Analysis of regionally aggregated CUP_{NEE} metrics indicates that the observed advancement in CUP_{MR} onset originates primarily from Eurasian boreal ecosystems, while North American regions exhibit weaker or inconsistent trends in CUP_{NEE} onset.

Regions with advancing CUP_{NEE} onset are characterized mainly by earlier GPP, with TER also advancing in similar ammounts, suggesting the an increase in magnitude of early season GPP. These patterns are consistent with stronger spring warming across Eurasia, suggesting that earlier photosynthetic activation in Eurasian boreal ecosystems likely influences the observed advancement of CUP onset in high-latitude atmospheric CO_2 records.

Overall, this thesis shows that atmospheric CO_2 observations are a powerful tool for diagnosing large-scale changes in the timing of terrestrial carbon exchange, while also highlighting limitations arising from atmospheric transport and spatial signal integration. The work contributes methodological advances and new insights into the seasonal dynamics of the terrestrial carbon cycle. By improving the reliability of CUP estimates derived from atmospheric observations and clarifying the relationship between atmospheric signals and surface fluxes, it provides a framework for diagnosing seasonal changes in ecosystem carbon exchange at large spatial scales. Together, these advances strengthen the potential of atmospheric CO_2 observations to constrain the timing of the terrestrial carbon fluxes.

Contents

	Page
Acknowledgements	v
Summary	vii
Contents	xi
Chapter 1 Introduction	1
Chapter 2 Reducing errors on estimates of the carbon uptake period based on time series of atmospheric CO_2	21
Chapter 3 Limitations in the use of atmospheric CO_2 observations to directly infer changes in the length of the biospheric carbon uptake period	45
Chapter 4 Advancing onset of the carbon uptake period revealed by high-latitude CO_2 records, linked to Eurasian regions	69
Chapter 5 Synthesis	93
References	105

Chapter 1

Introduction

1.1 The global carbon cycle

The global carbon cycle is the continuous movement of carbon among four key reservoirs: the atmosphere, the oceans, terrestrial ecosystems, and geological stores (Ciais et al., 2013). These reservoirs differ widely in size and turnover time: atmospheric carbon is small and cycles rapidly, the terrestrial biosphere exchanges carbon on seasonal to centennial timescales, and the ocean spans processes from rapid air–sea exchange to slow deep-ocean sequestration (Ciais et al., 2013). The geological reservoir, including sedimentary rocks and fossil carbon deposits, represents the largest and slowest component of the cycle, with turnover times exceeding millions of years, although erosion and riverine fluxes may have been altered by human land-use changes (Raymond & Cole, 2003). Since the onset of the Industrial Era, the extraction and combustion of fossil fuels have transferred large quantities of carbon from this slow geological domain into the fast-cycling atmosphere–ocean–land system, creating an unprecedented anthropogenic perturbation to the carbon cycle (Ciais et al., 2013).

Anthropogenic emissions, arising primarily from fossil fuel combustion and land-use change (land-use, land-use change, and forestry), now add carbon to the atmosphere at rates far exceeding those of natural processes (Archer et al., 2009). Over the past decade (2014–2023), average anthropogenic carbon emissions (fossil and land use) reached approximately 10.8 ± 0.9 gigatons of carbon per year (GtC/yr), as reported in the recent Global Carbon Budget (Friedlingstein et al., 2025). Of the total emissions, 90% were from fossil CO_2 emissions and 10% from land-use change. During this period, terrestrial ecosystems absorbed approximately 3.2 ± 0.9 GtC/yr and the ocean sequestered 2.9 ± 0.4 GtC/yr (Fig. 1.1). Together, these sinks offset a substantial fraction of anthropogenic CO_2 emissions, thereby moderating the rate of atmospheric CO_2 increase. The land sink is highly variable from year to year, primarily in response to climate variability and disturbances, whereas the ocean sink is comparatively more stable and governed by physicochemical processes such as solubility and ocean circulation. Looking over the longer historical period from 1850 to 2023, roughly one third of the cumulative anthropogenic emissions originated from land-use change, with the remaining two thirds arising from fossil fuel combustion. Since around 1960, however, fossil fuel emissions have increased dramatically, whereas land-use change emissions have remained comparatively stable, leading to a declining relative contribution of land-use change to the total anthropogenic emissions.

The anthropogenic inputs have led to a sharp and persistent rise in atmospheric CO_2 levels. As a long-lived greenhouse gas (atmospheric gases that trap heat by absorbing and re-emitting infrared radiation), CO_2 absorbs outgoing longwave radiation, strengthening the Earth's radiative forcing and thereby contributing to warming (Forster et al., 2021). The continued rise in CO_2 enhances the natural greenhouse effect, thereby contributing

to global warming. Observations from the NOAA Global Monitoring Laboratory indicate that CO_2 alone accounts for roughly 80% of the total radiative forcing from anthropogenic greenhouse gases since 1990 (Lindsey, 2025). Globally averaged marine surface annual mean data from NOAA's Global Monitoring Laboratory indicate that atmospheric CO_2 concentrations reached 425.64 ± 0.09 parts per million (ppm) in 2025, (Lan et al., 2026), up from 278 ppm in the pre-industrial era (∼1750) (Gulev et al., 2021). The observed atmospheric CO_2 signal represents the superposition of fluxes from multiple carbon cycle components, including land biosphere exchange, ocean–atmosphere fluxes, and anthropogenic emissions. The long-term increase in atmospheric CO_2 reflects an imbalance between anthropogenic emissions and natural carbon sinks, particularly those on land (Friedlingstein et al., 2025). The terrestrial carbon budget plays a central role in modulating this imbalance and is governed by two dominant processes: the uptake of CO_2 through photosynthesis and its release back to the atmosphere via plant and microbial respiration. The balance between these opposing fluxes gives rise to both the net land carbon sink and largely drive the seasonal cycle in atmospheric CO_2 (more pronounced in the Northern Hemisphere)(Keeling et al., 1996). During spring and summer, enhanced photosynthetic activity leads to a drawdown of atmospheric CO_2, whereas in autumn and winter, reduced photosynthesis and continued respiration result in net CO_2 release. Superimposed on this seasonal cycle, interannual variability in the terrestrial carbon sink, driven by climate anomalies and disturbances such as temperature extremes, droughts, fires, and large-scale modes of variability like El Niño–Southern Oscillation, further modulates atmospheric CO_2 (e.g. Li et al., 2022; Luo & Keenan, 2022).

Alongside, the increasing emissions, an increasing trend in the global net land CO_2 sink since the 1980s has been suggested both by atmospheric inversions (e.g., Peylin et al. (2013)) and by dynamic global vegetation models (e.g.,Friedlingstein et al. (2019)). The terrestrial ecosystem carbon uptake has grown from roughly 1.2 ± 0.5 GtC/yr in the 1960s to about 3.2 ± 0.9 GtC/yr in the last decade (2014–2023) (Friedlingstein et al., 2025). The observed increase in land carbon uptake is attributed mainly to elevated atmospheric CO_2 enhancing photosynthesis (the CO_2 fertilization effect (Prentice et al., 2001; Piao et al., 2009; Schimel et al., 2015; Chen et al., 2022). While global-scale analyses identify CO_2 fertilization as a dominant driver of the increase in the terrestrial biospheric sink, its magnitude varies among biomes and is often constrained by nutrient availability (Schimel et al., 2015; Wang et al., 2020). Increases in nitrogen deposition, arising from fossil fuel combustion, agriculture, and rock-derived inputs, can reduce nutrient limitation (Huntzinger et al., 2017), enabling ecosystems to more fully respond to elevated CO_2, strengthening the land carbon sink. However, recent studies (e.g. Kou-Giesbrecht et al., 2025; O'Sullivan et al., 2019) show that nitrogen deposition contributes only marginally to enhancing CO_2 fertilisation and does not substantially strengthen the contemporary terrestrial carbon sink.

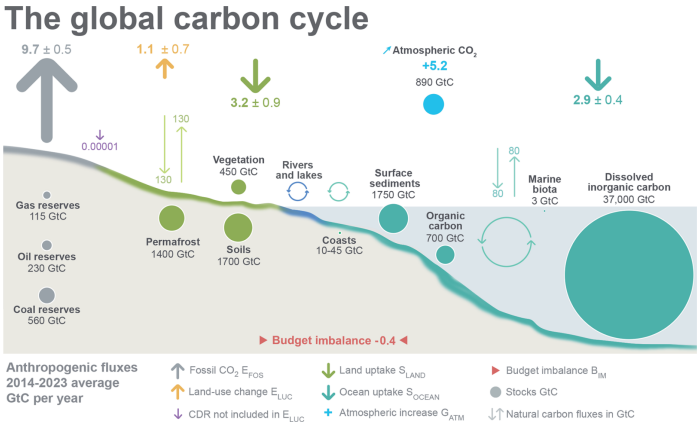


Figure 1.1: The global carbon budget, illustrating natural fluxes, carbon reservoirs, and the contributions of anthropogenic emissions, averaged over the decade 2014–2023, as reported by Friedlingstein et al. (2025). Fluxes are expressed in gigatonnes of carbon per year (GtC/yr), and carbon reservoirs are given in gigatonnes of carbon (GtC).

One third of the global terrestrial carbon sink can be attributed to the terrestrial ecosystems in the Northern Hemisphere (Liu et al., 2025b). Recent assessments emphasise that protecting and maintaining the sink strength of northern forests is critical for keeping warming within the Paris Agreement limits (well below 2° C, with efforts to limit warming to 1.5° C above pre-industrial level) (Masson-Delmotte et al., 2021), as these forests currently offset a substantial fraction of global emissions and could continue to do so if not degraded by climate stress or land-use change (Riany et al., 2024). At the same time, high-latitude ecosystems also contain vast soil carbon pools that are vulnerable to thawing permafrost and increasing disturbance, so the long-term fate of the Northern Hemisphere sink remains uncertain (Schuur et al., 2015). Boreal ecosystems alone store more than 30% of all carbon present in the terrestrial biome in biomass and soils (Kasischke, 2000), making them especially sensitive to fire-driven carbon loss (Zhao et al., 2021). Fire activity in these regions has increased markedly: for example, the Canadian boreal forest has experienced a doubling of annual burned area since the 1970s, with fire seasons now starting earlier and lasting longer (Hanes et al., 2019). Analyses show that boreal wildfires now offset a significant fraction of the region's annual carbon uptake, with some fire years resulting in net carbon source conditions over vast areas (Walker et al., 2019).

Among the processes that contribute to the increased sink, recent shifts in seasonal phenology also play an important role. In these high-latitude ecosystems, where

temperature is often a limiting factor for photosynthetic activity, rising temperatures trigger earlier snowmelt, leading to an advanced start of photosynthetic activity and an associated lengthening of the growing season (Keenan et al., 2014; Black et al., 2000). However, a longer growing season may not necessarily result in an increase in net carbon uptake. Earlier and more vigorous vegetation growth can elevate evapotranspiration, thereby depleting soil moisture and increasing the risk of drought stress during the latter part of the growing season (Buermann et al., 2018; Barnett et al., 2005; Lian et al., 2020).

Moreover, the extent to which ecosystems continue to absorb carbon during warmer summer conditions is heavily influenced by water availability. Elevated temperatures alone do not guarantee higher carbon uptake; when accompanied by water scarcity, they may instead constrain photosynthesis and enhance stress responses, particularly in forests located in regions increasingly affected by summer aridity (Mirabel et al., 2023; Zeng et al., 2023). In such areas, net CO_2 uptake may decline or even reverse, resulting in a net release of carbon to the atmosphere (Liu et al., 2025b). During autumn, rising temperatures have been shown to prolong photosynthetic activity in some ecosystems, particularly in evergreen needleleaf forests where warming can delay declines in carbon assimilation (Stinziano & Way, 2017). However, this extended activity does not necessarily equate to greater carbon sequestration. Warmer autumns can also stimulate microbial and root respiration, increasing CO_2 emissions from the soil (Schindlbacher et al., 2012; Wang et al., 2014; Niu et al., 2024), potentially offsetting the additional carbon gained through photosynthesis. In some cases, this can result in a net loss of carbon from terrestrial ecosystems (Bond-Lamberty et al., 2018; Liu et al., 2020). Recent studies suggest that the global soil respiration has increased in recent decades in association with warming, and that this response is widespread across biomes (Bond-Lamberty et al., 2018; Nissan et al., 2023).

Determining the timing of the transition between terrestrial carbon uptake and release is a critical and open issue in carbon cycle science. Ongoing climate change not only modifies the total amount of carbon that ecosystems can absorb annually, but also shifts the seasonal pattern of carbon fluxes (Liu et al., 2025b).

1.2 Ecosystem fluxes and their drivers

Terrestrial carbon exchange is dominated by two large and tightly coupled ecosystem fluxes: Gross Primary Production (GPP), the total carbon fixed through photosynthesis, and Total Ecosystem Respiration (TER), the combined CO_2 release from autotrophic (plant) and heterotrophic (microbial) respiration. The difference between GPP and TER

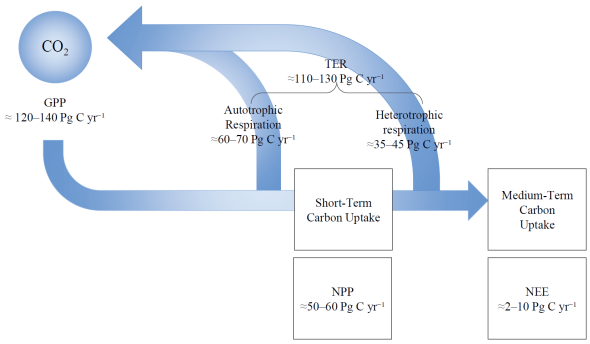


Figure 1.2: Net ecosystem exchange (NEE) and its component fluxes, adapted from Watson et al. (2000). The gross primary productivity (GPP) via photosynthesis is offset by autotrophic respiration, resulting in Net Primary Productivity (NPP) and representing short-term carbon uptake. Further CO_2 release occurs through heterotrophic respiration – decomposition of litter and soil organic matter, which reduces NPP to NEE, representing medium-term carbon uptake. Flux values are indicative of recent global terrestrial carbon budget estimates (e.g. Zhao & Zhu, 2025; Ciais et al., 2021) and are rounded to emphasise relative magnitudes rather than exact annual totals.

is defined as the Net Ecosystem Exchange (NEE) (Fig. 1.2, Eq. 1.1),

$$NEE = TER - GPP \tag{1.1}$$

NEE is the primary metric used to quantify whether an ecosystem behaves as a net carbon sink or source on daily to annual timescales. By this convention, negative NEE values indicate net CO_2 uptake by the ecosystem (i.e., $GPP > TER$), while positive values denote net CO_2 release ($TER > GPP$). In the Northern Hemisphere, high-latitude ecosystems become NEE sinks when plants and soils respond to warming temperatures and increasing day lengths in spring by storing more carbon than they release on average (Endsley et al., 2022).

GPP represents the largest carbon flux within the biosphere (Li et al., 2023). Estimates of global mean annual GPP vary widely, ranging from approximately 112 to 169 PgC/yr across different studies (Anav et al., 2015). Satellite-based optical remote sensing, combined with data-driven upscaling approaches such as FLUXCOM, yields global GPP estimates in the range of approximately 110–150 PgC yr^{-1} (Jung et al., 2020). More recent approaches that rely on CO_2 diffusion-tracers, such as carbonyl sulfide (COS), suggest a contemporary global GPP of roughly 157 ± 8.5 PgC/yr (Lai et al., 2024). TER closely balances global GPP. Earlier studies have estimated global annual TER to be approximately 100–110 PgC/yr (Jung et al., 2011). More recent work

employing improved models that incorporate a broader suite of key environmental drivers suggests a higher global TER, in the range of 117–125 PgC/yr (Zhao & Zhu, 2025). These fluxes exhibit pronounced spatial variation. For example, both observational data and model simulations reveal strong latitudinal gradients in annual GPP, with values increasing from cold tundra and arid desert biomes toward warmer temperate regions and humid tropical rainforests (Li et al., 2023).

These fluxes respond in distinct and often nonlinear ways to environmental variability. Understanding the changes and mechanisms that govern these processes is essential for interpreting the seasonal and interannual behaviour of terrestrial CO_2 fluxes and their sensitivity to ongoing climate change.

At the global scale, the increase in GPP is largely attributed to the CO_2 fertilisation effect, which provides the largest contribution to the observed global GPP trend (65.73%) (Sun et al., 2018). However, other environmental drivers are also important, particularly in shaping regional variability. While CO_2 increases are globally uniform, climate factors such as temperature, radiation, and soil moisture vary spatially and play a key role in regulating GPP at regional scales (Sun et al., 2018). The relationships between GPP and climate factors are complex, and the annual cycle of GPP is phase-locked with the seasonal evolution of the regional climate. An optimal combination of environmental conditions (e.g., appropriate temperature, sufficient light, and available soil water) generates high production. Conversely, productivity declines when any one of these factors becomes limiting (Li et al., 2023). Plant photosynthesis and ecosystem productivity generally increase with temperature until reaching an optimum, beyond which rising temperatures can lead to photosynthetic inhibition (Shi et al., 2025; Wang et al., 2024). Enhanced GPP under warm conditions also depends on adequate soil moisture; warming tends to boost plant photosynthesis during wetter periods when water availability is sufficient (Quan et al., 2019). Liu et al. (2025a) showed that the recent increase in the frequency and severity of compound hot and dry events caused net GPP reductions of -5.2PgC/y, globally. Solar radiation is a key driver of plant photosynthesis and thus GPP. Photosynthesis depends on the amount of Photosynthetically Active Radiation reaching the surface, with diffuse radiation often enhancing canopy-scale photosynthesis by reducing light saturation in upper leaves and increasing light penetration to lower canopy layers (Mercado et al., 2009). Sun et al. (2018) estimated that the contributions of temperature, radiation and water availability on global GPP trends were 13.07%, -7.24% and 11.74%, respectively over the period 1982–2015. The impact of climatic trends can vary geographically: at middle and high latitudes, GPP is mainly influenced by increases in radiation and temperature; at lower latitudes, changes in water availability are the primary driver; and at high altitudes, both temperature and water conditions determine GPP variations (Sun et al., 2018).

Temperature and water remain the dominant controls on TER, together accounting for roughly 44.15% of global TER variability (Zhao & Zhu, 2025). Both autotrophic and heterotrophic respiration are highly temperature-sensitive, yet their responses are strongly modulated by soil moisture. While TER typically rises with increasing temperature, it often reaches a threshold beyond which respiration rates decline sharply at higher temperatures (Zou et al., 2022). Soil moisture exerts a strong control over TER, particularly in arid and semi-arid environments. Low soil water content can place microbial communities under desiccation stress, and fluctuations in moisture also influence substrate availability and oxygen diffusion within the soil. As a result, limited soil moisture can substantially suppress respiration rates relative to what would be expected based solely on ambient temperature conditions (Moyano et al., 2013). TER rises steadily with increasing soil moisture, reaching its maximum at an identifiable optimal soil-moisture level. Beyond this point, excess soil water suppresses respiration (Peng et al., 2025). Recent studies found that variables related to biotic factors (e.g., vegetation structure, 25.91%) and spatiotemporal variation factors (e.g., land cover and phenology, 29.94%) were also key factors influencing large-scale TER (Zhao & Zhu, 2025).

Climate factors that control TER and GPP ultimately determine NEE. While water availability primarily governs local interannual variability in NEE, at the global scale, temporal fluctuations in NEE are largely driven by temperature variations (Jung et al., 2017).

1.3 Growing season dynamics

Growing season refers to the period of the year during which environmental conditions are favourable for plant growth and photosynthetic activity. Satellite and field observations show that growing season length has increased substantially over the last three decades (Fang et al., 2022; Garonna et al., 2016; Park et al., 2018). Earlier studies estimated a lengthening of approximately 10–20 days up to the early 21st century in temperate and cold regions of the Northern Hemisphere, largely attributed to global warming (Linderholm, 2006). This shift is driven by both earlier spring onset (Zhou et al., 2001) and delayed autumn senescence (Jeong & Medvigy, 2014). More recent evidence suggests that increasing tree cover has additionally extended the growing season length at the global scale (Fang et al., 2022).

Because land–atmosphere CO_2 exchange is tightly regulated by plant phenology (leaf emergence, canopy development, and senescence), changes in the onset and end of the growing season have important consequences for seasonal and annual carbon budgets. Over recent decades, multiple observational sources, including satellite vegetation indices, atmospheric CO_2 records, eddy-covariance measurements, and land-surface models, have

documented widespread modifications to growing season characteristics across the Northern Hemisphere.

One of the most consistent observations is the earlier onset of the growing season, in temperate and boreal regions. Numerous studies attribute this advance to rising spring temperatures in recent decades (Chen et al., 2023; Jeong et al., 2011). However, more recent analyses reveal that this trend has weakened since the late 1990s. Using long-term NDVI observations, Xiong et al. (2024) showed that the phenological sensitivity to warming decreased substantially across large areas of northern temperate and boreal forests, even though spring temperatures continued to rise. Their study suggests that the rate at which the growing season onset advances declined by nearly two thirds between 1999 and 2015. Importantly, the underlying reasons for this slowdown vary across regions. In European forests, a reduced temperature sensitivity of spring phenology contributed to a deceleration of the trend (Fu et al., 2015), whereas in boreal forests (particularly in Siberia and northwestern North America) , the slowdown was primarily linked to external climatic factors, notably reduced cumulative preseason temperatures (Park et al., 2018).

Autumn phenology exhibits similarly complex behaviour. Although warming generally delays leaf senescence and prolongs vegetation activity (Jeong et al., 2011; Zhu et al., 2012; Stinziano & Way, 2017), recent studies suggest that this trend may reverse under certain conditions. For example, Zani et al. (2020) reported that enhanced photosynthetic activity earlier in the season can accelerate the depletion of internal carbon stores, causing plants to progress more rapidly through their annual cycle and senesce earlier. Based on observational, experimental, and modelling evidence from European forests, they project that autumn senescence could advance by 3–6 days by the end of the 21st century.

Temperature remains the primary driver of spring phenology in high-latitude and temperate ecosystems. Warmer conditions promote earlier snowmelt, increase enzymatic activity, and accelerate leaf-out once photoperiod constraints are met. A meta-analysis by Fu et al. (2015) found that a 1° C increase in preseason temperature advances leaf onset by roughly three days in temperate tree species. However, several recent studies suggest that this temperature sensitivity is diminishing. Shi et al. (2025) apply the concept of a thermal optimum for phenological development, demonstrating that many ecosystems are now operating near or above their optimal temperature range for spring leaf-out. Beyond this threshold, additional warming can slow or even delay phenological onset, consistent with post-1990s trends across mid-latitude forests. Autumn phenology is also temperature-sensitive, but regulated by distinct mechanisms. Warmer autumns tend to delay leaf colouration and abscission, yet they also enhance ecosystem respiration, potentially reducing or offsetting the carbon gains associated with a longer growing season (Liu et al., 2022).

1.4 Observations of CO_2 exchange

1.4.1 Atmospheric CO_2 mole-fraction observations

Atmospheric CO_2 mole-fraction measurements from remote background stations reflect the influence of surface CO_2 sources and sinks over broad spatial scales, as air masses transport and mix signals from both land and ocean (Keeling et al., 1996). The long-term record and broad spatial representativeness of atmospheric CO_2 observations make them indispensable for constraining carbon exchange among the land, ocean, and atmosphere (Barichivich et al., 2013). Over decades, these measurements have revealed accelerating anthropogenic emissions (Friedlingstein et al., 2025), shifts in the strength of the terrestrial carbon sink (Graven et al., 2013), hemispheric asymmetries in CO_2 uptake (Barichivich et al., 2012), and responses of the biosphere to climatic anomalies such as El Niño events (Langenfelds et al., 2002) or major volcanic eruptions (Farquhar & Roderick, 2003).

Time-series analysis of atmospheric CO_2 isolates the dominant modes of variability: long-term growth rates, interannual anomalies, and seasonal cycles, each of which conveys information about different components of the Earth system (Thoning et al., 1989). The seasonality of atmospheric CO_2 recorded in these datasets was first documented in detail by Charles David Keeling at Mauna Loa Observatory in the mid-20th century, establishing the iconic Keeling Curve and demonstrating the capacity of continuous atmospheric monitoring to detect both long-term anthropogenic trends and natural carbon-cycle variability (Keeling, 1960).

The pronounced seasonal cycle in the Northern Hemisphere (Fig. 1.3) is driven largely by mid- and high-latitude terrestrial biosphere exchange. The CO_2 seasonal cycle has a peak in late winter to spring when photosynthesis is minimal and respiration and heterotrophic decomposition dominate ecosystem fluxes. As temperatures rise and day length increases, boreal and temperate vegetation initiate rapid growth, leading to a strong decline in atmospheric CO_2 as gross primary production outpaces ecosystem respiration across vast northern land areas. This drawdown produces a pronounced summer minimum, usually occurring in late summer or early autumn. Thereafter, declining day length and cooling temperatures suppress photosynthesis while respiration persists, leading to rising atmospheric CO_2 through autumn and early winter, followed by relatively stable concentrations during mid- to late winter (Keeling et al., 1996; Randerson et al., 1997; Barichivich et al., 2013; Zhao & Zeng, 2014). The magnitude and timing of these features have been linked to large-scale ecosystem dynamics, for example, the timing of spring green-up, autumn senescence, and changes in the land sink. Consequently, they have long served as a diagnostic of carbon-cycle dynamics between the land and the atmosphere (e.g. Keeling et al., 1996; Angert et al., 2005; Graven et al., 2013; Liu et al., 2024).

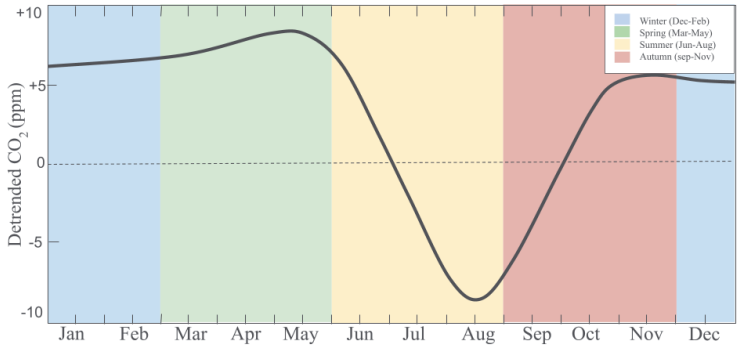


Figure 1.3: Schematic showing seasonal cycle of detrended atmospheric CO_2. The solid black curve shows the mean annual variation in detrended CO_2 mole-fraction (ppm) as a function of month at higher latitudes. Shaded backgrounds indicate seasons of the Northern Hemisphere: winter (Dec–Feb, blue), spring (Mar–May, green), summer (Jun–Aug, yellow), and autumn (Sep–Nov, red).

However, the use of atmospheric CO_2 as an integrative signal also introduces substantial challenges. Atmospheric records reflect the natural carbon cycle processes (photosynthesis, respiration, ocean exchange) constantly interacting with acute events (e.g., volcanic eruption, El Niño) and long-term anthropogenic impacts (emissions from fossil fuel combustion) to determine the overall atmospheric CO_2 levels and their variability. Observed variations do not correspond directly to local sources or sinks, but instead represent the integration of spatially and temporally heterogeneous fluxes through atmospheric transport (Qu et al., 2025). This complicates efforts to attribute observed changes to specific processes or regions without the aid of atmospheric inversion methods or transport modelling (Schuh et al., 2019). For example, spatial asynchrony in spring green-up across continents is smoothed into a more coherent hemispheric-scale signal by the time it reaches remote background stations (Barichivich et al., 2012).

Gaps in the observational record, the superposition of diverse surface flux signals, and synoptic-scale variability further obscure underlying climate-driven trends. These elements create short-term fluctuations unrelated to surface carbon fluxes that must be disentangled to isolate meaningful ecological or climatic information. As a result, filtering and curve-fitting techniques are routinely applied to produce smooth, continuous time series suitable for scientific analysis (Trivett et al., 1989). Furthermore, interannual variations in wind patterns, convection, and large-scale circulation modulate the amplitude,

phase, and shape of the CO_2 seasonal cycle observed at remote stations (Sec. 1.5).

1.4.2 Net Ecosystem Exchange (NEE) Observations

To complement these large-scale, integrated atmospheric signals, direct measurements of surface-atmosphere CO_2 exchange are obtained through the eddy-covariance (EC) technique. EC flux measurements offer insight into ecosystem-level carbon dynamics. The global eddy covariance (EC) network, coordinated through FLUXNET, comprises hundreds of tower sites that measure high-frequency turbulent exchange of CO_2, water vapour, and energy between ecosystems and the atmosphere (Baldocchi et al., 2001). These measurements have become central to carbon-cycle research, revealing how ecosystems respond to climate variability and extremes. For example, EC records show strong reductions in net carbon uptake during major droughts and heatwaves, such as the 2003 European heatwave, when many forests switched from carbon sinks to sources (Ciais et al., 2005). Long-term EC observations also reveal phenological sensitivities: earlier spring uptake and delayed autumn release have been observed in boreal and temperate forests during warm years, linking temperature anomalies directly to seasonal carbon exchange patterns (Keenan et al., 2014).

However, using EC measurements remains challenging for analysis at the global scale. This is primarily due to the limited spatial representativeness of individual tower footprints, which typically encompass only a few square kilometers, and the uneven spatial distribution of flux towers (Jung et al., 2020; Walther et al., 2022). Currently, more than 500 EC tower sites are operating across approximately 30 regional flux networks on five continents. However, these sites collectively cover only a narrow subset of the Earth's biomes, disturbance regimes, and land-use systems (Zhu et al., 2013). Long-term EC records, defined as those spanning more than a decade, are particularly sparse across Arctic and boreal regions, where understanding seasonal carbon dynamics is critically important in the context of climate change (Pallandt et al., 2024). In addition to limitations in spatial coverage, EC measurements face several technical challenges. Data gaps are frequently introduced by sensor malfunctions, power failures, harsh environmental conditions and periods of low turbulence under stable atmospheric conditions, especially during winter (Vekuri et al., 2023). While gap-filling algorithms have been developed to address these interruptions, they inherently introduce uncertainties and can lead to systematic biases in the final flux estimates. For instance, Vekuri et al. (2023) demonstrated that a commonly used EC gap-filling technique can systematically bias carbon balance assessments.

To bridge the gap between site-level EC measurements and large-scale estimates, upscaling frameworks that integrate satellite remote sensing and meteorological data with flux tower observations have been developed. One example is FLUXCOM, which

uses machine learning algorithms to integrate data from the FLUXNET network of EC towers with global predictor variables, including satellite-derived vegetation indices and climate reanalysis datasets (Beer et al., 2010; Jung et al., 2011, 2020). Initially, empirical models are developed at the site level to relate fluxes such as NEE to environmental drivers. These models are then applied globally to generate gridded flux products. However, these estimates are subject to considerable uncertainties that stem from the choice of machine learning algorithms, variability in predictor datasets, inconsistencies in the underlying flux measurements, and incomplete biome representation within FLUXNET (Jung et al., 2020). Recent advances have led to the development of FLUXCOM-X, an enhanced version of the FLUXCOM framework designed to offer greater flexibility and improved technical capabilities. Its first global product, X-BASE, exhibits improved consistency with independent atmospheric CO_2 constraints compared to earlier FLUXCOM outputs. Nevertheless, important challenges remain. For example, X-BASE still exhibits low interannual variability in global NEE, which is a problem common to state-of-the-art data-driven flux products (Nelson et al., 2024).

Atmospheric inversion provides a top-down framework for estimating surface–atmosphere CO_2 exchange at regional to global scales.(e.g. Byrne et al., 2020; Chen et al., 2021; Palmer et al., 2019; Miller & Michalak, 2020; Enting et al., 2012). In this approach, NEE is inferred by working backward from measured atmospheric mole fractions to estimate the surface fluxes that produced them. It combines (i) observations of CO_2 mole fractions from ground stations, aircraft and satellites; (ii) numerical atmospheric-transport models that simulate how winds, turbulence and convection move CO_2 through the atmosphere; and (iii) Bayesian optimization that adjusts prior surface flux estimates until the modeled mole fractions best match the observations within their respective uncertainties. The resulting solution yields spatially and temporally resolved maps of CO_2 sources and sinks. However, estimates derived from atmospheric tracer inversions are often inconsistent across models, reflecting differences in input data, inversion approaches, and atmospheric transport (Munassar et al., 2023; Baker et al., 2006).

1.5 Atmospheric transport and CO_2 observations

1.5.1 Influence of transport on CO_2 measurements at monitoring sites

Interpreting atmospheric CO_2 measurements requires an explicit understanding of the atmospheric transport processes that govern how surface fluxes imprint on observed atmospheric mole fractions. Although the seasonal cycle recorded at background stations is often taken as an indicator of terrestrial biosphere activity, the relationship between surface exchange and the atmospheric signal is indirect. CO_2 measured at any observation site is the result of contributions from diverse upwind regions that have been advected, mixed, and diluted through atmospheric circulation. Consequently,

the observed variability in CO_2 reflects not only changes in surface fluxes, but also temporal and spatial fluctuations in atmospheric transport, making transport one of the dominant sources of uncertainty when attributing observed signals in atmospheric CO_2 to underlying carbon cycle processes.

Measurements collected across the global monitoring network reflect a mixture of continental, marine, and regional influences, the relative contributions of which are determined by atmospheric circulation. The influence of atmospheric transport on these measurements operates across a wide range of timescales, from synoptic variability on the order of days to longer-term changes in large-scale circulation patterns and influence the structure of the atmospheric CO_2 seasonal cycle. Taguchi et al. (2003) and Higuchi et al. (2002), for instance, found that fluctuations in atmospheric dynamics alone can account for a substantial fraction of the observed changes in the seasonal amplitude at Northern Hemisphere background sites. Similarly, Murayama et al. (2007) demonstrated that at Arctic background stations such as Alert (ALT) and Barrow (BRW), interannual differences in synoptic circulation patterns account for much of the observed variability in the seasonal cycle timing and amplitude. More recent studies confirm that variability in atmospheric transport continues to play a key role in shaping the magnitude and timing of the atmospheric CO_2 seasonal cycle (e.g. Li et al., 2022). These findings illustrate that atmospheric transport can produce features in the observed CO_2 record that resemble variations in surface fluxes, complicating direct interpretation.

Atmospheric transport affects CO_2 observations at all monitoring sites, but its influence varies strongly with each site's position relative to large-scale circulation patterns. Murayama et al. (2007) noted that, because of their location within the atmospheric circulation, some Northern Hemisphere monitoring stations may exhibit limited sensitivity to even large changes in biospheric carbon fluxes. A well-studied illustration of transport sensitivity is the Mauna Loa Observatory (MLO), which is situated in the central tropical North Pacific between the midlatitude westerlies and the tropical easterlies. Lintner et al. (2006) showed that this setting exposes MLO to two dominant, seasonally varying transport pathways: air masses arriving from the west over the Eurasian continent and those arriving from the east over the Pacific Ocean. For Arctic background stations such as ALT in the Canadian Arctic and BRW in the Alaskan Arctic, atmospheric transport has been characterised primarily in terms of seasonally varying source regions. Transport-model analyses show that air masses sampled at these sites are frequently influenced by long-range transport from Eurasia, particularly from Siberian and European regions, whereas during summer the Arctic is more often influenced by marine air masses and regional Arctic sources as large-scale transport from lower latitudes is reduced (Sharma et al., 2006; Stohl, 2006). This suggests that the seasonal alternation of transport pathways plays a key role in shaping the CO_2 variability observed at different sites.

1.5.2 Overview of the global tracer transport model TM3

Given the strong role of transport in shaping observed CO_2 variability, atmospheric transport models are essential tools for diagnosing how surface fluxes from upwind regions influence CO_2, dry-air mole fraction measurement at remote background sites. In this thesis we use the three-dimensional Eulerian transport model TM3 (Tracer Model version 3) (Heimann & Körner, 2003). TM3 has been extensively evaluated in the context of global carbon-cycle studies, including experiments as part of the TransCom intercomparison project (Gurney et al., 2002; Patra et al., 2008), where it has been used to examine the sensitivity of atmospheric tracer distributions to different transport mechanisms and to evaluate regional flux estimates.

The atmospheric transport model TM3 represents tracer evolution by solving the continuity equation in flux form:

$$\frac{\partial}{\partial t}(\rho\phi) + \nabla \cdot (\rho \mathbf{u}\phi) = S$$

This formulation is applied on a global, three-dimensional Eulerian grid. In this equation, ϕ is the tracer mixing ratio (kg of tracer per kg of air), ρ denotes air density, $\mathbf{u}$ represents wind velocity, and S corresponds to the volumetric source or sink term of the tracer (Heimann & Körner, 2003). Here, TM3 is driven in offline mode by 6-hourly meteorological fields from the NCEP reanalysis, interpolated to the model grid (here 5° in longitude by 4° in latitude, with 19 vertical levels). The primary input variables are horizontal wind components, temperature, specific humidity, and surface pressure, along with geopotential heights. These fields are used to diagnose advection, vertical diffusion and convective transport as described in Heimann & Körner (2003). In TM3, advection, defined as the transport of tracers by three-dimensional air mass fluxes, is computed using the "slopes scheme" introduced by Russell and Lerner (Russell & Lerner, 1981).

Within a single one-dimensional advection step, the slopes scheme updates each grid cell through a sequence of calculations. As described in Heimann & Körner (2003), first, the air mass in the grid cell is revised by accounting for fluxes entering and leaving across its boundaries. Next, tracer exchange across these boundaries is determined using information on tracer mass and its spatial gradients in both the target cell and neighbouring cells. This is followed by an update of the tracer mass within the grid cell after accounting for these fluxes. Finally, the spatial gradients (slopes) of the tracer are recalculated to reflect the new distribution. In addition to advective transport, vertical redistribution associated with convective activity is represented using a cloud mass flux parameterisation (Tiedtke, 1989). Turbulent mixing in the vertical direction is parameterised through stability-dependent diffusion following Louis (1979). Together, these processes redistribute tracer mass throughout the troposphere and lower stratosphere. A detailed formulation of the transport operators and numerical scheme is

given in Chapter 1 of Heimann & Körner (2003).

1.6 The Carbon Uptake Period as an integrative diagnostic

The Carbon Uptake Period (CUP) refers to the period of the year during which a terrestrial ecosystem is a net carbon sink (Gonsamo et al., 2012). This period is bounded by the dates when NEE shifts from positive to negative (onset) and back to positive (termination). This typically occurs in early to mid-spring at high latitudes, as GPP resumes and increases with rising light and temperature, exceeding TER and leading to net carbon uptake. The CUP concludes in late summer or early autumn when GPP declines below TER, resulting in a return to net carbon release. During the net uptake phase, a notable decline in atmospheric CO_2 mole fractions is observable at many Northern Hemisphere monitoring sites, reflecting widespread terrestrial carbon sequestration (Fig. 1.3).

The CUP is distinct from the growing season, which characterises the period of potential photosynthetic activity based on biological or climatic indicators such as leaf emergence, senescence, or temperature thresholds. In contrast, the CUP is defined functionally in terms of carbon exchange and explicitly accounts for the balance between photosynthetic uptake and ecosystem respiration. As a result, the two periods do not necessarily coincide. For example, photosynthetic activity can begin before ecosystems become net carbon sinks if respiration remains high in early spring, and similarly, carbon uptake can cease before the end of the growing season when respiration dominates in autumn (Churkina et al., 2005). Consequently, the CUP provides a more direct measure of ecosystem carbon balance, whereas the growing season reflects broader phenological or climatic conditions.

Empirical evidence indicates that the response of net ecosystem carbon uptake to an extended growing season is not uniform. Some studies report increases in net carbon uptake under longer growing seasons (e.g. Churkina et al., 2005; Dragoni et al., 2011), whereas others find little to no significant effect (Parmentier et al., 2011; Barichivich et al., 2012). In contrast, several investigations suggest that prolonged growing seasons may even reduce net carbon uptake or lead to net carbon losses (e.g. Hu et al., 2010; Piao et al., 2008).

Studies investigating the CUP have primarily relied on atmospheric CO_2 mole-fraction measurements (e.g. Barlow et al., 2015; Barichivich et al., 2012) and EC–based estimates of NEE (e.g. Fu et al., 2019; Churkina et al., 2005) as observational constraints on CUP dynamics. In the Northern Hemisphere, atmospheric CO_2 records show a spring

time peak, corresponding to the onset of the CUP, and a late summer or early autumn minimum, marking the termination of the CUP (Fig. 1.3). In NEE measurements, the CUP is identified as the period during which NEE is negative, under the sign convention defined in Eq. 2.1.

During the past few decades, many studies have reported an earlier onset of photosynthetic activity and a longer growing season, particularly in response to spring warming. These phenological shifts have significant implications for the timing and magnitude of the CUP at local to hemispheric scales (e.g. Goulden et al., 1996; Keeling et al., 1996; Baldocchi et al., 2001; Churkina et al., 2005; Gonsamo et al., 2012). For instance, warmer spring temperatures have been linked to an earlier start and extension of the CUP, as observed in the seasonal cycle of atmospheric CO_2 concentrations (Keeling et al., 1996; Randerson et al., 1999; Nemani et al., 2003). However, not all responses to warming are uniform. Piao et al. (2008) found that in some regions, warming led to an earlier end of the CUP, as respiratory carbon losses outpaced gains from photosynthesis. Barichivich et al. (2012) noted an erlier onset of the CUP, however, they did not detect a significant trend in overall CUP duration between 1987 and 2009, due to concurrent advances in CUP termination. More recent research suggests that the previously strong link between rising spring temperatures and earlier CUP onset is weakening in many regions. For example, a recent study focusing on the Siberian ecosystem (Tran et al., 2024) found no significant trends in the timing of CUP onset or termination between 2010 and 2021, suggesting regional stability in the timing of the CUP despite ongoing climate change. Together, these studies indicate that changes in CUP timing and duration show patterns that are regionally variable and complex.

The timing, extend and spatial variations of the CUP is increasingly recognized as a valuable diagnostic in carbon-cycle research because it provides an integrative measure of ecosystem carbon sequestration that is closely linked to NEE. Early studies demonstrated that CUP duration is strongly predictive of annual NEE in temperate and boreal ecosystems, with the length of the CUP explaining a substantially larger fraction of interannual variability in NEE than conventional growing-season metrics (Baldocchi et al., 2001; White & Nemani, 2003; Wu et al., 2012). This strong relationship arises because the CUP integrates the combined effects of gross primary production and total ecosystem respiration, which respond to climate variability in complex and sometimes asymmetric ways that are not captured by phenology alone. As a result, the CUP has been shown to be a more process-relevant indicator of ecosystem carbon balance, providing a useful constraint for evaluating model representations of seasonal carbon dynamics and ecosystem responses to climate variability (Liu et al., 2017; Gonsamo et al., 2012).

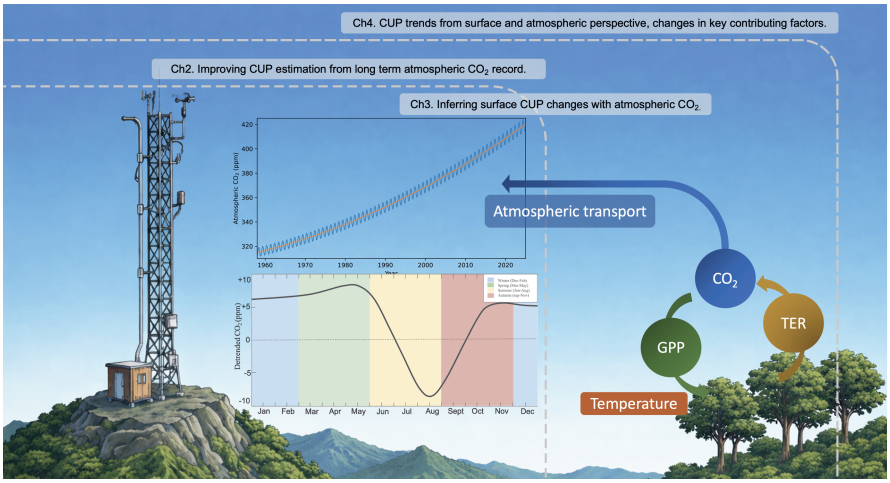


Figure 1.4: Schematic illustrating the focus of each main chapter of the thesis and the connections between these chapters.

1.7 Research objectives and thesis outline

This PhD project focuses on investigating changes in the timing of the CUP in the Northern Hemisphere, the drivers of these changes, and the methodological challenges that influence its estimation. The research emphasises three main aspects: improving methodologies for estimating CUP-related metrics from atmospheric CO_2 time series, examining the influence of atmospheric transport on observed CUP signals, and interpreting these signals to attribute observed changes to underlying ecosystem drivers. Guided by these objectives, the thesis is structured around three core chapters, each organized into standard scientific sections – introduction, methods, results, discussion, and conclusions. A visual summary of the key components of each chapter and how they collectively link to address the overarching research question is shown in Fig. 1.4.

Chapter 2 focuses on identifying and addressing limitations in the use of long-term atmospheric CO_2 mole-fraction records for estimating CUP changes. The work in this section focuses on improving the estimation of the CUP timing from atmospheric CO_2 time series using a derivative-based threshold method applied to detrended CO_2 mole-fraction data. To account for uncertainties introduced during curve fitting, a statistical resampling approach based on residual bootstrapping is employed to generate ensembles of plausible fits. This framework allows the propagation of curve-fitting uncertainty into CUP metrics to be quantified, and results in the definition of a more robust, uncertainty-aware threshold for CUP onset and termination. These methodological

advances form the foundation for the subsequent analyses and interpretation of CUP variability in chapter 3 and chapter 4.

Building on this framework, Chapter 3 examines how well CUP estimates derived from atmospheric CO_2 measurements reflect the timing and duration of the CUP in the underlying surface carbon fluxes, with particular emphasis on the role of atmospheric transport variability. Idealized flux scenarios with prescribed modifications to NEE fluxes are implemented in an atmospheric transport model to generate corresponding CO_2 mixing ratio fields. This approach allows the sensitivity of site-level atmospheric CO_2 signals to regional surface flux changes to be quantified, and enables the attribution of observed variations in CUP timing to contributions from different Northern Hemisphere regions.

In the final study, presented in Chapter 4, CUP estimates are derived from atmospheric CO_2 measurement sites, as well as from NEE fluxes produced by the two top-down inversion models (CarbonTracker and CarboScope) and upscaled fluxes from the FLUXCOM-X product. Spatial and temporal patterns in CUP onset, termination, and duration are analysed for the period 2001–2021, which includes the global warming hiatus of the early 2000s, and their links to ecosystem drivers are investigated.

Finally, Chapter 5 synthesizes the main findings of the thesis, highlights their implications for understanding carbon–climate interactions, discusses remaining methodological and scientific challenges, and outlines directions for future research.

Chapter 2

Reducing errors on estimates of the carbon uptake period based on time series of atmospheric CO_2

This chapter is based on:

Kariyathan, T., Bastos, A., Marshall, J., Peters, W., Tans, P., & Reichstein, M. (2023). Reducing errors on estimates of the carbon uptake period based on time series of atmospheric CO_2. Atmospheric Measurement Techniques, 16 , 3299–3312. doi:10.5194/amt-16-3299-2023.

Abstract

High-quality, long-time-series measurements of atmospheric greenhouse gases show inter-annual variability in the measured seasonal cycles. These changes can be analyzed to better understand the carbon cycle and the impact of climate drivers. However, nearly all discrete measurement records contain gaps and have noise due to the influence of local fluxes or synoptic variability. To facilitate analysis, filtering and curve-fitting techniques are often applied to these time series. Previous studies have recognized that there is an inherent uncertainty associated with this curve fitting and the choice of a given mathematical method might introduce biases. Since uncertainties are seldom propagated to the metrics under study, this can lead to misinterpretation of the signal. In this study, we use an ensemble-based approach to quantify the uncertainty of the derived seasonal cycle metrics. We apply it to CO_2 dry-air mole fraction time series from flask measurements in the Northern Hemisphere. We use this ensemble-based approach to analyze the carbon uptake period (CUP: the time of the year when the CO_2 uptake is greater than the CO_2 release): its onset, termination and duration. Previous studies have diagnosed CUP based on the dates on which the detrended, zero-centered seasonal cycle curve switches from positive to negative (the downward zero-crossing date, DZCD) and vice versa (upward zero-crossing date, UZCD). However, the UZCD is sensitive to the skewness of the CO_2 seasonal cycle during the net carbon release period. Hence, we develop an alternative method proposed by Barlow et al. (2015) to estimate the onset and termination of the CUP based on a threshold defined in terms of the first derivative of the CO_2 seasonal cycle. Using the ensemble approach, we arrive at a tighter constraint to the threshold by considering the annual uncertainty; we call this the ensemble of first derivative (EFD) method. Further, using the EFD approach and an additional curve-fitting algorithm, we show that (a) the uncertainty of the studied metrics is smaller using the EFD method than when approximated using the timing of the zero-crossing date (ZCD), and (b) the onset and termination dates derived with the EFD method provide more robust results, irrespective of the curve-fitting method applied to the data.

2.1 Introduction

Ongoing in situ measurements of the atmospheric CO_2 mixing ratio have revealed an increase in CO_2 mole fraction in the atmosphere. The increase in atmospheric CO_2 due to release of carbon from fossil fuel burning and land-use change is buffered by net CO_2 uptake by the ocean and land biosphere (Keeling, 1960). Since then, many studies have used high-precision measurements of greenhouse gases at MLO and other sites across the globe to better understand the role of CO_2 in the global climate (e.g., Langenfelds et al., 2002; Keeling et al., 2017; Barlow et al., 2016). The analysis of such atmospheric time series helps to identify and isolate the long-term trends, inter-annual variability and seasonality of climatically important greenhouse gases (Thoning et al., 1989). However, these measurement records contain gaps and are influenced by local fluxes or synoptic-scale variability, which induces noise on the underlying climate signals. Hence the use of filtering and curve-fitting techniques to obtain smooth and continuous data has been an inevitable part of such studies (Trivett et al., 1989). The choice of mathematical method for data processing can, however introduce biases that can result in misinterpretation of the signal (Nakazawa et al., 1997; Tans et al., 1989; Pickers & Manning, 2015; Barlow et al., 2015).

Curve-fitting methods are often used to preprocess atmospheric time series for analysis. Three examples are found in the commonly used software packages, HPspline (Bacastow et al., 1985), CCGCRV (Thoning et al., 1989) and STL (Cleveland et al., 1990). Each of these methods produces a gap-filled time series that contains the important features of the atmospheric record; however the resultant fitted curves vary significantly from each other owing to differences in their response to gaps and outliers in the original data. Pickers & Manning (2015) addressed the sensitivity of scientific conclusions to the curve-fitting method used, by repeating a scientific study (Piao et al., 2008) using two additional curve-fitting method. Both studies looked at changes in the CO_2 seasonal cycle zero-crossing date (ZCD) for 10 midlatitude to high-latitude, Northern Hemisphere stations. The re-analysis by Pickers & Manning (2015) found that the major conclusion of Piao et al. (2008) was robust but that inferences at individual stations depended on the curve-fitting method. This was corroborated by Barlow et al. (2015), who used a wavelet-based curve-fitting method to illustrate the sensitivity of various key aspects of the seasonal cycle of CO_2 time series to the curve-fitting approach. Thus, the impact of bias introduced by data processing methods can vary based on the data set used and the type of analyses performed. Each method has its strengths and weaknesses; hence Pickers & Manning (2015) argued that data must be analyzed with multiple approaches to ensure that results are robust and free from bias. Despite this recommendation, studies that focus on metrics of time series such as the ZCD or seasonal cycle amplitude usually use a single curve-fitting method for analysis (e.g., Park et al., 2019; Piao et al., 2018), which can lead to differences in the conclusions that are drawn. An example is the

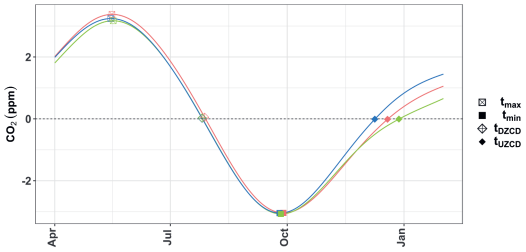


Figure 2.1: Diagram showing how the skewness of the seasonal cycle can influence the estimation of the CUP based on the ZCD. The three seasonal cycles have similar seasonal cycle maxima, minima and downward ZCDs but very different upward ZCDs.

disagreement in the direction of the trend of the CO_2 seasonal cycle amplitude (SCA) at Alert, Canada between Chan & Wong (1990) and Keeling et al. (1996), as shown by Pickers & Manning (2015).

Metrics derived from CO_2 time series such as the seasonal cycle peaks can be highly sensitive to data gaps and noise. This is especially true for metrics associated with the growing season onset at higher-latitude sites, where CO_2 shows flat or multiple peaks in winter (Barlow et al., 2015). Hence, deriving other metrics like the timing of the carbon uptake period (CUP) from the seasonal cycle maximum results in less robust estimates. The CUP is defined as the time of the year during which the CO_2 uptake is greater than the CO_2 release. The onset and termination of the CUP are marked by the spring maximum and late-summer minimum of the seasonal cycle, respectively. However, the seasonal cycle at many observational sites is characterized by a flat peak or multiple peaks in winter, making it difficult to estimate the start of the CUP. To avoid this problem, previous studies have used the comparatively more unambiguous ZCD to approximate the timing and duration of the CUP (e.g., Piao et al., 2008). The ZCDs are the two dates in the seasonal cycle when the detrended CO_2 curve crosses the zero line (an imaginary line passing through 0 ppm in the detrended CO_2 seasonal cycle). Note that this period starts later than the seasonal spring maximum and ends later than the summer minimum; i.e., it is shifted compared to the CUP definition above. This approximation is thus based on the assumption that if the shape of the seasonal cycle does not change significantly, a change in the phase at one point (e.g., maximum) of the seasonal cycle can be traced as a relative phase change at other points (Barichivich et al., 2012). However, the shape of the seasonal cycle changes from year to year, and the CUP approximated using the ZCD may be erroneous (Barlow et al., 2015). This is illustrated in Fig. 2.1.

Barlow et al. (2015) show that using the time derivative of a time series can provide a more robust estimate of the key dates that define the CUP, compared to the conventional use of ZCDs. A threshold of this time derivative as a fraction of peak uptake in mid-summer was shown to be a robust metric to define both start (threshold 25%) and end (threshold 0%) of the CUP in their study. They used a synthetic data experiment applying a linear trend with substantial interannual variations in amplitude (± 25%) and CUP (±10 days) to a dCO_2/dt time series, to show that in the absence of transport, their method can capture the prescribed linear trend of the CUP. We expand on that work here by additionally creating an ensemble of fitted time series using residual bootstrapping on a loess-fit. For each ensemble member we calculate the first derivative, allowing us to determine the timing of the various start, end, and peak moments in the CUP; its duration; and the individual uncertainty on each metric for each individual year in the time series. We call this the ensemble of first derivative method (EFD method). The EFD method accounts for the random and non-linear changes from year to year in the CO_2 time-series, allowing for a better handling of outlier years (in mean or uncertainty), which potentially improves trend analyses of seasonal cycle changes. We apply the EFD method to long time series and a set of stations covering the low latitudes, midlatitudes and high latitudes.

We first use the EFD method to confirm that the CO_2 ZCDs are not the best proxy for determining the timing and duration of the CUP, also when the newly derived uncertainty is considered. We then demonstrate that the EFD method is independent of the skewness of the seasonal cycle, and we optimize the threshold for the CUP onset and termination based on the first derivative. The derived uncertainty also reveals that the robustness of various metrics is site-dependent, with high latitudes being sensitive to the seasonal cycle maximum (also found in Barlow et al. (2015)) and low-latiude sites sensitive to the upward zero-crossing date (UZCD) of the CO_2 seasonal cycle. We also tested whether the EFD method is sensitive to the specific curve-fitting method applied by fitting the data with the commonly used CCGCRV method, which is a frequency-domain-based filter, similar to the wavelet transform approach of Barlow et al. (2015). The measurements used in this study are presented in Sect. 4.2 and the EFD method is presented in Sect. 4.3. The results and the discussion on the findings can be found in Sects. 4.4 and 4.4.4 respectively, and Sect. 2.6 summarizes the findings of this study.

2.2 Data

We use the discrete CO_2 dry-air mole fraction from flask measurements from 10 observational sites of the NOAA/ESRL network (Dlugokencky et al., 2019, 2020), ranging from 19 to 82°N latitude. Table 2.1 lists the station names, station codes, their locations and the studied time period for each station (longer time records are available for MLO and NWR

Table 2.1: Observational sites of NOAA/ESRL network used in this study

Station name	Station code	Latitude	Longitude	Time period	Data Source
Mauna Loa, Hawaii, United States	MLO	19.47°N	155.57°W	1977-2017	(Dlugokencky et al., 2019)
Assekrem, Algeria	ASK	23.26°N	5.63°E	1996-2018	(Dlugokencky et al., 2020)
Sand Island, Midway, United States	MID	28.21°N	177.36°W	1986-2018	(Dlugokencky et al., 2020)
Weizmann Institute of Science at the Arava Institute, Ketura, Israel	WIS	29.96°N	35.06°E	1996-2018	(Dlugokencky et al., 2020)
Terceira Island, Azores, Portugal	AZR	38.76°N	27.37°E	1996-2018	(Dlugokencky et al., 2020)
Niwot Ridge, Colorado, United States	NWR	40.05°N	105.58°W	1976-2018	(Dlugokencky et al., 2020)
Shemya Island, Alaska, United States	SHM	52.71°N	174.12°E	1986-2018	(Dlugokencky et al., 2020)
Barrow Atmospheric Baseline Observatory, United States	BRW	71.29°N	156.61°W	1972-2017	(Dlugokencky et al., 2019)
Ny-Alesund, Svalbard, Norway and Sweden	ZEP	78.90°N	11.88°E	1995-2018	(Dlugokencky et al., 2020)
Alert, Nunavut, Canada	ALT	82.50°N	62.50°W	1986-2017	(Dlugokencky et al., 2019)

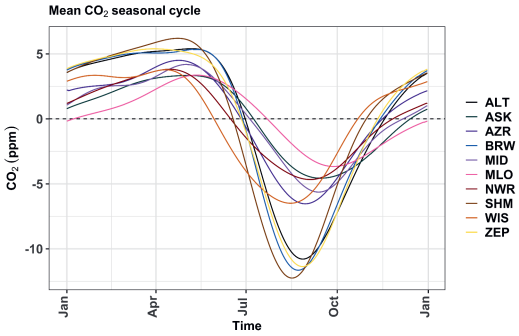


Figure 2.2: Mean seasonal cycle of CO_2 at the stations studied. Note that this seasonal cycle is derived from the fitted loess curves and excludes the observed mean, trend and high-frequency variations in CO_2.

(Niwot Ridge), but these years have large data gaps of a year or more and hence are not considered for analysis). At these observational sites, air is sampled in glass flasks under background conditions; hence the dry-air mole fractions from the air samples are representative of the zonal mean atmospheric composition (Langenfelds et al., 2002). These air samples are collected weekly in pairs for quality control, and pairs with a difference of less than 0.5 ppm between the two samples are flagged as good-quality data ("good pairs") (Dlugokencky et al., 2019, 2020). For our analysis, we use the mean value of each pair considered as "good pairs" and exclude low-quality measurements, which introduces irregular gaps in the data. The mean seasonal cycle of the higher-latitude stations (above 45°N latitude, i.e., SHM (Shemya Island), BRW (Barrow Atmospheric Baseline Observatory), ZEP(Ny-Ålesund, Svalbard, Norway and Sweden), and ALT (Alert)), is characterized by a broader maxima or multiple peaks in winter. Some lower-latitude stations like MLO, MID (Sand Island, Midway) and NWR have distinct seasonal cycles with clearly defined maxima, while others, like ASK (Assekrem, Algeria), AZR (Terceira Island, Azores) and WIS (Weizmann Institute of Science), have broader peaks (Fig. 2.2).

2.3 Method

2.3.1 Loess fitting

The time series of CO_2 can be described as the superposition of different modes of variability, acting at different frequencies. A standard approach to extract these modes of variability from the observations ($X_{obs}(t)$) is to define

$$X_{\text{obs}}(t) = X_{\text{trend}}(t) + X_{\text{seas}}(t) + R(t) \tag{2.1}$$

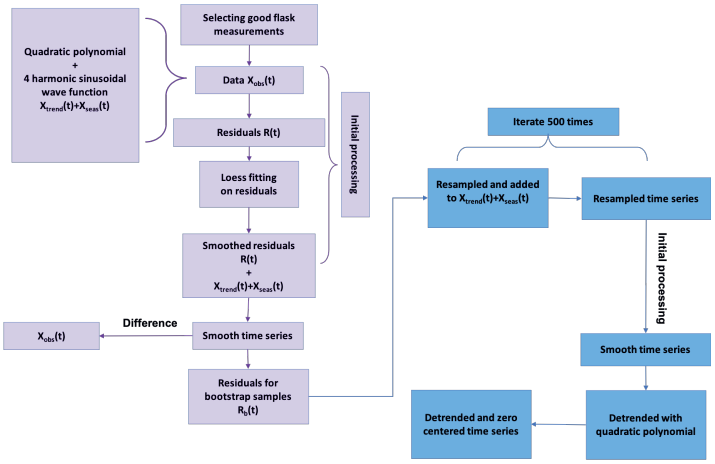


Figure 2.3: Flow diagram explaining the processes of curve fitting (purple boxes) and ensemble generation (blue boxes).

where $X_{trend}(t)$ is the low-frequency component of the data, which captures variability on multi-annual time scales; $X_{seas}(t)$ represents the seasonal cycle, which can be expressed in terms of a series of harmonics; and R(t) captures the remaining variability (Cleveland et al., 1990). The data used in this study are provided at approximately weekly time steps and include gaps, as described above. We fill gaps and estimate daily values by fitting a series of curves described in Eq. (2.1) and use residual bootstrapping (Kreiss & Lahiri, 2012) to generate an ensemble of 500 fitted curves consistent with the observational data for uncertainty estimation. Figure 2.3 describes the steps involved in the curve fitting and uncertainty estimation. Each step is described in detail below.

First, we separate the long-term trend and mean seasonal cycles ($X_{trend}(t) + X_{seas}(t)$) with a second-degree polynomial and four harmonic sinusoidal functions respectively (Bacastow et al., 1985). The remaining variability, R(t), is referred to as the residuals, which we verified to not show autocorrelation. We then fit a smooth curve to the residuals using the "loess" (local regression) method, which smooths the data, taking into account the gap lengths in the data. The "Caret" package (Kuhn, 2020) in R provides a method for optimizing the smoothing parameter for the "loess" regression using a mathematical method called k- fold cross validation. The optimization is based on five repetitions of 10-fold (k=10) cross-validation, where the sub-samples are randomly sampled with restitution. The optimized smoothing parameters are then used to fit a smooth curve to the residuals (R(t)). The resulting smoothed residuals ($R_s(t)$), which contain the remaining variability, are added back to the other components ($X_{trend}(t) + X_{seas}(t)$). This

produces a continuous and smooth data set that preserves short-term variations.

2.3.2 CCGCRV fitting

CCGCRV is a curve-fitting method developed by Kirk Thoning and Pieter Tans (Global Monitoring Laboratory (GML), NOAA) in the late 1980s. The method fits a combination of polynomials and annual harmonics to the data to approximate the long-term variation and seasonal cycle. The short-term and interannual variability are retained by filtering the residuals from the fit using a low-pass filter. A detailed description of the routines used for fitting the data and filtering of residual can be found in Thoning et al. (1989). In this study we use the C language version of CCGCRV, freely available at: ftp://ftp.cmdl.noaa.gov/pub/john/ccgcrv/ (last access: 22 June 2022), for the curve fitting and finally obtaining a detrended time series. The values chosen for the input parameters were taken from Table 2 of Pickers & Manning (2015), who optimized them by fitting artificial data (short-term cut-off period f_s: 250 days; long-term cut-off period f_l: 1500 days; number of harmonic terms: 4; degree of polynomial function: 3).

2.3.3 Ensemble generation

Further, for uncertainty estimation, we generate 500 bootstrap samples from the curve-fitted data. For this, we calculate the difference between the smoothed data and the observational data, which gives the new set of residuals for generating bootstrap samples. These residuals are resampled (with replacement) and added to the initial fitted curve, producing a resampled time series. The resampled time series is processed as described in the preceding sections to obtain a continuous and smooth data set with daily values. The residual resampling and further processing are iterated 500 times to create an ensemble of 500 slightly different de-trended time series (bootstrap samples) which are all consistent with the observations (Fig 2.3 shows these steps for loess fitting). The classical bootstrapping method (where the observations are resampled) cannot be applied directly to a time series data as the resampling step fails to replicate the time-dependent structure. Hence, we use residual bootstrapping where bootstrapping is applied to the residuals obtained from fitting a model to the raw data. The resampled time series thus show the same time dependence as the observational data but are produced from the fitted curve and a random component from the residual resampling.

The ensemble of fitted curves is used to constrain the uncertainty in seasonal cycle metrics estimates. If the estimated metrics differ largely across the bootstrap samples, it indicates that the metric estimate is influenced by the inherent uncertainty in extracting a definitive seasonal cycle, by curve-fitting the discrete data. Hence, interpreting these metrics without accounting for this uncertainty can be misleading.

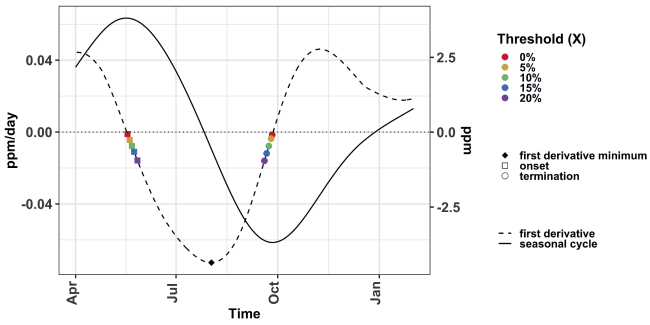


Figure 2.4: Schematic diagram showing the timing of the CUP as determined by the first derivative method. The timing is marked by a threshold, defined in terms of the first derivative of the CO_2 seasonal cycle. It is defined as X% of the first derivative minimum. The value of X is varied from 0% to 20%, and the corresponding threshold value is marked on the seasonal cycle first derivative with different coloured points. Their timing then defines the timing of the CUP for the different threshold values. The day of the onset and the termination of the CUP are defined by the points before and after the first derivative minimum, respectively. The squares and circles denote the onset and threshold calculated with different thresholds.

2.3.4 Ensemble of first derivative (EFD) method

At high-latitude measuring stations, the CUP extends from the seasonal cycle maximum in spring to the seasonal cycle minimum in late summer (Barichivich et al., 2012), driven by CO_2 uptake by ecosystems in the Northern Hemisphere. There is large uncertainty in associating the seasonal cycle maximum with the onset of the CUP, and the definition of the maximum is very sensitive to the curve-fitting method (Barichivich et al., 2012). The uncertainty in associating the timing of a maximum to the start of the CUP is larger than associating it with the ZCD, especially if the seasonal cycle is characterized by a fairly flat peak, or multiple peaks during the winter (Piao et al., 2008). Hence, previous studies have used the ZCD and their difference as proxies for the onset, termination and duration of the CUP, respectively. However, the period between the ZCD includes the CO_2 release period that does not directly affect the CUP (Fig. 2.1). Therefore, we use the alternate method proposed by Barlow et al. (2015) to determine the timing and duration of the CUP from the first derivative of the mole fraction data, which more closely correspond to the spring maximum and the late-summer minimum times. We then estimate the uncertainty in the different CUP estimates by using the spread of the ensemble members.

For each ensemble member, we calculate the first derivative of the time series as a proxy for the rate of CO_2 uptake or release. The first derivative is at its minimum when CO_2 uptake is most intense and reaches zero at the peak or trough of the seasonal cycle,

i.e., when the sign of the integrated large-scale CO_2 flux changes. However, a peak or a trough (as indicated by zero first derivative Fig. 2.4) might not correspond to the spring maximum or late-summer minimum if the peak is flat or there are multiple peaks in winter. The timing of the CUP should be such that it closely corresponds to the timing of the spring maximum and late-summer minimum.

To determine the onset and termination of the CUP from CO_2 mole fractions, we define a threshold, based on an ensemble of the first derivative of the time series. We define the threshold in terms of the first derivative of the CO_2 dry-air mole fraction measurements analogous to Barlow et al. (2015). The first derivative can be seen as a proxy for the flux (not an exact correspondence, as the seasonal cycle at each site is affected by the atmospheric transport). The threshold is defined as X% of the first derivative minimum, and X is determined separately for the onset and termination of the CUP. The onset/termination of CUP is defined as the closest point to the threshold value before/after the first derivative minimum (Fig. 2.4). The threshold for the onset and termination is chosen such that (1) the uncertainty in the timing of onset and termination is minimized across the ensemble members, and (2) it represents as long a period as possible within the CUP. We varied the value of the parameter X until we find the optimum threshold. When X is 0%, it corresponds to the time period between the seasonal cycle maximum and minimum, including the full CUP, but additional non-CUP periods may be erroneously included due to multiple peaks or flat maxima. By increasing the value of X we remove this error, but can also truncate part of the "actual" CUP. Hence, we try to select a low value of X while reducing the uncertainty in the timing of the CUP.

2.4 Results

For the EFD method, we first optimize the threshold as described in Sect. 2.3.4. By continuously increasing X we found the optimum for the termination is 0%, and for the onset it is 12-13%, with maximum CUP representation and no further reduction in the uncertainty beyond it. To be on the safe side, we chose 15% as the threshold (for onset) in all our analyses. Incidentally, previous studies using flux measurements have also used 15% of the maximum GPP as a threshold to define the start of the growing season (e.g., Wang et al., 2019). The result from varying X in steps between 0%-20% is shown in Fig 2.5. When X is set to 0%, the onset corresponds to the maximum of the seasonal cycle, hence the large spread in CUP onset at BRW and ALT. The interquartile range of 15.0 and 11.2 days respectively can be attributed to the multiple peaks or broad peak of the CO_2 seasonal cycle at these stations. Compared to the onset (30.8 days shown as whiskers of the box plots in Fig.2.5 (a)) the variability in the termination of the CUP is smaller with a maximum range of 3.9 days (whiskers of the box plots in Fig.2.5 (b)).

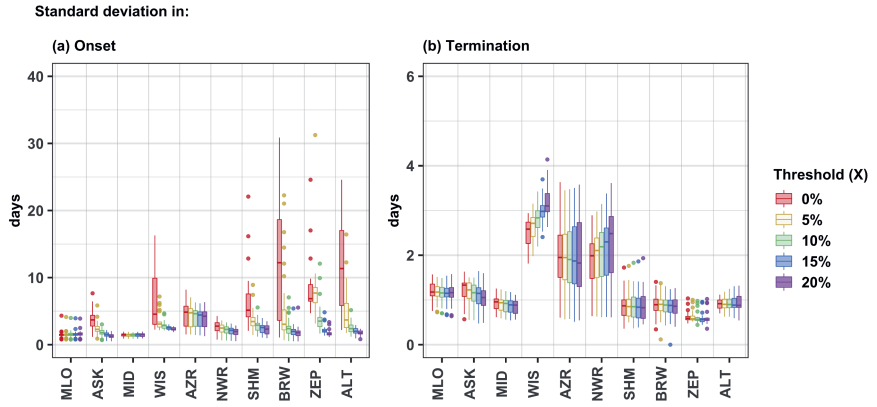


Figure 2.5: Standard deviation (among ensemble members) in the onset (a) and termination (b) of the CUP across years. Differently colored boxes represents different threshold values. The threshold value with X equal to 15% and 0% is chosen for defining the onset and termination of the CUP respectively, for all the studied sites.

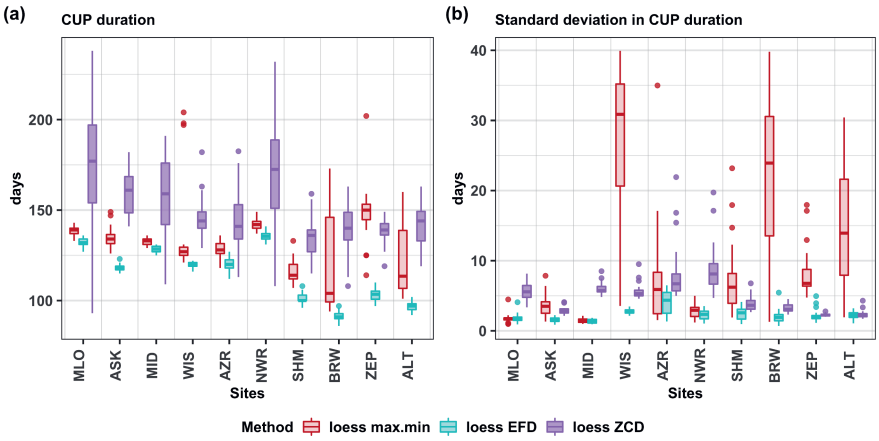


Figure 2.6: Box plot showing the distribution of the (a) median and (b) standard deviation of CUP duration across all years estimated for the loess-fitted residual bootstrap samples using different methods at the studied sites. The median of the CUP duration for a given year is estimated from the ensemble spread for that year. The CUP duration is calculated using three methods, namely, as the period between the seasonal maximum and minimum (loess max.min), the EFD method (loess EFD), and using the ZCD (loess ZCD)).

The standard deviation in the termination is highest at WIS where the median of the box plot for different threshold values is within 2.8 ±0.2 days. Hence, to define the termination, we chose a threshold such that the standard deviation is minimized at WIS. This is achieved when X is set to 0% (the median of the spread is then 2.5 days).

We estimate the duration of the CUP for each year using different approaches: (1) the difference between the seasonal cycle maximum and minimum times, (2) the difference in the ZCD and (3) using the EFD method. Figure 2.6 (a) shows the duration of CUP for all the studied sites across the years (median of the 500 ensemble members), estimated using the three different methods. The size (interquartile range) of the box plots varies strongly across the stations for CUP duration calculated using the ZCD and the maxima and minima. At the lower-latitude stations MLO, MID and NWR, the variability in the CUP duration is larger than at the other stations when using the ZCD ("loess ZCD" in Fig. 2.6 (a)). This is seen in the interquartile range of the "loess ZCD" box plots, with values of 43, 34 and 37 days for MLO, MID and NWR respectively, which is larger than for the other stations (within 15.2 ±5.1 days). The large interquartile range of the CUP-duration estimates using maximum and minimum times at the high-latitude sites BRW (46.75 days) and ALT (32 days) ("loess max.min" in Fig. 2.6 (a)) mainly follows from the large variability in the timing of the seasonal cycle maximum across the ensemble members (Fig. 2.7).

When using EFD method, the CUP estimates have least uncertainty across the ensemble members (Table 2.2). Figure 2.6 (b) compares the standard deviation of the CUP duration across years at all studied sites and methods. The standard deviation is smaller when the EFD method is used for calculating the CUP duration, implying that this metric is better determined. The interquartile range of standard deviation is largest for the method using the dates of the seasonal cycle maximum and minimum, especially at higher-latitude stations like BRW (17 days) and ALT (13.7 days) and lower-latitude station like WIS (17 days). At MLO, MID and NWR, using the ZCD to approximate the CUP duration results in a larger standard deviation (median of the spread is 5.5, 6.7 and 8.1 days respectively) in the CUP duration relative to the other methods used (the median of the spread for the other methods is within 1.75 ±0.6 days).

Here we show that using the EFD method, the uncertainty in the CUP estimate is reduced across all the studied sites. Previous studies (Barichivich et al., 2012; Barlow et al., 2015) also noted the large uncertainty in using the seasonal cycle maximum and minimum to determine the CUP, which is similar to our result (Fig. 2.6 (b)). Therefore this method will not be considered in further analysis here. However, when ZCD is used to approximate CUP duration there is also large uncertainty at the lower latitude stations (e.g. the interquartile range for the 'loess ZCD´ boxplot for MLO is 43 days, Fig. 2.6(a)). Nevertheless, the ZCD is a widely used approach (e.g. Piao et al., 2008;

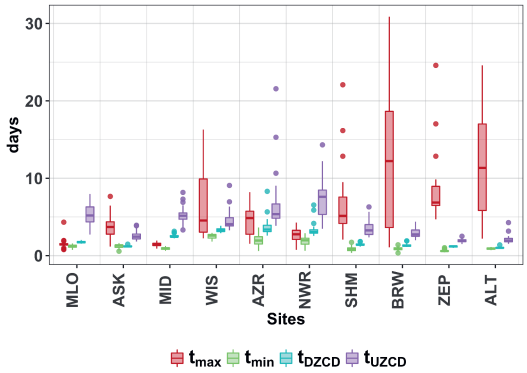


Figure 2.7: Box plots showing the bootstrap standard deviation (i.e., the standard error of estimate) in the timing of the seasonal cycle maximum (t_{max}) and minimum (t_{min}) and upward (t_{UZCD}) and downward (t_{DZCD}) zero-crossing dates across the years for loess fitted residual bootstrap samples. The standard deviation in the timing of the different metrics for a year is estimated from the ensemble spread for the year. In the box plots in this paper, the box denotes the interquartile range (IQR), showing the median with a solid line. The whiskers range from $Q_1$1.5x IQR to Q_3+1.5x IQR, where Q_1 and Q_3 are the 25^{th} and 75^{th} percentiles.

Barichivich et al., 2012, 2013), therefore the EFD method is compared against the ZCD here. The difference between the CUP estimates, using the two different methods (EFD and ZCD) varies from year to year, suggesting that the estimates cannot be corrected by simply adding an offset (Fig. 2.8). The x-axis range, showing the CUP from ZCD in Fig. 2.8, has large year-to-year variation in the CUP, with the largest variation at MLO, NWR and ASK. To further test the robustness of the CUP estimates based on the loess-fitted residual bootstrap method, we compared them against the CUP estimates from an ensemble using the CCGCRV curve-fitting method. Comparable results were obtained when the same CUP estimation method (ZCD/EFD) was applied to the ensemble members using the two different curve-fitting methods (Fig. 2.9 (a)). The CUP duration calculated from the CCGCRV ensemble using the ZCD and the EFD method was within the range of their corresponding estimates from the loess-fitted ensemble members. The mean difference between the median of the "CCG ZCD" and "loess ZCD" estimates in Fig. 2.9 (a) is 1.1 days, and between the median of "CCG EFD" and "loess EFD" estimates, the mean difference is only 0.6. However, the range of box plots corresponding to "loess ZCD" is larger relative to the "CCG ZCD", resulting from the curve-fitting details. In the loess method, the long-term trend in the data is separated by fitting a quadratic polynomial, the decadal variability in the data is then retained which influences the ZCD, leading to more variability in the CUP approximated using the ZCD.

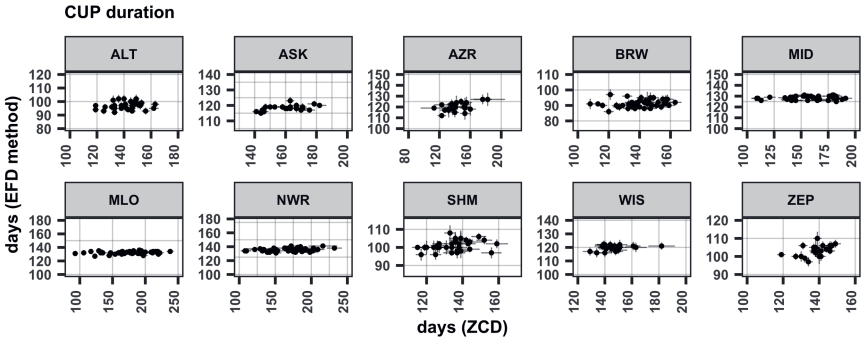


Figure 2.8: CUP duration estimated from the loess-fitted residual bootstrap samples using the timing of the ZCD (x axis) against that estimated using the EFD method (y axis) for different sites (panels). The points show estimates for different years, and the associated error bars show the spread (median ±SD) of the ensemble.

The EFD method is less sensitive to the choice of the curve-fitting method (Fig. 2.9 (a)) shown in the comparable "CCG EFD" and "loess EFD" numbers. Furthermore, we show that for both curve-fitting methods, the standard deviation in the CUP duration estimate across the ensemble members is lowest for EFD method (Fig. 2.9 (b)). Thus, EFD method produces robust results irrespective of the particular curve-fitting method.

The CUP duration approximated using the ZCD shows larger spread for sites like MLO (with an interquartile range of 16 days for CCGCRV fitted data and 43 days for loess fitted data) irrespective of the curve-fitting method used. This is attributed to variability in the UZCD due to the skewness of the seasonal cycle during periods of net release and is similar in both the curve-fitting methods. Furthermore, we find that using the EFD method of CUP estimation resulted in smaller spread across the bootstrap samples for both the curve-fitting methods (Fig. 2.9b). This suggests that the period within the onset and termination defined by the EFD method, which includes only part of the drawdown period, is less variable than the time period between the ZCD, which includes parts of both the drawdown and release periods.

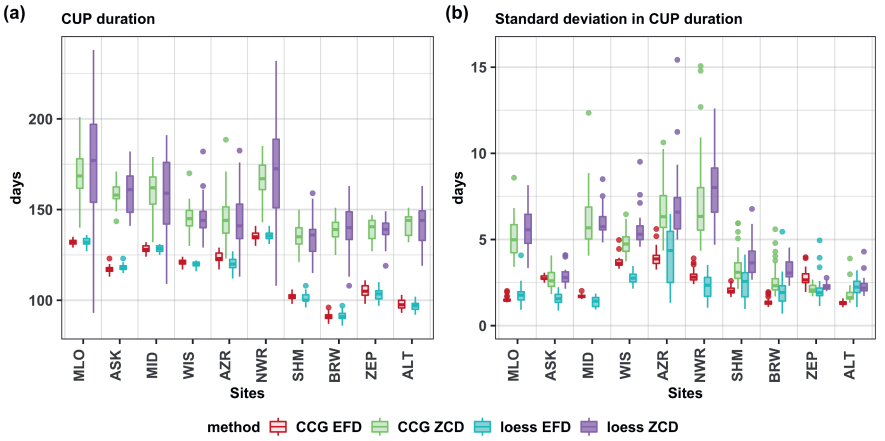


Figure 2.9: Box plot showing the distribution of the (a) median and (b) standard deviation of the CUP duration across years (as described in Fig. 2.6), estimated for the CCGCRV-fitted residual bootstrap samples using the EFD method (CCG EFD, red) and the ZCD (CCG ZCD, green), and for the loess-fitted residual bootstrap samples using the EFD method (loess EFD, blue) and the ZCD (loess ZCD, purple).Note that six outliers (with values between 16 to 30 days) corresponding to AZR in (b) has been removed for ease of visualization.

2.5 Discussion

2.5.1 Uncertainty estimation with EFD method

In this study, we quantify the uncertainty in the CO_2 seasonal cycle curve fitting by creating multiple residual bootstrap samples. The spread of this ensemble provides a measure of the uncertainty in the estimation of seasonal cycle metrics. The ensemble members are consistent with the observational data; hence we consider the variability of the metric estimate across the ensemble as a measure of uncertainty. The ensemble approach allows us to quantify the year-to-year change in different seasonal cycle metrics, and we see that the sensitivity of these metrics to curve fitting differs across latitudes and from year to year. Here we show that CO_2 seasonal cycle metric estimates can be strongly sensitive to the method used; hence any method must be thoroughly evaluated before it can be used to derive trends from the atmospheric data. In Barlow et al. (2015) the robustness of the first derivative is tested by evaluating its ability to capture a known trend from a synthetic time series. They found a larger threshold value for the onset (25%, suggesting a shorter CUP in their approach) from a synthetic data trend analysis in which they applied a linear trend with Gaussian variations of the peak uptake date to a CO_2 time series. However, we argue that the data-derived year-to-year uncertainty

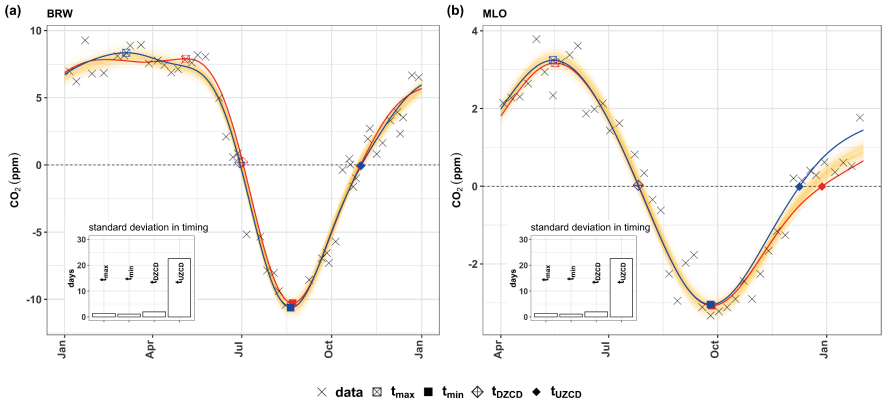


Figure 2.10: Fitted bootstrap samples (thin yellow lines) representing the seasonal cycle of a year at (a) BRW and (b) MLO. The observational data of the corresponding time period are shown with '×'. Red and blue curves in (a) and (b) highlight two random ensemble members that differ in shape and are marked with the timings of the seasonal cycle maximum (t_{max}), minimum (t_{min}), downward zero-crossing(t_{DZCD}) and upward zero-crossing (t_{UZCD}), with the corresponding symbols as in the legend. The vertical bars in the inset show the standard deviation of the labeled metric estimates across the ensemble members.

from our ensemble provides a more robust threshold estimate and we derived a tighter threshold than Barlow et al. (2015) (15% for onset). Further, Barlow et al. (2015) showed that their method can retrieve the true linear trend to within 10-25%. Our EFD approach provides uncertainty on the year-to-year variability in the seasonal cycle metrics based on the fitted data residuals, which could be used in a trend analysis to give differential weights to each year. Also, trend analysis on the individual ensemble members would allow uncertainty on the trend to be calculated. Our demonstration of the EFD method on the CUP could be extended to other metrics that are derived directly from the seasonal cycle in a similar way, for example the peak-to-trough amplitude, especially when curve-fitting discrete data, at sites with broader or multiple peaks. In a similar fashion, the ensemble-based approach could be used to evaluate a newly proposed method or select an optimal method for evaluating any other metric based on reduced uncertainty. The EFD approach, based on residual bootstrapping, assumes that the residuals are independent and as such may not be appropriate for hourly or daily in situ data. There is considerable auto-correlation between consecutive days in daily measurements, limiting the number of independent events to five or six per month, which is comparable to the scale of our weekly measurements. The uncertainties in curve fitting related to gaps in the data are also lower in the case of more frequent measurements.

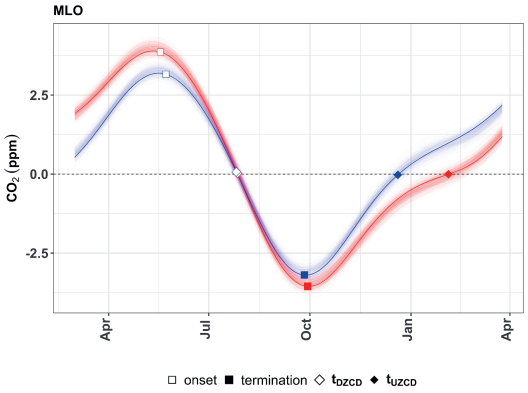


Figure 2.11: Bootstrap samples representing the seasonal cycle of 2 years (red and blue) with largely different CUP timing when estimated with the two methods (a case taken from Fig 2.8). Thin red and blue lines represent the ensemble spread for the 2 years. The thicker red/blue lines represent a random ensemble member from each year, and these are marked with the timings of the onset and termination as determined by the EFD method (squares) and the ZCD (diamonds).

2.5.2 Latitudinal dependence of metrics

The shape of the CO_2 seasonal cycle varies with latitude. At the higher-latitude stations the seasonal cycle has a broader peak or multiple peaks in winter, and the timing of the seasonal cycle maximum cannot be interpreted as the onset of the CUP. Further, our analysis shows that there is large uncertainty in the timing of the seasonal cycle maximum (Fig. 2.7) at higher-latitude stations, which is in agreement with previous studies (e.g., Barichivich et al., 2012; Piao et al., 2008; Barlow et al., 2015). For example, for BRW shown in Fig. 2.10 (a) the atmospheric mixing ratios have a nearly constant value from January to May followed by a decrease in CO_2 until a minimum is reached in August, also illustrated in Barlow et al. (2015) (their Figure 6). If the seasonal cycle were determined solely by the biospheric fluxes, then the onset and termination of the CUP would be marked by the timing of the seasonal cycle maximum and minimum respectively (Barichivich et al., 2012). However, it can be noted that the estimated timing of the seasonal cycle maximum varies greatly across the bootstrap samples in BRW (inset of Fig. 2.10 (a)), where the seasonal cycle is characterized by a flat peak. An earlier peak is likely to be associated with a flat maximum or multiple peaks that may result from transport (Parazoo et al., 2008) or other fluxes, rather than indicating the onset of the uptake period (Barlow et al., 2015). The timing of the ZCD at BRW is consistent across the ensemble members, which suggests that the timing of the ZCD (upward and downward) is less ambiguous. Other higher-latitude sites like ALT, SHM

and ZEP and lower-latitude sites like ASK, WIS and AZR exhibit similar seasonal cycles, characterized by flat or multiple peaks and less ambiguous ZCD. However, the ZCDs are closer to the timing of the maximum uptake and release of CO_2 (Manning, 1993) than to the actual onset and termination of the CUP. For example, in Fig. 2.1, the onset of the CUP occurs in June; however the downward zero crossing occurs in early July, and thus the CUP approximated using the ZCD explicitly excludes the start of the drawdown period.

At lower-latitude stations like MLO, MID and NWR, we find that the ZCDs can vary across ensemble members as shown in Fig. 2.7 and in such cases the ZCD are clearly not the best proxy for estimating the duration of the CUP. This is especially the case for the time series at MLO (Fig. 2.10 (b)), which shows relatively a large spread of 5 days (median of the ensemble spread, rounded to the nearest integer) in the timing of the UZCD across the ensemble members. The seasonal cycle at MLO has well-defined peaks and troughs; hence the timings of the seasonal cycle maximum and minimum show only a small spread of 1 day (median of the ensemble spread, rounded to the nearest integer) across the bootstrap samples (inset of Fig. 2.10 (b)). In this case, the EFD method gives a more robust estimate of the CUP duration.

We find that in addition to having a larger annual uncertainty, the range of CUP values over the study period for the ZCD approach is much larger than that of the EFD approach for some sites (Fig. 2.8). For example, at MLO the zero-crossing-approximated CUP ranges from 100 to 250 days, corresponding to a period of 3-8 months. Changes in the length of the growing season in the Northern Hemisphere are not expected to be this large. As an example, Jeong et al. (2011) estimated the length of the growing season using satellite measurements of the normalized difference vegetation index (NDVI). When integrating over the temperate Northern Hemisphere, the length of the phenology-derived growing season was found to vary by less than 25 days from 1982-2008. The ZCD approach includes changes in both the latter part of the net uptake period and the early-release period, making it difficult to separate the contribution of the net uptake and net release periods to the changes in the CUP estimate. To understand this large spread in CUP, we compare two years with very different CUP values estimated by the ZCD at MLO, 1992 with 192 days and 1998 with 147 days (Fig 2.11). We find that the difference in the CUP estimate is due to the change in the early-release period, whereas the uptake periods are essentially the same. When using the EFD method, by contrast, the 2 years show similar CUP, 134 and 126 days, respectively. By definition, the EFD is not affected by differences in the net release period and therefore provides more robust CUP duration estimates.

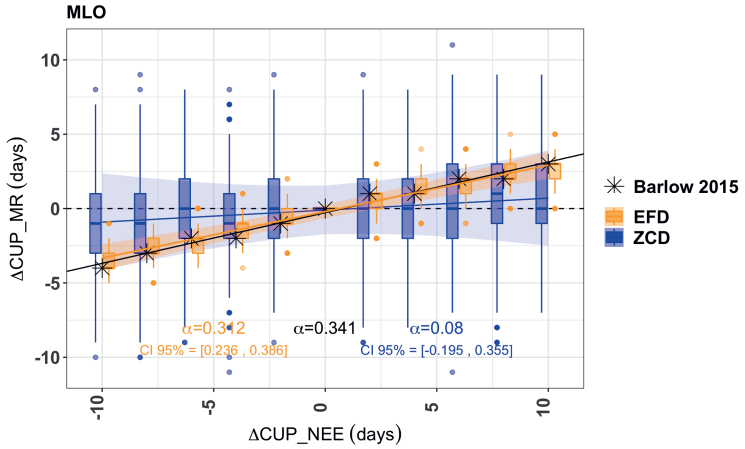


Figure 2.12: Sensitivity of the EFD (orange), ZCD (blue) and an approach similar to that of Barlow et al. (2015) (black asterisks) to imposed changes in the CUP_NEE. The deduced change in the CUP based on the simulated mixing ratio ΔCUP_MR is shown here for MLO. The spread of the boxplot for the EFD and ZCD methods corresponds to the uncertainty in the curve fitting estimated by the residual ensemble. The uncertainty in the sensitivity of the EFD and ZCD methods is estimated as described in Sect. 2.5.3 with multiple regression fits. The shaded region represents the 95% confidence interval (CI) of the fitted lines. The mean slope (α) of the fitted regression lines and their 95% CI are shown.

2.5.3 Sensitivity of different methods to changes in the CUP

To test the sensitivity of the different methods to changes in the CUP, we performed a synthetic data experiment. experiment. We compare the EFD and ZCD methods and additionally an approach where we determine the CUP using a 25% threshold as in Barlow et al. (2015) but using a single loess curve fitting rather than an ensemble. We manipulated the posterior net ecosystem exchange (NEE) flux by imposing predefined CUP changes (Δ CUP_NEE) for land pixels in the Northern Hemisphere that have a clearly defined seasonal cycle, using a randomly selected baseline year from the Jena Carboscope CO_2 Inversion (Rödenbeck et al., 2003) (version ID: sEXT_ocNEET_v2021). The manipulated fluxes were then transported forward using an atmospheric transport model (TM3 (Heimann & Körner, 2003)). We then sampled the atmospheric mixing ratios at time steps corresponding to flask data measurements at the station locations. Then, we evaluated the CUP changes deduced from the simulated CO_2 mixing ratio (ΔCUP_MR) in response to the imposed ΔCUP_NEE with the three different CUP estimation methods. The experiment shows that the EFD method is more sensitive to the changes in CUP_NEE compared to the ZCD method (Fig. 2.12), which is seen by the

higher slope of ΔCUP_MR to ΔCUP_NEE (0.312 vs. 0.08, respectively). Further, the uncertainty in the sensitivity of the ZCD and EFD methods was estimated by calculating the 95%confidence intervals of the slopes of the regression lines by fitting multiple (10000) sets of randomly resampled CUP_MR values (from its distribution) corresponding to each CUP_NEE value (shown in Fig.2.12 for MLO). The confidence interval is large for the ZCD method, from -0.195 to 0.355. This implies that ΔCUP_NEE cannot be reliably inferred from ΔCUP_MR using the ZCD. Further, we observed that the approach in Barlow et al. (2015) is similarly sensitive to changes in CUP_NEE as the ensemble-based approach; however the uncertainty in its sensitivity cannot be calculated as only a single CUP_MR value is available for every CUP_NEE, clearly showing the advantage of the ensemble approach to constrain uncertainties in metrics.

As seen from the experiment, the ZCD is the least sensitive to changes in the flux. Hence, years with extreme CUP approximated by the ZCD as in Fig.2.8 may not indicate actual changes in the CUP but rather other factors, like reduced net respiration in the early-release period, which postpone the UZCD. This shift could be due to reduced net respiration in the early-release period, prolonging the time to reach the UZCD. This change is determined by the interplay of the CO_2 uptake and release processes, which are influenced by physical factors like temperature, soil moisture and solar radiation. For example, in dry conditions there is less respiration by plants and slower decomposition of organic matter in the soil, resulting in reduced CO_2 release to the atmosphere (Yan et al., 2018). The rate of decomposition further depends on the snow cover and available detritus content in the soil following leaf senescence. Furthermore, in the early-release period, when the solar radiation is not limiting, plants may continue to photosynthesize depending on water availability and temperature, leading to reduced net CO_2 release. Thus, in years with extreme CUP as approximated by the ZCD, the physical processes that affects the release period should be investigated. In comparison to the CUP definition, the approximation by ZCD is also sensitive to variations after the summer minimum, i.e., during the early-release period.

The EFD and the approach in Barlow et al. (2015), which consider the first derivative of the concentration time series as a proxy for the large-scale spatially integrated flux (Barlow et al., 2015), are relatively more sensitive to the flux changes. However, the inferred changes cannot be directly translated to the underlying flux fields. The concentration time series do not exactly replicate the changes imposed in CUP_NEE, as these changes do not occurr simultaneously across the Northern Hemisphere, and hence do not represent a single changed flux but a superposition of many. These signals dampen each other when aggregated in CUP_MR, as seen in Fig. 2.12.

The synthetic experiment presented here used simulated data from only 1 year, thus controlling for the influence of inter-annual variability in atmospheric transport. In reality,

atmospheric transport plays an important role in explaining a significant portion of observed CO_2 variations at surface stations (e.g. Krol et al., 2018; Fu et al., 2015), which might affect any interpretation of the CUP metrics. An extensive study was carried out by Lintner et al. (2006), confirming the importance of atmospheric transport to account for some of the inter-annual variations in CO_2 observed at Mauna Loa. Murayama et al. (2007) showed how year-to-year changes in the atmospheric transport create significant inter-annual variations in the downward zero-crossing date of the CO_2 seasonal cycle that cannot be neglected. The ZCD is influenced by transport variability in both the late uptake and early-release periods. Hence, changes in the early-release period could be erroneously interpreted as changes in the CUP when using the ZCD. Also, atmospheric transport can contribute to the inter-annual variability in CUP estimates when using the EFD method. Hence, we recommend that the contribution of atmospheric transport at the studied background sites should be evaluated before interpreting and relating the CUP metrics to sources/sinks.

2.6 Conclusions

Here, we discuss a method for estimating the timing, duration, and uncertainty of the CUP and related metrics from a discrete time series of CO_2 dry-air mole fraction data. The uncertainty in the metrics is quantified using an ensemble of fitted time series generated through residual bootstrap sampling, a novel addition to the method presented in Barlow et al. (2015). Previous studies have used the timing of the ZCD as a proxy for defining the CUP; however the timing of the UZCD is influenced by the shape of the seasonal cycle, leading to large variability in the estimated CUP duration across the ensemble members for a given year for some of the studied sites, particularly at lower latitudes. The spread in the CUP duration across the ensemble members for a given year (i.e., the annual uncertainty) is lower for all studied sites when calculated using the EFD method. The EFD method depends directly on the timing and rate of the maximum CO_2 uptake; hence the method is not affected by the shape change of the seasonal cycle outside the time period during which the CO_2 uptake is larger than the CO_2 release. Further, a synthetic data experiment showed that the approaches based on the first derivative of the CO_2 mixing ratio are more sensitive to changes in CUP evaluated at MLO than the ZCD method. With the EFD method, the onset and termination are tightly constrained by considering the year-to-year change in the seasonal cycle. To test the impact of the curve-fitting method used, we generated bootstrap samples using both loess-fitted residuals and CCGCRV. The CUP duration estimated using the EFD method results in smaller spread for both curve-fitting methods. Further, for both curve-fitting methods, the standard deviation in the estimates across the ensemble members is smaller when using the EFD method, suggesting that the EFD method gives robust estimates. Thus, the EFD method allows for a robust estimate of the CUP that better reflects the CO_2 drawdown period.

This approach could be extended to other metrics of seasonal cycle analysis or to other curve-fitting methods, as was shown with the comparison to the CCGCRV results.

Table 2.2: The inter-quartile range of the standard deviation in the CUP duration across all years as described in Fig. 2.6 (b), rounded to the nearest integer (day). Values are given for three different method of estimation for each site.

Sites	Time period	sd CUP duration (days)	Method
MLO	1977-2017	1-2	max.min
		1-2	EFD method
		5-6	ZCD
ASK	1996-2018	3-4	max.min
		1-2	EFD method
		2-3	ZCD
MID	1986-2018	1-2	max.min
		1-2	EFD method
		5-6	ZCD
WIS	1996-2018	21-35	max.min
		2-3	EFD method
		5-6	ZCD
AZR	1996-2018	2-8	max.min
		3-5	EFD method
		6-8	ZCD
NWR	1976-2018	2-3	max.min
		2-3	EFD method
		7-10	ZCD
SHM	1986-2018	4-8	max.min
		2-3	EFD method
		3-4	ZCD
BRW	1972-2017	14-31	max.min
		1-2	EFD method
		3-4	ZCD
ZEP	1995-2018	6-9	max.min
		1-2	EFD method
		1-2	ZCD
ALT	1986-2017	8-22	max.min
		2-3	EFD method
		1-2	ZCD

Chapter 3

Limitations in the use of atmospheric CO_2 observations to directly infer changes in the length of the biospheric carbon uptake period

This chapter is based on:

Kariyathan, T., Bastos, A., Reichstein, M., Peters, W., & Marshall, J. (2025). Limitations in the use of atmospheric CO_2 observations to directly infer changes in the length of the biospheric carbon uptake period. Atmospheric Chemistry and Physics, 25, 7863-7878, doi:10.5194/acp-25-7863-2025.

3.1 Abstract

The carbon uptake period (CUP) refers to the time of each year during which the rate of photosynthetic uptake surpasses that of respiration in the terrestrial biosphere, resulting in a net absorption of CO_2 from the atmosphere to the land. Since climate drivers influence both photosynthesis and respiration, the CUP offers valuable insights into how the terrestrial biosphere responds to climate variations and affects the carbon budget. Several studies have assessed large-scale changes in CUP based on seasonal metrics from CO_2 mole fraction measurements. However, an in-depth understanding of the sensitivity of the CUP as derived from the CO_2 mole fraction data (CUP_{MR}) to actual changes in the CUP of the net ecosystem exchange (CUP_{NEE}) is missing. In this study, we specifically assess the impact of (i) atmospheric transport, (ii) inter-annual variability in CUP_{NEE} and (iii) regional contribution to the signals that integrate at different background sites where CO_2 dry air mole fraction measurements are made. We conducted idealized simulations where we imposed known changes (Δ) to the CUP_{NEE} in the Northern Hemisphere to test the effect of the aforementioned factors in CUP_{MR} metrics at 10 Northern Hemisphere sites. Our analysis indicates a significant damping of changes in the simulated ΔCUP_{MR} due to the integration of signals with varying CUP_{NEE} timing across regions. CUP_{MR} at well-studied sites such as Mauna Loa, Utqiaġvik (formerly Barrow), and Alert showed only 50% of the applied ΔCUP_{NEE} under non-interannually varying atmospheric transport conditions. Further, our synthetic analyses conclude that interannual variability (IAV) in atmospheric transport accounts for a significant part of the changes in the observed signals. However, even after separating the contribution of transport IAV, the estimates of surface changes in CUP by previous studies are not likely to provide an accurate magnitude of the actual changes occurring over the surface. The observed signal experiences significant damping as the atmosphere averages out non-synchronous signals from various regions.

3.2 Introduction

Terrestrial ecosystems constitute a net sink of carbon from the atmosphere, mediated by the interplay between photosynthesis and respiration (autotrophic and heterotrophic). The period between the dates when an ecosystem transitions from being a carbon source to a carbon sink and vice versa is referred to as the carbon uptake period (CUP) (Gonsamo et al., 2012). During the Northern Hemisphere's CUP, a continuous decline can be observed in atmospheric CO_2 mole fraction in many sites across the globe. The CUP as defined by net ecosystem exchange (NEE) will be referred to as CUP_{NEE} and the corresponding period in the CO_2 mole fraction data will be referred to as CUP_{MR}. The timing and duration of the CUP_{NEE} and CUP_{MR} are influenced by vegetation phenology and soil respiration, which are in turn influenced by climate variability (Gill et al., 2015; Piao et al., 2019). For example, in northern boreal and temperate ecosystems, warmer temperatures trigger early snowmelt and an associated early onset of plant growth in spring (Buermann et al., 2018; Zhou et al., 2020). In autumn, warm temperatures lead to delayed leaf senescence and a longer growing season (Piao et al., 2019; Shen et al., 2022). However, warmer temperatures can also enhance soil respiration if soil moisture is not limiting, and potentially result in earlier termination of the CUP_{NEE} and CUP_{MR} (Piao et al., 2008). The timing of the CUP_{MR} integrates the signal of ecosystem changes over large spatial scales. Metrics associated with CUP, e.g., its amplitude have been attributed to Northern Hemisphere greening (e.g. Forkel et al., 2016; Keeling et al., 1996; Barichivich et al., 2013) and to the intensification of the land carbon sink over the past decades (e.g. Graven et al., 2013; Ciais et al., 2019).

In previous studies (e.g. Fu et al., 2017, 2019), the CUP_{NEE} has been derived from eddy-covariance measurements of net CO_2 fluxes. However, estimation of the CUP_{NEE} using eddy-covariance flux measurements remains challenging on a global scale due to the uneven distribution of flux towers over the globe and the small spatial area covered by the footprint of these towers (Jung et al., 2020; Walther et al., 2022). Therefore, several studies have explored the potential of remote sensing to estimate the CUP_{NEE} (Churkina et al., 2005; Zhu et al., 2012; Gonsamo et al., 2012). However, while satellite-based indices provide information about the overall health and activity of vegetation, they cannot distinguish between different components of the carbon cycle, such as gross primary production and ecosystem respiration. In drought-stressed ecosystems, there may even be periods of carbon release during the growing season (Churkina et al., 2005; Zhu et al., 2012; van der Woude et al., 2023b), influencing CUP_{NEE}. The satellite-based indices are closely related to vegetation growth or photosynthesis and characterize the start and end of the growing season (Wang et al., 2022; Zeng et al., 2020), but they do not necessarily capture CUP_{NEE}.

Measurements of atmospheric CO_2 dry air mole fraction from remote background

sites represent the balance between surface emissions and uptake from land and ocean (Keeling et al., 1996) over large spatial scales. The seasonal patterns evident in these data from the Northern Hemisphere reflect the terrestrial ecosystem exchange, mostly from the high and mid-latitudes, and have been used by previous studies to investigate the changes in the CUP_{NEE} over large spatial scales (e.g. Barichivich et al., 2012; Piao et al., 2008, 2017). Robust methods were developed for the estimation of the CUP from the CO_2 mixing ratio, such as the ensemble of first derivative (EFD) method from Kariyathan et al. (2023), which was better able to identify changes in the CUP_{NEE} compared to the conventional use of the dates when the detrended seasonal cycle crossed the zero value. Even with refined CUP_{MR} estimation methods, atmospheric transport causes a significant fraction of observed CO_2 variations at surface stations. Interannual variations and long-term trends in atmospheric transport can affect the relationship between the seasonal cycle of atmospheric CO_2 observations and surface exchange (Murayama et al., 2007; Piao et al., 2008). For example, Jin et al. (2022) studied the impact of varying winds and ecological CO_2 fluxes on seasonal cycle amplitude trends, finding that shifting winds partially offset the amplitude increase at MLO, contributing nearly 50% to the seasonal cycle amplitude changes between 1959 and 2019. Lintner et al. (2006) suggest a contribution by atmospheric transport to the downward trend in the CO_2 seasonal cycle amplitude observed at MLO between 1991 and 2002. Murayama et al. (2007) demonstrated how year-to-year changes in atmospheric transport create significant interannual variations in the downward zero-crossing date of the CO_2 seasonal cycle, inevitably influencing CUP_{MR} estimates. Previous studies have primarily focused on aspects such as the seasonal cycle amplitude or zero-crossing times. Barlow et al. (2015) used the improved CUP estimation method to explore the influence of transport on CUP timing to some extent. In this study, we aim to understand in detail how well the CUP_{MR} deduced from atmospheric time series observations of CO_2 mixing ratios represents the CUP_{MR} changes from the Northern Hemisphere biosphere and its interannual variability (IAV), especially:

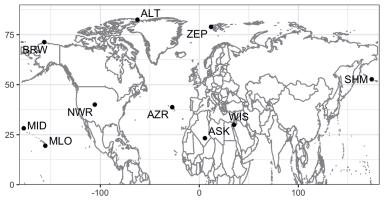
1 To what extent do CO_2 mixing ratio observations accurately capture variations in CUP_{NEE}?

2 How does IAV in atmospheric transport affect the observed changes in CUP_{MR}?

3 Considering the variability in both CUP_{NEE} and transport, can CUP_{MR} effectively reflect long-term trends in CUP_{NEE}?

4 Can the changes observed at the studied sites be attributed to specific regions of the Northern Hemisphere?

To address these questions, we evaluate the role of transport in shaping the CUP_{MR} at regional and global scales by conducting a series of experiments using the atmospheric transport model TM3 (Heimann & Körner, 2003) for a total of 10 sites in the Northern Hemisphere (Fig. 3.1).



Station code	Station name
MLO	Mauna Loa, Hawaii, United States,
ASK	Assekrem, Algeria
MID	Sand Island, Midway, United States
WIS	Weizmann Institute of Science at the Arava Institute, Ketura, Israel
AZR	Terceira Island, Azores, Portugal
NWR	Niwot Ridge, Colorado, United States
SHM	Shemya Island, Alaska, United States
BRW	Barrow Atmospheric Baseline Observatory,United States
ZEP	Ny-Ålesund, Svalbard, Norway and Sweden
ALT	Alert, Nunavut, Canada

Figure 3.1: Map showing the location of studied sites, with the station names corresponding to the station code shown in the map.

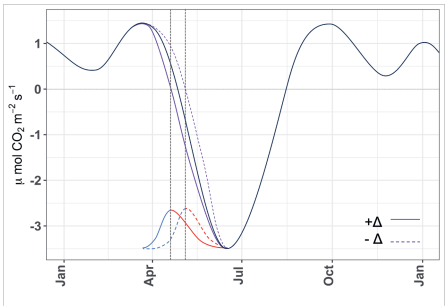


Figure 3.2: Schematic showing manipulation of CUP_{NEE}. The shifted purple solid/dashed curves result in $+\Delta$ and $-\Delta$ changes in the CUP_{NEE}, respectively. The curve is obtained by subtracting/adding two half-Gaussian curves. For example, the red and blue curves combine at the points (i.e., new onset) indicated by the dashed black lines to produce the purple curves (described in Sect. 3.3.3). The seasonal cycle minimum separates the early (left) and late (right) CUP_{NEE} phases. The manipulation for the early CUP_{NEE} phase is shown here and can be similarly applied to the late CUP_{NEE} phase.

3.3 Methods

To evaluate the degree to which CUP_{MR} represent the changes in the CUP_{NEE}, when influenced by atmospheric transport, we design idealized scenarios with prescribed changes to the optimized NEE fluxes from the Jena CarboScope Atmospheric CO_2 Inversion (Rödenbeck et al., 2003) (version ID: sEXTocNEET_v2021). The modifications were applied solely to pixels in the Northern Hemisphere ($> 0°$ N) with a clearly defined seasonal cycle, characterized by a seasonal cycle minimum, and downward and upward zero-crossing points in spring and autumn, respectively. The year 2003 is employed as the reference year (simulations with an alternative reference year, 2001, did not show a noticeable difference), and pixels exhibiting clearly defined seasonal cycles in that specific year were chosen for perturbation. For the remaining pixels, the reference year flux was repeated over time, so that there was no IAV in CUP_{NEE}. This was done to ensure that any observed changes in the simulated CO_2 mixing ratio could be attributed to the prescribed Δ. The influence of fossil fuel, biomass burning, and ocean fluxes on the seasonal variation of atmospheric CO_2 is minimal, and changes in the seasonal cycle of atmospheric CO_2 reflect alterations in the integrated net ecosystem exchange in the Northern Hemisphere (Barichivich et al., 2012). While these fluxes were not modified in our simulations, our results are based on differences between simulations where only the NEE flux is altered. The flux manipulation was carried out from 1995 to 2017, aligning with the meteorological forcing used in the transport model. These adjusted fluxes were then transported forward using an atmospheric transport model, TM3 (Heimann & Körner, 2003), simulating time series of CO_2 mixing ratios at different study sites (as shown in Fig. 3.1), in temporal frequency aligning with the flask measurements at the sites. The 10 sites chosen for this study represent a selected subset of the Northern Hemisphere observation network. To minimize anthropogenic influences, only remote background sites were included. These sites were selected based on their long-term data records and their spatial distribution across the Northern Hemisphere, with roughly at least one station per 10° latitude, capturing the network's spatial diversity. Previous studies, such as Murayama et al. (2007) and Piao et al. (2008), have confirmed that interannual variations and long-term trends in atmospheric transport can affect the relationship between the seasonal cycle of atmospheric CO_2 observations and surface exchange. These studies also used a subset of background sites to evaluate transport influence on observed signals, similar to our approach. After the forward transport run, we assess CUP_{MR} changes based on the simulated CO_2 mixing ratios (ΔCUP_{MR}) resulting from ΔCUP_{NEE}. We use the EFD method from Kariyathan et al. (2023) to evaluate CUP_{MR}, as its efficacy on the sites shown in Fig.3.1 was previously established in Kariyathan et al. (2023). The method uses an ensemble-based approach to quantify the uncertainty associated with curve-fitting discrete time series data and deriving seasonal cycle metrics. Using this approach, an optimal threshold is defined based on the first derivative of the CO_2 seasonal cycle to determine CUP timing. The threshold is selected

Table 3.1: Description of different forward simulation experiments, using manipulated NEE fluxes. The first character in the experiment name indicates if the early (E) or late (L) $\mathrm{CUP_{NEE}}$ phases are manipulated, the next character specifies if Northern Hemisphere (N) or Regional (R) fluxes are adjusted and the subscript and superscript of the last character denote variability (V) in $\mathrm{CUP_{NEE}}$ and transport respectively. The Δ applied in each experiment is shown in the first column. In $\Delta_x^d\mathrm{CUP_{NEE}}$, x ranges from -10 to +10 days in intervals of 2 days. In $\Delta_x^l\mathrm{CUP_{NEE}}$, x can be a sequence from -10 to +10 days and vice versa denoted by p and n respectively in the main text.

Δ $\mathbf{CUP_{NEE}}$	Period	Spatial Structure	$\mathbf{CUP_{NEE}}$	Transport	Experiment
Discrete (Δ_x^d)	Early (E)	Northern Hemisphere (NH)	Fixed (V_0)	Fixed (V^0)	ENV_0^0
				IAV (V^T)	ENV_0^T
		Regional (R)	Fixed	Fixed	ERV_0^0
				IAV	ERV_0^T
	Late (L)	Northern Hemisphere	Fixed	Fixed	LNV_0^0
				IAV	LNV_0^T
		Regional	Fixed	Fixed	LRV_0^0
				IAV	LRV_0^T
Linear (Δ_x^l)	Early	Northern Hemisphere	Fixed	IAV	ENV_0^T
	Late	Northern Hemisphere	Fixed	IAV	LNV_0^T
	Early	Northern Hemisphere	IAV (V_1)	IAV	ENV_1^T
		Regional	IAV	IAV	ERV_1^T
	Late	Northern Hemisphere	IAV	IAV	LNV_1^T
		Regional	IAV	IAV	LRV_1^T
	Early	Northern Hemisphere	2 times IAV (V_2)	IAV	ENV_2^T
	Late	Northern Hemisphere	2 times IAV	IAV	LNV_2^T

such that the CUP timing closely corresponds to the spring maximum and late summer minimum, with minimal influence from curve-fitting uncertainty caused by multiple or broader peaks in the CO_2 seasonal cycle.

To evaluate how well CUP_{MR} captures the changes in CUP_{NEE}, we used experiments ENV_0^0 and LNV_0^0, where we imposed spatially uniform, discrete changes in CUP_{NEE} (Δ^d) and the atmospheric transport was held constant in the forward transport run (meaning that one year (2008) of transport was repeated). Then, to answer how the IAV in atmospheric transport affects derived CUP_{MR}, the CO_2 mixing ratios were simulated with interannually varying meteorology (experiment ENV_0^T and LNV_0^T). To evaluate the ability of CUP_{MR} to reflect long-term trends in CUP_{NEE}, we initially assessed the ability to capture a trend in CUP_{NEE} while accounting for IAV in atmospheric mixing. This was achieved by prescribing long-term trends in $CUP_{NEE}(\Delta^l)$ and conducting the forward transport run with interannually varying meteorology. Subsequently, we then tested the detectability of prescribed linear trends in CUP_{NEE} (Δ^l) when IAV was present in both atmospheric transport and NEE (experiments ENV_1^T and LNV_1^T). Additionally, to analyze the influence of IAV in CUP_{NEE}, we prescribed known IAV to CUP_{NEE} (experiments ENV_2^T and LNV_2^T). Further, to understand the sensitivity of the simulated signals to regional changes (experiments ERV_0^0, LRV_0^0, ERV_1^T and LRV_1^T), we limited the flux manipulation to Northern Hemisphere land regions of the TransCom3 (Gurney et al., 2002) experiment, namely Europe, Eurasian Temperate, Eurasian Boreal, North American Temperate and North American Boreal. The experiments performed are listed in Table 1.

3.3.1 NEE flux manipulation

The CUP_{NEE} is the period when the NEE flux is negative, and the downward and upward zero-crossing dates represent the onset and termination of the CUP_{NEE} respectively. Hence, we shift the NEE zero-crossing dates to have a change Δ (where Δ is measured in days) in the CUP_{NEE} duration (ΔCUP_{NEE}). The NEE flux is characterized by daily temporal resolution, showing relatively gradual variations along the y-axis compared to the x-axis. For all the experiments performed, the NEE values (i.e., y-axis) are modified to achieve the desired timing adjustments (Δ) in CUP_{NEE}, without altering the time axis itself. This adjustment ensures the creation of a smooth curve that closely mirrors the actual flux while achieving the intended change in CUP_{NEE}. For each value of ΔCUP_{NEE}, we modify the downward and upward zero-crossing dates of NEE separately to evaluate the effect of changes in the early and late CUP_{NEE} phases, respectively. This is achieved by adding or subtracting a continuous curve to the period extending from the peak in spring to the NEE minimum for early phase changes and the period from the NEE minimum to peak in winter for late phase changes. The curve is created by combining two distinct half Gaussian curves (Fig. 3.2, red and blue curves): the first curve has its peak

at the new onset/termination and a standard deviation (σ_1) equal to one-third of the distance between the NEE peak in spring/winter and the new onset/termination. The second curve, also with its peak at the new onset/termination, has a different standard deviation (σ_2) equal to one-third of the distance between the new onset/termination and the date corresponding to the NEE minimum value. This configuration (i.e., Gaussian peaks and σ) ensures that the Gaussian tail minimizes any shift around the NEE peak and trough while realizing the Δ shift at the onset or termination of the $\mathrm{CUP_{NEE}}$.

Some pixels exhibit a distinct seasonal pattern without a well-defined peak in spring or winter. In those cases, the period for manipulating the early and late CUP phases then extends from the beginning of the year to the day of minimum NEE and from the day of minimum NEE to the end of the year, respectively. The portions of the first and second curves corresponding to the range from "μ - $3\sigma_1$" to "μ" and from "μ" to "$\mu + 3\sigma_2$," respectively, are then combined and smoothed using a spline function (Fig. 3.2, purple curves).

We note that the annual flux is not conserved in the manipulation. However, we detrend the simulated CO_2 mixing ratio prior to $\mathrm{CUP_{MR}}$ analysis, which would remove any trend in the CO_2 mixing ratio caused by repetition of the manipulated years. Further, when evaluating the simulated CO_2 time series, we found that the change in the total annual flux only changes the peak-to-peak amplitude and does not influence the timing and duration of the simulated time series, except at times corresponding to periods of manipulation in the $\mathrm{CUP_{NEE}}$. This happens for instance, when the downward zero crossing of the NEE flux is manipulated: it changes only the CUP onset and has minimal influence on the CUP termination in the CO_2 mixing ratios. The different cases of manipulation are described below.

1. Δ_x^d: In these simulations, every year has the same discrete change in $\mathrm{CUP_{NEE}}$. In the different experiments, the magnitude of the shift (denoted by x) ranges from -10 to 10 days in intervals of 2 days.

2. Δ_x^l: In these simulations, $\Delta\mathrm{CUP_{NEE}}$ progresses from -10 days to +10 days (denoted by $x = p$) or vice versa (denoted by $x = n$) over the period of manipulation.

Manipulation Δ_x^d is done for experiments where there is no IAV in $\mathrm{CUP_{NEE}}$, indicated by V_0 in the experiment name. Δ_x^l manipulation is made for experiments with and without IAV in $\mathrm{CUP_{NEE}}$ (i.e., experiment names with V_0, V_1 and V_2). For the case V_0, the manipulation is done on the flux of a reference year (2003 chosen arbitrarily), which is repeated in time so that there is no IAV in $\mathrm{CUP_{NEE}}$. Any IAV in $\mathrm{CUP_{MR}}$ may then be attributed to IAV in transport. In V_1, the annual fluxes are used instead of repeating the base year flux. The case V_2 has a prescribed IAV in $\mathrm{CUP_{NEE}}$. In this case, for a given pixel, a set of Δ values is added to the original $\mathrm{CUP_{NEE}}$ in the manipulation period

(2000-2017). The set of Δ has a mean zero and a standard deviation twice that of the IAV in the original CUP_{NEE} for the manipulation period.

The flux alteration is complicated to apply in some cases, as described below.

1. When a local maximum is observed between the downward or upward zero-crossing points and the minimum NEE. In such cases, adding the Gaussian curve shifts these peaks above the zero-crossing line, creating an additional downward or upward zero-crossing point. This complicates the assessment of CUP_{NEE} following the manipulation, and results in ΔCUP_{NEE} being different from the prescribed value. The Δ is kept at zero in this case.

2. In a few instances, when the magnitude of Δ is larger than the period between the original zero-crossing dates and the start/end of the period of manipulation, we instead opt for the next-closest Δ value in the sequence.

3. Additionally, in manipulation cases where interannually varying fluxes are used (Δ_x^l), only certain years have the complexities described above. In such instances, the next available Δ value from the sequence is chosen to minimally impact the imposed CUP_{NEE} trend. This involves selecting a Δ such that it results in a smaller or larger value compared to the subsequent year, achieving either a positive or negative change in CUP_{NEE} (i.e., Δ_p^l or $\Delta_n^l CUP_{NEE}$).

The manipulated pixels for the different cases are shown in Fig. 3.3. Furthermore, the manipulated fluxes are used to conduct regional sensitivity analyses, in which we limit the flux manipulation process explained above to different TransCom3 (Gurney et al., 2002) geographic regions in the Northern Hemisphere. This allows us to evaluate the regional contribution of NEE fluxes to ΔCUP_{MR} when comparing how perturbations involving different regions are expressed in $\Delta_x^l CUP_{MR}$ at the studied sites. This comparison is conducted for two experiments: ERV_0^0, illustrating the integration of signals from various regions in an idealized scenario without IAV in atmospheric transport or CUP_{NEE}; and ERV_1^T, which reflects signal integration in a relatively realistic setting, with IAV in atmospheric transport and CUP_{NEE}.

3.3.2 Forward transport runs

We use a three-dimensional global atmospheric transport model, TM3 (Heimann & Körner, 2003), to simulate CO_2 mixing ratios at the specified sites based on manipulated NEE fluxes. The model is run at a spatial resolution of 5° in longitude and 4° in latitude with 19 vertical levels, using 6-hourly NCEP reanalysis meteorological fields from 1995 to 2017 and daily surface fluxes from the Jena Carboscope CO_2 Inversion (version ID: sEXTocNEET_v2021) (Rödenbeck et al., 2003), with the NEE fluxes manipulated as previously described. The forward runs are carried out with (1) fixed transport (mete-

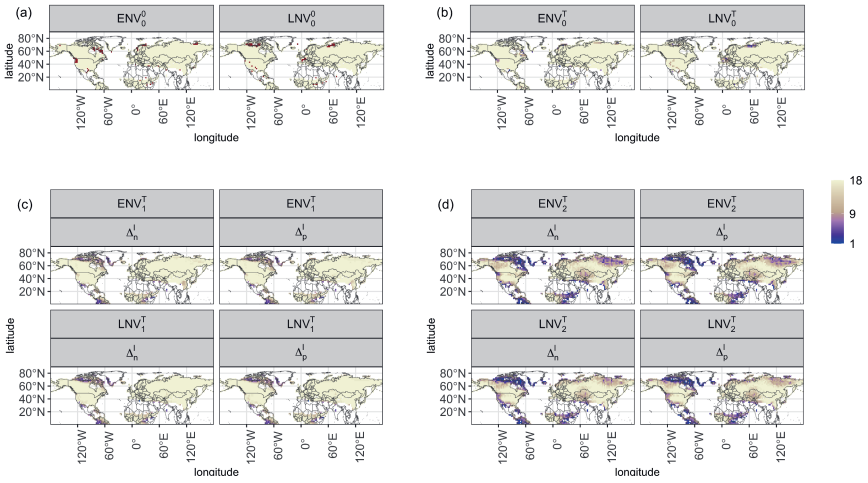


Figure 3.3: Spatial distribution of the pixels manipulated for different experiments. (a) Reference year flux is repeated and discrete changes are prescribed to CUP_{NEE} (beige), the red color represents pixels where Δ is different from the prescribed Δ due to the complications described in Sect. 3.3.1. (b) Reference year flux is repeated and a long-term trend is applied to CUP_{NEE}. When a long-term trend is applied, Δ varies over the years. The colour bar indicates the number of years for which Δ equals the prescribed Δ, i.e., years with no complications described in Sect. 3.3.1 (also applicable for panels (c) and (d)). (c) Actual CUP_{NEE} is retained and long-term trend is applied to CUP_{NEE}. (d) IAV in CUP_{NEE} is doubled and a long-term trend is applied. The panel titles in every plot represent different simulations as detailed in Table 3.1.

orology from a random year, here we used the year 2008 and repeated it in time such that there is no IAV) and (2) interannually varying transport for the period 1995 to 2017 to study the contribution of atmospheric transport to the IAV in CUP_{MR}. The first five years are excluded from the CUP_{MR} analysis to account for the model's spin-up time, and ΔCUP_{NEE} is held at zero during this period.

3.3.3 CUP estimation methods

The forward transport runs simulate CO_2 mixing ratios at discrete time steps, which we sample at the frequency corresponding to the flask measurements (approximately bi-weekly) at the studied sites. This sampling interval sufficiently captures the larger-scale trends and seasonal variations critical to our analysis and allows for consistent comparison with previous studies that looked into long-term trends using flask measurements. We apply the EFD method described in Kariyathan et al. (2023) to the output data and estimate the CUP_{MR}. Here, the CUP_{MR} is estimated using a threshold derived from the first derivative of the detrended and smoothed CO_2 mixing ratio seasonal cycle curves. A threshold of 15% and 0% of the first-derivative minimum was used as a threshold to determine the onset and termination of the CUP_{MR}, respectively, as in Kariyathan et al. (2023). The calculation is applied to an ensemble of the detrended time series, which allows for an uncertainty range on the CUP estimate to be calculated.

3.4 Results

3.4.1 Northern Hemisphere CUP_{MR} sensitivity under fixed transport

The calculated ΔCUP_{MR} consistently shows lower absolute values than the prescribed ΔCUP_{NEE}. For example, at BRW, ΔCUP_{MR} is 0.43 times the prescribed early phase ΔCUP_{NEE} as illustrated in Fig. 3.4, (a). This reduction in ΔCUP_{MR} is found across all the studied sites with varying degrees of intensity as illustrated in Fig. 3.4, (d), when Δ is prescribed to either the early or late phases of CUP_{NEE}. This shows how atmospheric observations respond differently to CUP perturbations compared to local NEE measurements, and a one-on-one translation might lead to an incorrect interpretation of at least the magnitude of CUP changes. The persistent difference in the magnitude of ΔCUP_{MR} from the imposed ΔCUP_{NEE} results from the integration of signals from various regions with different CUP_{NEE} timings as detailed in Sect. 3.5.

At most studied sites, the Δ assigned to the early phase of CUP_{NEE} predominantly affects the onset of CUP_{MR} (Fig 3.4, (b) and (e)). The ΔCUP_{MR} then corresponds to the changes in onset of CUP_{MR} as indicated by the similar variation in the red bars in Fig. 3.4 (d) and (e). Similarly, Δ applied to the late phase of CUP_{NEE} primarily influences the termination of CUP_{MR} (Fig. 3.4, (c) and (f)) which then drives ΔCUP_{MR}

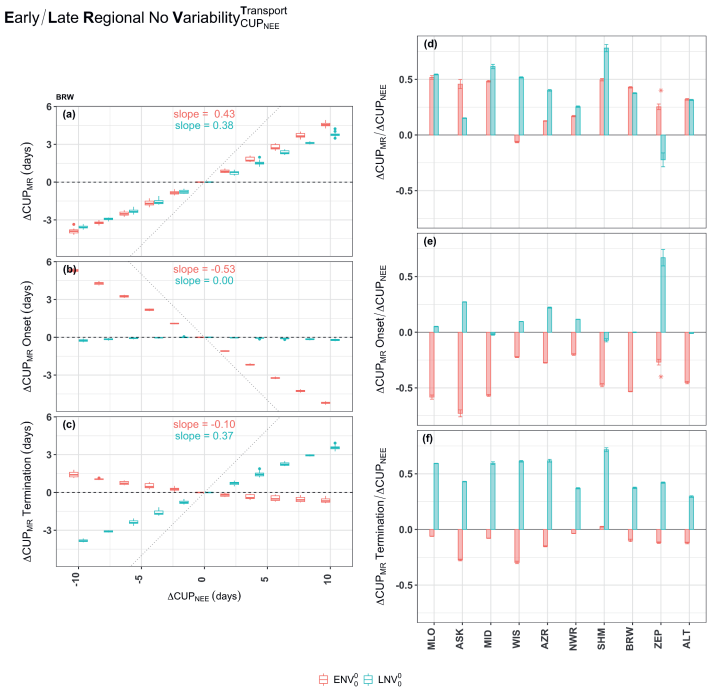


Figure 3.4: The change in $\mathrm{CUP_{MR}}$ in response to varying $\Delta\mathrm{CUP_{NEE}}$ for experiments ENV_0^0 (red) and LNV_0^0 (cyan). The experiments ENV_0^0 and LNV_0^0 largely drives the Δ in $\mathrm{CUP_{MR}}$ onset and termination respectively and thereby $\Delta\mathrm{CUP_{MR}}$. The left panels show the Δ in (a) $\mathrm{CUP_{MR}}$ (ie., the duration), (b) $\mathrm{CUP_{MR}}$ onset and (c) $\mathrm{CUP_{MR}}$ termination against the applied $\Delta\mathrm{CUP_{NEE}}$ for BRW. In these panels, the individual boxplots display the distribution of the median values across years, estimated from the ensemble spread for each year. The dotted line represents an ideal case of a one-to-one (minus one-to-one for panel (b)) relation between $\Delta\mathrm{CUP_{NEE}}$ and $\Delta\mathrm{CUP_{MR}}$. The text within these plots shows the slope of the regression lines fitted to the median of the boxplots. The right panels ((d) to (f)) show these slopes (unit less) across the different studied sites. The estimate of ZEP is reduced to 0.1 times the actual value for ease of visualization. Error bars represent $\pm$ one standard deviation (σ) around the estimated slope.

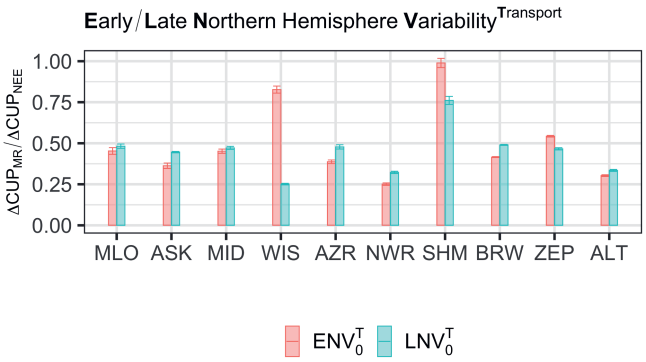


Figure 3.5: The change in CUP_{MR} metrics in response to varying ΔCUP_{NEE}, similar to Fig. 3.4, (d) but for the experiments with interannually varying meteorology, ENV_0^T (red) and LNV_0^T (cyan).

in experiment LNV_0^0 (Fig. 3.4, (d) and (f), cyan bars). This suggests that the changes in the early and late phases of CUP at the surface can be analysed separately by examining the onset and termination of CUP inferred from CO_2 mole fraction observations. Contrary to the direct but dampened relationship between ΔCUP_{NEE} and ΔCUP_{MR}, we find an opposite response at some sites: a lengthening (shortening) imposed on CUP_{NEE} leads to shortening (lengthening) of the CUP_{MR}. This is seen to occur at sites ZEP and WIS, as indicated by the negative slopes at these sites (Fig. 3.4, (d)).

At ZEP, the late phase ΔCUP_{NEE} leads to unintended changes in CUP_{MR} onset. For Δ prescribed to the late CUP_{NEE} phase, the change in CUP_{MR} termination is only 0.4 times the Δ, while that in the onset is 0.6 times the Δ. Thus, the changes intended for CUP_{MR} termination extend to CUP_{MR} onset in the following year. For example, a 10-day delay prescribed to the CUP_{NEE} termination results in a 4-day delay in CUP_{MR} termination and a 6-day delay in the onset. This results in a 2-day shorter CUP_{MR}, establishing an inverse relation between ΔCUP_{MR} and ΔCUP_{NEE} at ZEP (slope of -0.22 in the experiment LNV_0^0). Likewise, at WIS, in experiment ENV_0^0, the change in CUP_{MR} onset is only -0.2 times the applied early phase ΔCUP_{NEE}, while the change in termination is -0.3 times the perturbation imposed. This offsets the ΔCUP_{MR} and leads to a significant ($p < 0.001$) inverse relation between ΔCUP_{MR} and ΔCUP_{NEE} at WIS (slope of -0.06, in the ENV_0^0 experiment).

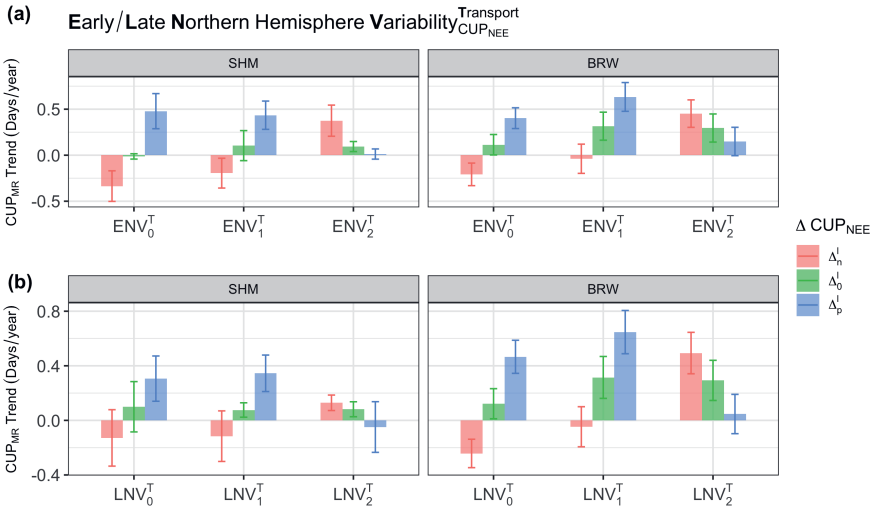


Figure 3.6: Sensitivity of $\mathrm{CUP_{MR}}$ to the applied long-term trend in $\mathrm{CUP_{NEE}}$ (results for sites SHM and BRW). The bars show the slope of the regression line fitted to the median $\mathrm{CUP_{MR}}$ from experiments ENV_x^T (a) and LNV_x^T (b), where x is 0, 1, and 2 implying no IAV in NEE flux, the actual IAV in NEE flux, and two times the actual IAV in NEE flux respectively. Error bars represent ± one standard deviation (σ) around the estimated slope. Colours show the prescribed trend Δ_p^l (1.1 days/year) in blue, Δ_n^l (-1.1 days/year) in red and Δ_0^l (0 days/year) in green applied to $\mathrm{CUP_{NEE}}$.

3.4.2 Northern Hemisphere $\mathrm{CUP_{MR}}$ sensitivity under interannually varying transport

Even when interannual variations from atmospheric transport are included, changes imposed in $\Delta\mathrm{CUP_{NEE}}$ are reflected in $\Delta\mathrm{CUP_{MR}}$. The varying atmospheric transport leads to year-to-year variations in signal integration and changes that were not captured in the experiment with transport from single-year meteorology can be seen in the experiment with inter-annually varying transport. This is illustrated for different sites in Fig. 3.5. An inverse relation between $\Delta\mathrm{CUP_{MR}}$ and $\Delta\mathrm{CUP_{NEE}}$ was calculated at WIS and ZEP in experiments ENV_0^0 and LNV_0^0, respectively, as described in Sect. 3.4.1. However, in experiments with varying transport, slope values of 0.83 at WIS (experiment ENV_0^T) and 0.47 at ZEP (experiment LNV_0^T) are found, compared to -0.06 and -0.22 in the experiment with fixed transport. This suggests that anomalies observed in specific years may be predominantly attributed to the meteorological conditions of those particular years.

3.4.3 Northern Hemisphere CUP_{MR} sensitivity to long-term trends in CUP_{NEE}

Out of all the evaluated sites, only SHM and BRW partially captured CUP_{MR} trends corresponding to the imposed trends in CUP_{NEE} as shown in Fig. 3.6 (results for other sites are shown in Table A.1). In experiment ENV_0^T, the largest trend in CUP_{MR} is derived at SHM, with values of 0.5 days/year and -0.3 days/year for the imposed increasing (1.11 days/year) and decreasing (-1.11 days/year) trend respectively. Similarly, in experiment LNV_0^T, the largest trend in CUP_{MR} is observed at BRW (0.5 days/year and -0.2 days/year for the imposed increasing and decreasing trend respectively). Nevertheless, part of the observed trend can be attributed to the IAV in atmospheric transport thereby showing that the IAV in transport can influence our understanding of the actual long-term changes in CUP_{NEE} trends. This can be seen in Fig. 3.6, green bars (Δ_0^l), corresponding to experiments ENV_0^T and LNV_0^T. Note that in these experiments, there is no IAV in the CUP_{NEE} flux as indicated by the subscript '0', and Δ_0^l, indicates that no trend is prescribed to the CUP_{NEE}. Then any derived CUP_{MR} trend can be attributed solely to the IAV in transport. The trend from the IAV in transport contributes to the asymmetry between the red and blue bars. At BRW, experiment LNV_0^T, indicates that a CUP_{MR} trend of 0.1 days/year can arise from variability in transport alone, and accounts for about 20% of the derived CUP_{MR} trend (blue bar showing 0.5 days/year).

Furthermore, we observe that the actual IAV in the CUP_{NEE} fluxes contribute to the derived CUP_{MR} trends; however, as the IAV in the flux becomes larger, it imposes noise that makes the trends harder to detect. This is shown in experiments ENV_1^T and ENV_2^T (Fig. 3.6), where the actual IAV in CUP_{NEE} is retained and doubled, respectively. In experiment ENV_1^T, the CUP_{MR} trend in response to the prescribed opposite trends, Δ_p^l and Δ_n^l are distinct in sign. Even though the magnitude of the prescribed trend is the same, a large difference in magnitude can be seen between results for Δ_p^l (red bar, 0.6 days/year) and Δ_p^l (blue bar, -0.03 days/year), for example, at BRW. This can be attributed to the increasing trend from both IAV in the actual flux and transport, as indicated by the green bar for ENV_1^T. The green bars in experiment ENV_1^T (0.3 days/year) and ENV_0^T (0.1 days/year) are distinct, and their difference (0.2 days/year) is the contribution from the actual IAV in CUP_{NEE} alone. In the experiment where the IAV in CUP_{NEE} per pixel was doubled, it becomes evident that the imposed alterations in CUP_{NEE} are not accurately reflected in CUP_{MR}, even at sites like BRW, which exhibited pronounced responses in other experiments (ENV_1^T and LNV_1^T).

3.4.4 Regional contribution to CUP_{MR}

The various Transcom3 regions of the Northern Hemisphere contribute in various degrees to the CUP_{MR} changes observed at the studied sites. The changes in the Boreal regions are partially captured at both the higher and lower latitudes (e.g., ALT, BRW, SHM,

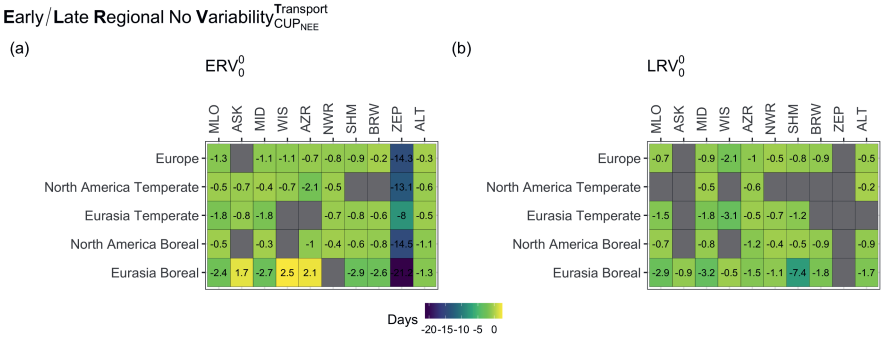


Figure 3.7: Regional contribution to ΔCUP_{MR}. The colour and value represent the ensemble median of ΔCUP_{MR} when ΔCUP_{NEE} is -10 days, in experiment ERV_0^0 (a) and LRV_0^0 (b). Values are displayed solely for the sites where a significant difference in ΔCUP_{MR} is detected when ΔCUP_{NEE} is 0 and -10 days (p-value of Mann-Whitney test < 0.05) in the specific region (y-axis).

MID, and MLO). Considering both early and late ΔCUP_{NEE} phases, the contribution from the Eurasian Boreal region is largely seen at SHM (-3 days in early and -7 days in the late CUP_{NEE} phase), followed by MID with (-3 in both the days early and late CUP_{NEE} phase), showing an eastward transport from the Eurasian Boreal region. Similarly, considering both the CUP_{NEE} phases, the contribution from the North American Boreal region is seen at all sites except ASK, WIS, and ZEP. In response to delayed onset, prescribed to the CUP_{NEE} in Eurasian Boreal region, a longer CUP_{MR} is calculated at ASK, WIS, and AZR (Fig. 3.7 (a)), suggesting that the inverse slope relation between ΔCUP_{MR} and ΔCUP_{NEE} in Sect. 3.4.1 might largely be from changes in the Eurasian Boreal region. In the Eurasian Temperate region, the Δ prescribed to both the early and late CUP_{NEE} phase integrates at the lower latitude site (e.g., MID, MLO, NWR, and, SHM), whereas higher latitude sites (e.g., ALT, BRW and ZEP) only capture perturbations imposed during the early phase of CUP_{NEE}. The contribution from the North American Temperate region is strong during the early phase of CUP_{NEE}, while late phase changes are captured only by MID and AZR. Signals from the European region integrate well at most of the studied sites. At ZEP, a significant regional contribution from any of the studied TransCom3 regions can only be seen in the early CUP_{NEE} phase. This explains to some extent the direct relation between ΔCUP_{MR} and ΔCUP_{NEE} found only in the early phase (Sect. 3.4.1).

The long-term trend in the CUP_{MR} could not be accurately attributed to different regions even for sites like BRW that showed a predominant response to the prescribed long-term trend in CUP_{NEE} (Sect. 3.4.3). This can be seen from (Fig. 3.8). At BRW,

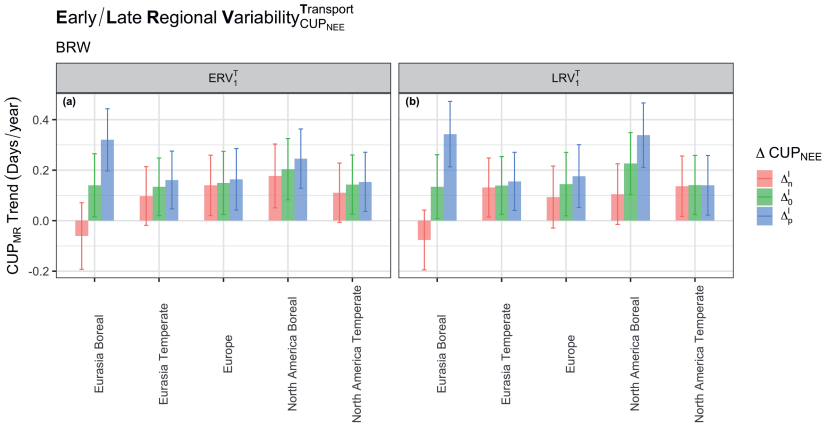


Figure 3.8: Regional contribution to CUP_{MR} trend detected at BRW in response to imposed long-term CUP_{NEE} trends. The bars show the slope of the regression line fitted to median CUP_{MR} from experiments ERV_1^T (a) and LRV_1^T (b). Error bars represent ± 1 standard deviation (σ) around the estimated slope. The colours represent the trend in NEE imposed in the experiment, as described in Fig. 6.

the CUP_{MR} trends partially reflect the CUP_{NEE} trends prescribed to the Eurasian Boreal region. For example, in the early CUP_{NEE} phase, we find a change of 0.32 days/year and -0.06 days/year in response to the prescribed Δ_p^l (1.1days/year) and Δ_n^l (-1.1days/year), respectively. However, the large error bars show that the uncertainty in trend estimation is large when changes are prescribed to only a given TransCom3 region.

3.5 Discussion

We find that changes (both fixed differences and trends) prescribed to CUP_{NEE} are reflected in CUP_{MR} simulated by TM3. However, the magnitude of the change seen in CUP_{MR} is consistently lower than the prescribed change in CUP_{NEE}, for example at BRW only about 50% of the change applied to CUP_{NEE} was reflected in ΔCUP_{MR}, even in simulations with fixed transport. This is contradictory to previous studies that consider the long-term CO_2 record to reflect changes in surface fluxes. For example, in Piao et al. (2008), 50% of the observed zero-crossing date variance at BRW could be accounted for by NEE variability.

We show that, given fixed transport, the reduced expression of changes in CUP_{MR} relative to CUP_{NEE} arises from variations in the timing of CUP_{NEE} across the regions

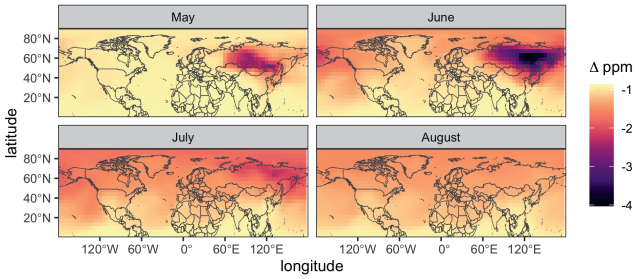


Figure 3.9: 2D mixing ratio fields (integrated vertically up to an altitude of 400 m and averaged per month) when a delay of 10 days is prescribed to the $\mathrm{CUP_{NEE}}$ onset in the Eurasian Boreal region. The field (Δ ppm) is the difference between the 2D mixing ratio fields when $\Delta\mathrm{CUP_{NEE}}$ is -10 days and 0 days in experiment ERV_0^0.

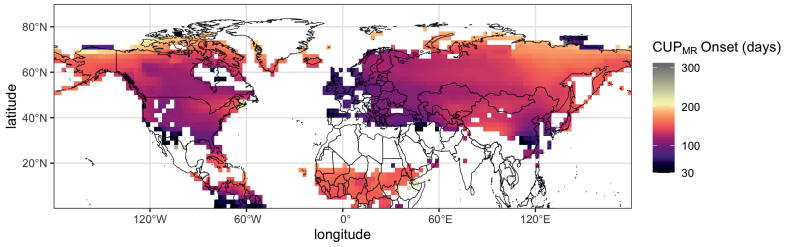


Figure 3.10: Spatial distribution of the $\mathrm{CUP_{NEE}}$ timing across the Northern Hemisphere as derived from Jena CarboScope CO_2 Inversion (version ID: sEXTocNEET_v2021) NEE fluxes for the reference year (2003) used in the study.

over which the signal is integrated. For instance, when a delay (10 days) was applied to the CUP_{NEE} onset in the Eurasian Boreal region, the mixing ratio reflects this change over the region in May and the signal slowly propagates eastward by June (Fig. 3.9), showing a difference in timing of the onset within the Eurasian Boreal region. The difference in the spatial distribution of CUP_{NEE} onset, with an earlier CUP_{NEE} onset in the western and later in the eastern part of the Eurasian Boreal region, is shown in Fig. 3.10. Due to the difference in CUP_{NEE} timing across the pixels, the effective ΔCUP_{NEE} of a region will be different from the applied Δ. The atmospheric transport does not always carry the CUP_{NEE} fluxes from the region to the observation site; it could be transported in other directions at other times. If an applied Δ shifts the CUP_{NEE} timing of some pixels into a period when transport is less favourable, the contribution from those pixels may be weaker or absent in the final measurements, causing a dampened relation between ΔCUP_{NEE} and ΔCUP_{MR}. Below, we discuss how the sensitivity of CUP_{NEE} to the discrete and long-term changes in surface fluxes is affected when influenced by the interannual variability in both transport and surface fluxes.

3.5.1 Transport influence on CUP_{MR}

We have shown the significant role of interannually varying atmospheric transport in the evaluation of metrics derived from CO_2 mole fraction data. At certain sites such as ZEP and WIS, the CUP_{MR} from simulations with fixed transport failed to capture the CUP_{NEE} changes, whereas in simulations with varying transport, the prescribed CUP_{NEE} changes could be partially derived from CUP_{MR}. This indicates that in a given year of meteorology used in the fixed transport simulation, the atmospheric transport is unlikely to originate from the areas where the ΔCUP_{NEE} was prescribed, while in simulations with transport variability, the meteorology in other years might have originated from these regions. Thus, the anomalies observed in CUP_{MR} in a particular year could stem from transport variability rather than anomalies in CUP_{NEE} itself, rendering mixing ratio time-series less useful for studying interannual variations in CUP_{NEE}.

Finally, we show that due to the atmospheric transport, the source areas for a given station during the early and late CUP_{NEE} phases can be substantially different, influencing the expression of CUP_{MR} in the different CUP_{NEE} phases. For instance, our analysis (Fig. 3.7) shows that WIS mainly receives signals from the Northern Hemisphere land pixels only in the late CUP_{NEE} phase. Consequently, at WIS, the CUP_{MR} is directly proportional solely to changes prescribed to late CUP_{NEE} phase (slope of 0.5 in LNV_0^0). Similarly, at ZEP, the contribution of the Northern Hemisphere landmass to ΔCUP_{MR} occurs only in the early CUP_{NEE} phase. The atmospheric transport to ZEP is dominated by the regions Eurasian Boreal and Europe during March-May; in the following months (June-August), the air mass transport is largely confined to the Arctic and does not extend equatorward into the continents in some years (Tunved et al., 2013; Platt et al.,

2022). Our observations imply that at ZEP/WIS, changes in the onset/termination of CUP_{NEE} are more effectively reflected as changes in CUP_{MR}.

3.5.2 Long-term trends in CUP_{MR}

The long-term trends prescribed to the CUP_{NEE} could be partially derived from CUP_{MR} at BRW and SHM, even under IAV in atmospheric transport and CUP_{NEE}. However, when IAV in CUP_{NEE} was doubled, the prescribed trends were not captured. This suggests that the long-term trends in the observations may be compromised when there is a higher IAV in CUP_{NEE}. The contribution from atmospheric transport exhibited a CUP_{MR} trend of 0.11 days/year at BRW. This finding aligns with a study by Murayama et al. (2007) where the IAV in transport alone caused a change of 0.16 days per year in the downward zero-crossing date at BRW for their analysis period between 1979 and 1999.

With warming, a longer growing season is observed in the high latitudes (e.g., Park et al. (2016), 2.6 days per decade). A longer growing season does not necessarily mean an increase in CUP_{NEE} or CUP_{MR} as they are determined by both photosynthesis and respiration. The existing literature on the CUP_{NEE} changes in the Northern Hemisphere based on CUP_{MR} varies from increasing (Keeling et al., 1996) to neutral (Barichivich et al., 2012) to decreasing (Piao et al., 2008). The complications in interpreting CUP_{NEE} changes arise mostly when directly assessing the CUP from CO_2 mixing ratio. Therefore, CO_2 observations should preferably be interpreted following a formal inverse estimate of the corresponding surface NEE. It is then possible to account for the interannual variability, trends, and delays imposed by the slow atmospheric mixing. Nevertheless, the ability of such inversions to constrain regional changes in NEE can only be improved with an expanded observation network.

3.5.3 Regional contribution to CUP_{MR}

The regions contributing to the integrated signal at various observation sites are influenced by atmospheric transport to these locations. From the idealized simulations with no IAV in transport or CUP_{NEE} it turned out that at sites like ALT, BRW, SHM, and MLO, a significant contribution from Boreal and Temperate regions could be calculated, indicating that these remote sites receive well-mixed signals from higher- and mid-latitude regions in the Northern Hemisphere with strong seasonality. We calculate that the contribution from mid-latitude is significant at the sites in the Boreal region (e.g., ALT and BRW in early CUP_{NEE} phase) in line with Barnes et al. (2016). They found that the seasonal cycle observed at higher latitude sites is most sensitive to changes in the seasonality of mid-latitude surface emissions; however, we do not find that the mid-latitude influence is more than the Boreal region influences at higher-latitude sites. At ZEP, strong signals from both Eurasian and North American regions dominate during the early CUP_{NEE} phase (Fig. 3.7), and an amplification of the CUP_{MR} signal is

found. Further, a significant change in the regional contribution is found between the early and late CUP_{NEE} phases, shifting from continental in the early CUP_{NEE} phase to ocean signals in parts of the late CUP_{NEE} phase (Sect. 3.5.1). This change explains the significant difference in ΔCUP_{MR} to ΔCUP_{NEE} during different phases, as shown in Fig. 3.4. At WIS, ASK, and AZR, when a delayed onset is imposed on the CUP_{NEE} from Eurasian Boreal regions, a positive ΔCUP_{MR} (i.e., an extension in CUP_{MR}) is calculated. These sites are located in the temperate regions. The CO_2 2D mixing ratio fields (Fig. 3.9) reveal that changes imposed on the Boreal region propagate partially to the lower latitudes (around 30°N) later in the CUP_{NEE} phase. Thereby the delay imposed on the CUP_{NEE} of the Eurasian Boreal region in May integrates at the lower latitude region (near to the location of WIS, ASK, and AZR) only later in July, delaying and extending the CUP_{MR}.

When the long-term trends were applied to specific regions, the slope estimated from CUP_{MR} had large uncertainty due to the influence of IAV in transport and CUP_{NEE}. Furthermore, the flux manipulation strictly within the boundaries of the TransCom3 region in our experiments may have substantially limited the regions from which the signals reach the sites. In the real world, regional boundaries are more diffuse, and the footprint of the site provides a more accurate estimate of the regions contributing to the observed signals. Nonetheless, this aspect falls outside the scope of the present study.

The changes in the CO_2 mixing ratio time series from the Northern Hemisphere give a larger spatial perspective of the CUP_{NEE} changes. However, results from idealized simulations suggest that they are influenced by atmospheric transport IAV, seasonal changes in atmospheric transport, and IAV in the biospheric fluxes. We find a significant damping of the changes that were imposed on the CUP_{NEE}, from the integration of signals from different regions that have varied timing and suggest a more intense change in the local spatial scales. With the constraints in NEE flux manipulation, imposed by the presence of local maxima and insufficient data points for Δ changes in the early and late CUP_{NEE} (Sect. 3.3.1), the simulations in this study do not accurately represent the real-world scenarios. In the real world, the changes in CUP_{NEE} are asynchronous across space. Although we broadly examined the influence of different TransCom3 regions, conducting more dedicated footprint analyses of the studied sites may offer further insights into the signals studied here.

3.6 Conclusions

Our analysis, based on forward model experiments, reveals that at well-studied sites such as MLO, BRW, and ALT, only circa 50% of the prescribed changes in the CUP_{NEE} fluxes

were reflected in CUP_{MR}. In simulations with interannually varying meteorology, the signals were better captured at a few sites like ZEP and WIS, showing the significant influence of IAV in atmospheric transport. At BRW, 20% of the observed trend could be attributed to the IAV in transport. Furthermore, our findings suggest that the changes estimated in CUP_{MR}, subsequent to the separation of atmospheric transport influence, are likely to underestimate the actual magnitude of signals from the surface changes. This is because of the damping due to the integration of asynchronous CUP_{NEE} timing across different regions. While sites like BRW and SHM partially captured the prescribed long-term changes in the presence of natural IAV, they proved insensitive when IAV in CUP_{NEE} was doubled due to insufficient signal to noise. Furthermore, trends prescribed to individual TransCom3 regions were not captured by the evaluated sites, showing that long-term changes in the seasonal cycle of time series primarily reflect changes on larger spatial scales. These findings are based on forward model experiments rather than direct atmospheric observations, and they do not provide a direct estimate of biospheric changes. Instead, they highlight how atmospheric transport processes influence the representation of surface flux changes in CO_2 observations.

Appendix

Table A.1: Sensitivity of CUP_{MR} to the applied long-term trend in CUP_{NEE} for the different sites (excluding SHM and BRW). The first column shows the sites, the second column describes the prescribed trend Δ_x^l applied to CUP_{NEE}, and the other columns describe the different experiments, as detailed in the caption of Fig. 3.6. The values show the slope of the regression line fitted to the median CUP_{MR} ± one standard deviation (σ) around the estimated slope (in units of days/year) for the experiments indicated by the column names.

Site	Δ_x^l	ENV_0^T	ENV_1^T	ENV_2^T	LNV_0^T	LNV_1^T	LNV_2^T
MLO	Δ_p^l	0.07 ± 0.04	0.10 ± 0.05	0.00 ± 0.03	0.03 ± 0.04	0.06 ± 0.05	-0.05 ± 0.05
MLO	Δ_0^l	0.00 ± 0.03	0.02 ± 0.03	0.02 ± 0.03	0.00 ± 0.03	0.02 ± 0.03	0.00 ± 0.05
MLO	Δ_n^l	-0.14 ± 0.03	-0.08 ± 0.05	0.07 ± 0.05	-0.11 ± 0.04	-0.05 ± 0.05	0.05 ± 0.05
ASK	Δ_p^l	0.07 ± 0.07	0.31 ± 0.11	0.01 ± 0.07	0.13 ± 0.08	0.10 ± 0.08	0.06 ± 0.11
ASK	Δ_0^l	0.02 ± 0.05	0.05 ± 0.08	0.06 ± 0.08	0.02 ± 0.05	0.05 ± 0.08	0.05 ± 0.09
ASK	Δ_n^l	-0.08 ± 0.06	0.00 ± 0.07	0.26 ± 0.11	-0.11 ± 0.09	0.33 ± 0.28	0.09 ± 0.09
MID	Δ_p^l	0.05 ± 0.04	0.09 ± 0.04	0.03 ± 0.03	0.05 ± 0.05	0.06 ± 0.04	0.03 ± 0.03
MID	Δ_0^l	0.04 ± 0.04	0.03 ± 0.03	0.03 ± 0.03	0.03 ± 0.04	0.03 ± 0.03	0.03 ± 0.03
MID	Δ_n^l	0.02 ± 0.04	0.02 ± 0.03	0.04 ± 0.03	0.03 ± 0.04	0.05 ± 0.04	0.03 ± 0.03
WIS	Δ_p^l	0.08 ± 0.13	0.17 ± 0.13	-0.12 ± 0.11	-0.35 ± 0.15	-0.06 ± 0.13	0.00 ± 0.12
WIS	Δ_0^l	-0.25 ± 0.14	-0.02 ± 0.12	-0.01 ± 0.12	-0.23 ± 0.13	-0.02 ± 0.12	-0.02 ± 0.13
WIS	Δ_n^l	-1.02 ± 0.2	-0.19 ± 0.12	0.09 ± 0.12	-0.12 ± 0.13	0.03 ± 0.16	-0.03 ± 0.13
AZR	Δ_p^l	0.01 ± 0.03	0.01 ± 0.05	-0.01 ± 0.03	0.00 ± 0.02	0.00 ± 0.05	-0.01 ± 0.05
AZR	Δ_0^l	0.01 ± 0.03	-0.01 ± 0.03	-0.01 ± 0.03	0.00 ± 0.02	0.00 ± 0.03	0.00 ± 0.03
AZR	Δ_n^l	0.01 ± 0.02	0.00 ± 0.03	0.00 ± 0.03	-0.02 ± 0.04	0.00 ± 0.07	-0.01 ± 0.03
NWR	Δ_p^l	0.03 ± 0.06	0.44 ± 0.29	0.03 ± 0.13	0.02 ± 0.06	0.05 ± 0.23	0.24 ± 0.22
NWR	Δ_0^l	0.01 ± 0.06	0.05 ± 0.17	0.04 ± 0.14	0.01 ± 0.06	0.16 ± 0.21	0.04 ± 0.16
NWR	Δ_n^l	0.01 ± 0.06	0.03 ± 0.14	0.06 ± 0.16	0.01 ± 0.06	0.26 ± 0.23	0.07 ± 0.24
ZEP	Δ_p^l	0.18 ± 0.04	0.35 ± 0.06	0.05 ± 0.04	0.11 ± 0.04	0.22 ± 0.06	0.15 ± 0.06
ZEP	Δ_0^l	0.02 ± 0.03	0.09 ± 0.04	0.08 ± 0.04	0.02 ± 0.03	0.08 ± 0.04	0.08 ± 0.04
ZEP	Δ_n^l	-0.04 ± 0.03	0.02 ± 0.05	0.12 ± 0.04	0.00 ± 0.04	0.51 ± 0.15	0.09 ± 0.04
ALT	Δ_p^l	0.05 ± 0.03	0.19 ± 0.06	0.00 ± 0.03	0.10 ± 0.05	0.18 ± 0.06	0.02 ± 0.06
ALT	Δ_0^l	0.00 ± 0.03	0.05 ± 0.04	0.05 ± 0.04	-0.01 ± 0.03	0.05 ± 0.04	0.05 ± 0.04
ALT	Δ_n^l	-0.05 ± 0.03	-0.02 ± 0.06	0.07 ± 0.04	-0.07 ± 0.04	-0.01 ± 0.06	0.13 ± 0.06

Chapter 4

Advancing onset of the carbon uptake period revealed by high-latitude CO_2 records, linked to Eurasian regions

This chapter is based on:

Kariyathan, T., Marshall, J., Bastos, A., Reichstein, M., & Peters, W. Advancing onset of the carbon uptake period: revealed by high-latitude CO_2 records, linked to Eurasian regions. (In prep.)

Abstract

The extent and timing of the carbon uptake period (CUP) — the period of the year during which photosynthetic CO_2 uptake exceeds respiratory release — provides a sensitive indicator of ecosystem responses to climate change. Recent studies suggest spatial and temporal heterogeneity in biospheric responses to warming, raising questions about the ongoing trends in CUP timing. In this study, we examine CUP changes in the past two decades (2001-2021) using multi-decadal atmospheric CO_2 dry-air mole fraction measurements from the NOAA/GML CCGG cooperative air sampling network, combined with net ecosystem exchange (NEE) flux estimates from top-down atmospheric inversions (Jena CarboScope and CarbonTracker Europe) and a bottom-up data-driven product (FLUXCOM-X-Base). We address three central questions: (1) How has the CUP timing evolved in recent decades? (2) How does CUP timing differ across regions? (3) How do key drivers such as gross primary productivity (GPP), terrestrial ecosystem respiration (TER) and temperature contribute to the trends in CUP timing? Our analysis of atmospheric records reveals a robust and spatially coherent advancement in CUP onset across northern high latitudes. This advancing signal is also reproduced in CO_2 mole fractions simulated from independent flux products (Jena CarboScope, CarbonTracker, and FLUXCOM-X-Base). Across the diverse datasets (observed and simulated CO_2 mole fractions), the mean trend corresponds to an advancement of -2.50 $\pm$ 0.27 days per decade in CUP onset (95% CI: -3.04 to -1.96 days decade^{-1}). Regional analyses show that this signal originates primarily from Eurasian boreal ecosystems, where CUP onset derived from NEE exhibits a significant advancing trend, while North American regions display weaker, inconsistent, or non-significant changes. Decomposition of NEE into its component fluxes reveals that the advancing CUP onset is dominated by earlier GPP activation. The regional contrast in CUP onset trends is mirrored in the onset of both GPP and TER, particularly between Eurasian boreal and North American temperate regions. This regional difference is further consistent with spatial differences in spring temperature trends, with stronger and more coherent warming in Eurasia relative to North America. Together, these results demonstrate that recent spring warming in the Eurasian boreal region has led to earlier photosynthetic activity, driving a net advance in the onset of CUP that is imprinted in high-latitude atmospheric CO_2 records.

4.1 Introduction

The terrestrial carbon cycle plays a crucial role in regulating atmospheric CO_2 levels, with carbon uptake and release driven by plant photosynthesis and ecosystem respiration (Ciais et al., 2019). The period of the year when ecosystems absorb more CO_2 through photosynthesis than they release via respiration is known as the carbon uptake period (CUP). This period is shaped by the interplay between photosynthesis and respiration, which is strongly influenced by changes in environmental conditions. For example, warmer and earlier springs enhance early-season gross primary productivity (GPP) more than terrestrial ecosystem respiration (TER), leading to an earlier transition of net ecosystem exchange (NEE) to a carbon sink (Baldocchi et al., 2018). The CUP differs from the growing season, which represents periods of potential photosynthetic activity; instead, it explicitly reflects the balance between photosynthetic uptake and ecosystem respiration, and hence the two periods need not align in time.

Between 1982 and the early 2000s, the growing season in the northern high latitudes lengthened, largely due to rising spring temperatures (Park et al., 2016; Piao et al., 2007). Regional differences in ecosystem response were observed during this period, with browning in parts of North America and greening in Europe (Bi et al., 2013). Over a similar timeframe, Barichivich et al. (2012) showed an earlier onset of the CUP and further highlighted regional differences, noting a stronger advancement of the CUP onset in Eurasia compared to North America, which was attributed to more rapidly changing temperatures. In the period after 2000, often described as a warming hiatus (Modak & Mauritsen, 2021; Flato et al., 2013), satellite-based analyses show slower phenological changes, with no consistent advance in spring or delay in autumn, indicating a weakening of the earlier trend towards a longer growing season (Wang et al., 2019).

Recent findings further suggest that the once-strong relationship between rising spring temperatures and an earlier onset of the growing season is weakening across many areas. For example, Xiong et al. (2024) observed that although spring temperatures continued to increase after the late 1990s, the rate of seasonal advancement in northern temperate and boreal forests (inferred from satellite measurements of the Normalized Difference Vegetation Index) decreased significantly between 1999 and 2015. This was attributed to a reduced sensitivity of vegetation phenology to temperature. Building on this, Shi et al. (2025) applies the concept of thermal optima, highlighting that ecosystems already near or beyond their optimal growth temperatures exhibit diminished or even reversed phenological shifts in response to further warming. Their results suggest that, under ongoing climate change, the early spring advances seen historically may slow or reverse in many parts of the world. Consistent with these findings, a study focused on Siberia by Tran et al. (2024) reported little to no change in the timing of the CUP onset or termination between 2010 and 2021, implying relative stability in carbon uptake

patterns despite climatic shifts.

Climate variability regulates photosynthesis and respiration, influencing phenology, growing season length, and CUP dynamics. While phenology and growing season changes have been widely studied, changes in the CUP, particularly in recent decades, remain poorly constrained. Recent CUP studies are also limited by their reliance on single data sources, such as eddy-covariance flux measurements (e.g. Fu et al. (2017); Zhou et al. (2021)). Eddy-covariance data are constrained by their limited spatial footprint and sparse network and therefore do not provide a representative large-scale view of Northern Hemisphere CUP dynamics. Consequently, the link between regional surface flux changes and large-scale atmospheric expressions of the CUP remains poorly understood. In this context, our study advances the field by examining the CUP from multiple complementary perspectives, combining atmospheric CO_2 observations with flux products from bottom-up and top-down approaches, and using atmospheric transport modelling to enable a consistent comparison in concentration space. This integrated framework enables us to identify robust signals that are consistent across independent data sources. Our study specifically focuses on the following questions:

1) How has the CUP timing evolved in recent decades?
2) How does CUP timing differ across regions?
3) How do key drivers such as gross primary productivity (GPP), terrestrial ecosystem respiration (TER) and temperature contribute to the trends in CUP timing?

To answer these questions, we combine atmospheric CO_2 dry-air mole fraction data from the NOAA/GML CCGG Cooperative Air Sampling Network with NEE fluxes from top-down atmospheric inversions — Jena CarboScope (Rödenbeck et al., 2003) and CarbonTracker Europe (van der Woude et al., 2025a) — and bottom-up, data-driven estimates, FLUXCOM-X-Base (Nelson et al., 2024). Atmospheric CO_2 reflects the combined influence of terrestrial, oceanic, and anthropogenic fluxes and is influenced by atmospheric transport. Top-down inversions infer surface fluxes consistent with atmospheric observations, however, they depend on transport models and prior assumptions, introducing structural uncertainties. Bottom-up products such as FLUXCOM-X-Base are driven by local observations and machine learning but have larger uncertainties in regions with sparse site coverage and may not fully capture large-scale flux patterns. Combining these approaches and evaluating consistency across these flux-based and mole-fraction-based perspectives, we establish an integrated framework that has not been leveraged in previous studies. To directly compare ecosystem-driven signals with large-scale CUP shifts, we generate synthetic CO_2 mole fractions by performing forward transport simulations of NEE fluxes. Further, we leverage GPP and TER fluxes from FLUXCOM-X-Base to understand how they contribute to the NEE changes.

The remainder of this chapter is structured as follows. Section 4.2 describes the datasets used, including atmospheric CO_2 dry-air mole fraction measurements, surface flux estimates from top-down inversions and bottom-up data-driven products, and mixing ratios generated through forward transport simulations. Section 4.3 outlines the methods used to derive the timing of the CUP from both atmospheric and NEE flux data and to assess the respective roles of GPP and TER. Section 4.4 presents the main results, including global and regional trends in CUP timing, comparisons between observation- and model-based CUP estimates, and the contributions of GPP and TER to these changes. In Section 4.4.4, we discuss the implications of these findings for understanding recent shifts in terrestrial carbon dynamics, and Section 4.6 summarizes the key conclusions of this study.

4.2 Data

4.2.1 Ecosystem fluxes

Jena CarboScope

We use NEE fluxes from the CarboScope simulation r76nbetEXToc v2025 (Rödenbeck et al., 2018), which is part of the Global Carbon Budget 2025 (GCB2025) inversion ensemble (Friedlingstein et al., 2025). The NEE fluxes are estimated at a spatial resolution of about 2° longitude × 2° latitude at daily temporal resolution. CarboScope employs the TM3 atmospheric transport model (Heimann & Körner, 2003) within a variational Bayesian inversion framework to optimize surface carbon fluxes against atmospheric CO_2 observations (Rödenbeck et al., 2018). The version r76nbetEXToc v2025 was generated through a two-step procedure. In the first step, interannual anomalies in NEE were regressed against observed air temperature anomalies to capture the temperature sensitivity of NEE. In the second step, remaining interannual variability not explained by this regression was incorporated explicitly using long-term atmospheric CO_2 measurement records (van der Woude et al., 2025b; Rödenbeck et al., 2018)). This version will be referred to as CarboScope in rest of the text.

CarbonTracker Europe

The other inversion-based NEE fluxes were obtained from the CarbonTracker Europe dataset (version CTE2025 (van der Woude et al., 2025a; Peters et al., 2005), included in the GCB2025. The data are provided on a regular latitude-longitude grid at a spatial resolution of 1° × 1°. Like CarboScope, CarbonTracker integrates atmospheric CO_2 measurements with transport models and surface flux prior information to produce optimized estimates of carbon exchange between the land, ocean, and atmosphere. It differs from CarboScope in several key aspects: it uses the TM5 atmospheric transport model (Krol et al., 2005), applies an ensemble Kalman filter (EnKF) optimisation framework,

and represents surface fluxes through biome-based state vector elements, for which scaling factors are optimised during the inversion (Peters et al., 2005; van der Laan-Luijkx et al., 2017). These methodological differences provide an independent and complementary NEE dataset to help characterize surface flux differences, which remain large at the northern high latitudes (van der Woude et al., 2023a). The dataset will be referred to as CTE in rest of the text.

FLUXCOM-X-BASE

In addition, we use FLUXCOM-X-BASE NEE and GPP products (Nelson et al., 2024). These fluxes are derived by applying machine learning techniques to surface eddy covariance flux measurements and meteorological and remote sensing data, offering a data-driven representation of terrestrial carbon exchange. The fluxes have a spatial resolution of 0.05° longitude × 0.05° latitude and daily temporal resolution (Nelson et al., 2024). TER fluxes are calculated by adding GPP to NEE from the same dataset (TER = NEE + GPP). Although only NEE is directly measured at flux tower sites, it is partitioned into its component fluxes, GPP and TER, using the night-time partitioning method after (Reichstein et al., 2005). The FLUXCOM-X BASE product uses these partitioned GPP estimates as training targets in a machine learning framework. In addition, upscaled GPP products have undergone extensive cross-validation across spatial and temporal scales, and shows strong agreement with independent proxies for GPP, such as satellite-based solar-induced chlorophyll fluorescence (SIF) measurements from TROPOMI (Nelson et al., 2024).

4.2.2 Temperature data

We use monthly mean 2-m air temperature from the ECMWF Reanalysis v5 (ERA5) (Hersbach et al., 2020; Copernicus Climate Change Service (C3S), 2023) for the Northern Hemisphere, focusing on the spring months. ERA5 provides globally gridded fields at 0.25° × 0.25° resolution.

4.2.3 CO_2 dry-air mole fraction data

Measurements

We use discrete CO_2 dry-air mole fraction measurements from flask sampling at different background observational sites in the Northern Hemisphere (above 30° N) within the NOAA/GML CCGG cooperative air sampling network (inset Fig. 4.1, Table A.1). The data were obtained from the NOAA data archive. These sites were selected based on their long-term data records (starting at least from 2000) and their distribution across the Northern Hemisphere, with approximately one station for every 5 degrees of latitude. Their remote locations minimize local flux influences, ensuring that the observations reflect large-scale patterns of surface fluxes transported to the sites. There, air samples are

collected in glass flasks under background conditions, making the dry-air mole fractions representative of the zonal mean atmospheric composition (Langenfelds et al., 2002). This data set will be referred to as NOAA data in the rest of the text.

Simulated time series

Further, we use simulated atmospheric CO_2 mole fractions based on optimized fluxes from the inversion systems described above (CTE and CarboScope). Within GCB2025 ensemble's quality-control framework, CO_2 mole fraction fields were generated at the flask sampling frequency of observational sites (van der Woude et al., 2025a) included in the ObsPack products (Schuldt et al., 2023). From these, we use the simulated mole fractions corresponding to the sites analyzed in this study. We limit our analysis to these two inversion products that provide publicly available fluxes at the temporal resolution required for this study. In addition they employ distinct optimization frameworks and independent atmospheric transport models, resulting in structurally different representations of surface carbon fluxes. Further, to make it possible to directly compare FLUXCOM-X-BASE NEE flux products to signals observed in atmospheric CO_2 time series, we generated CO_2 mole fraction fields, using forward simulations with an atmospheric transport model as explained in Sect. 4.3.3.

We evaluate changes in CUP timing over the period 2001–2021, which represents the common time frame across all datasets.

4.3 Methods

4.3.1 Time-series analysis

The flask time-series data are discrete, contain gaps, and the influence of local fluxes and synoptic variability act as noise over the signal we want to isolate here. To facilitate analyses, we apply the ensemble of first derivative (EFD) method described in Kariyathan et al. (2023) for curve-fitting and estimating the metrics describing the timing of the CUP (onset, termination and duration). The CUP metrics derived from atmospheric CO_2 time series are hereafter referred to as CUP_{MR}. In the EFD method, the CUP_{MR} timing is estimated from the first derivative of the detrended and smoothed CO_2 mixing ratio seasonal cycle curves. Threshold values of this derivative relative to the minimum obtained during the peak uptake each year are used to identify the onset and termination (15% and 0%, respectively, following Kariyathan et al. (2023)). The same method (EFD) is applied to the simulated time series to estimate the CUP_{MR}.

4.3.2 CO_2 flux analysis

NEE fluxes from multiple products described in Sect. 4.2.1 are used to analyse surface-level changes in CUP timing. The CUP derived from NEE fluxes is hereafter referred to as CUP_{NEE} and is defined as the period during which NEE is negative, with the spring and autumn zero-crossings corresponding to the onset and termination of CUP_{NEE}, respectively. A 1° × 1° TransCom3 (Gurney et al., 2002; Patra et al., 2008) regional mask was applied to all flux products; for this, the fluxes were first regridded to 1° × 1°to match the resolution of the mask. CUP metrics were then calculated at the grid-cell level (1° × 1°), considering only cells exhibiting a clear seasonal cycle characterised by a single spring and autumn zero-crossing, as multiple crossings can occur in low-latitude or semi-arid regions.

To attribute changes in CUP_{NEE} to shifts in GPP and TER timing, we use GPP fluxes from FLUXCOM-X-Base and derive TER as TER = NEE + GPP from the same dataset. The onset and termination of GPP and TER are determined using thresholds defined as percentages of their respective annual maximum values (we tested 5%, 10%, and 15%). The dates at which GPP or TER cross these thresholds in spring and autumn are interpreted as their onset and termination timings, respectively. As for NEE, the GPP and TER fluxes were regridded to 1° × 1° and the TransCom3 regional mask was applied; the onset and termination metrics were then calculated at the grid-cell level.

The resulting CUP_{NEE}, GPP, and TER metrics were then aggregated to the TransCom3 regions. Linear trends were subsequently estimated on a regional basis using least-squares regression, applying a moving window approach with window sizes ranging from 1 to 6 years.

4.3.3 Forward transport simulations

To enable a direct comparison between FLUXCOM-X-BASE NEE and signals observed in atmospheric CO_2 time series, we generated CO_2 mole fraction time series from this flux using the TM3 atmospheric transport model (Heimann & Körner, 2003). The sampling matched that of the flask measurements at the sites of interest. To disentangle the contributions of GPP and TER to the trends and interannual variability observed in CUP_{MR}, we conducted separate forward runs using NEE fluxes generated specifically with:

i) Variable TER: GPP fluxes from a randomly chosen year (2004) were repeated for the entire study period, while TER was allowed to vary. The corresponding NEE flux was computed as

$$\mathrm{NEE}_{\mathrm{varTER}}(t) = \mathrm{TER}_{\mathrm{variable}}(t) - \mathrm{GPP}_{fixed}(t).$$

ii) Variable GPP: TER fluxes from 2004 were repeated for the entire study period,

while GPP was allowed to vary. The corresponding NEE flux was computed as

$$\mathrm{NEE}_{\mathrm{varGPP}}(t) = \mathrm{TER}_{fixed}(t) - \mathrm{GPP}_{\mathrm{variable}}(t).$$

4.3.4 Temperature trend and sensitivity

Monthly mean 2-m air temperature data for the spring months were first regridded to a $1^\circ \times 1^\circ$ resolution. Temperature trends were then estimated at each grid cell by applying ordinary least squares linear regression to the time series over the period 2001–2021 (Fig. 4.6). For this, CUP_{NEE} onset and temperature were first calculated at each $1^\circ \times 1^\circ$ grid cell and subsequently aggregated to the TransCom3 regions. The regression coefficient between regional mean CUP_{NEE} onset and temperature was then estimated for each region, yielding a single β_T value per region.

4.4 Results

4.4.1 Global Trends

The analysis of CUP_{MR} derived from the CO_2 mole fraction time series (Fig. 4.1, Table A.1) reveals clear latitudinal patterns. At high latitudes, stations consistently exhibit a pronounced advancement in the onset of CUP_{MR}, accompanied by a corresponding lengthening of its duration. The high-latitude sites (∼60°–90°; Storhofdi (ICE), Barrow (BRW), Summit (SUM), Zeppelin (ZEP), and Alert (ALT)) show a clear trend towards an earlier onset of CUP_{MR} ($p < 0.05$, except at ICE), with a mean rate of -0.33 ± 0.05 days yr^{-1} (mean ± standard deviation (SD) across sites). By comparison, trends in CUP_{MR} termination are generally not statistically significant. Consequently, the net effect at these high-latitude stations is a lengthening of the CUP_{MR} duration, driven primarily by the earlier onset (with significant increases in duration observed at BRW, ZEP, and ALT).

Mid-latitude sites, however, do not exhibit a coherent pattern. Among stations located at ∼30°–60°N, only Weizmann (WIS) shows a significant advancing trend in CUP_{MR} onset, while a significant delay in CUP_{MR} termination is detected at Shemya Island (SHM). The absence of a consistent signal across mid-latitude sites suggests that atmospheric transport differs between high and mid-latitude sites, with mid-latitude sites integrating more heterogeneous ecosystem signals.

The coherence of advancing CUP_{MR} onset trends across independent high-latitude stations suggests a large-scale, hemispherically coordinated shift in spring carbon dynamics rather than isolated local effects (Fig. 4.1). Given that high- and mid-latitude Northern Hemisphere ecosystems largely shape the seasonal CO_2 cycle at these sites (Randerson et al., 1997; Parazoo et al., 2011), these pronounced trends point to substantial changes in spring carbon uptake dynamics in these regions. To investigate

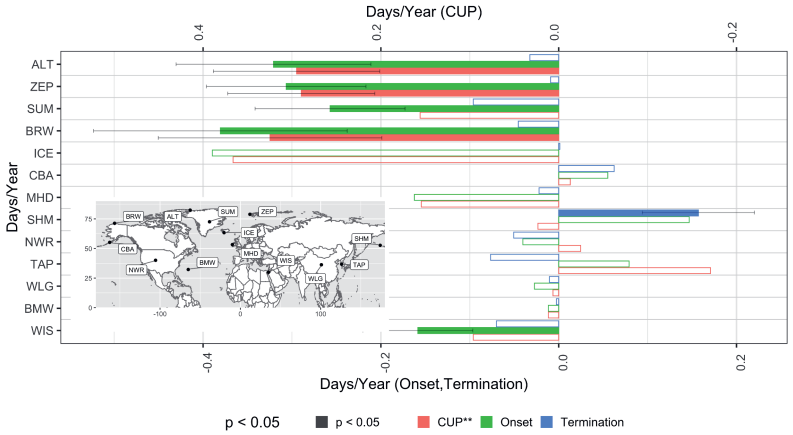


Figure 4.1: Slope of regression line fitted to the onset, termination, and duration of the CUP_{MR} over the time period 2001–2021. The filled columns denote significant slopes ($p < 0.05$). **Note that slope for the CUP_{MR} duration is opposite in sign, and is shown on the x-axis on the top. The inset map shows the geographic locations of the sites listed along the y-axis, which are sorted by station latitude.

the regional expression of these changes, we turn to surface NEE fluxes (Sect. 4.3). As a first step, we assess whether CUP_{MR} derived from NEE fluxes reproduces the advancing trends observed in the atmospheric record at the five high-latitude sites (ALT, ZEP, SUM, BRW, and ICE; Fig. 4.1).

Figure 4.2 compares trends in CUP_{MR} onset derived from the NOAA atmospheric observations at the five most northerly stations (ALT, BRW, ICE, SUM, ZEP) with those obtained from forward simulations sampled at the same locations and times, driven by different NEE products (CarboScope, CTE, and FLUXCOM-X). Across all sites and datasets, trends are negative, indicating a consistent advancement of CUP_{MR} onset over the study period. The results based on the CTE fluxes exhibit significant negative trends at all sites, ranging from -0.15 ± 0.10 to -0.34 ± 0.05 days yr^{-1} (slope ± SD) and show consistently strong agreement with the timeseries of CUP_{MR} onset derived from the atmospheric measurements, as reflected by moderate to high correlation coefficients. The analysis using CarboScope fluxes similarly shows an advancing CUP_{MR} onset signal, and shows moderate to high correlation (except at ICE, (R = 0.10)) with the atmospheric measurements based CUP_{MR} onset interannual variability. The weak slope and low correlation coefficient for CarboScope at ICE may be attributed to the exclusion of this site from the model assimilation. The results using FLUXCOM-X NEE generally display weak to moderate correlations (R = 0.21 to 0.70) with the observation based CUP_{MR}

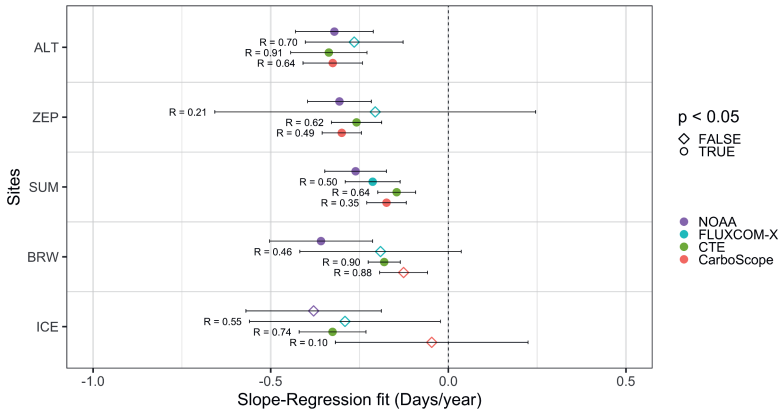


Figure 4.2: Trends in CUP_{MR} onset, derived from atmospheric observations (NOAA) and forward transport simulations using three different NEE products (FLUXCOM-X, CTE and CarboScope) for a subset consisting of the five most northerly stations from Fig. 4.1. The trend is calculated as the slope of the fitted regression line, and given in days yr^{-1}. Colours represent the data source for CUP_{MR}. Filled circles denote statistically significant trends ($p < 0.05$), whereas open diamonds indicate non-significant trends. Text labels show Spearman's correlation coefficients between the interannual variability of the model-derived CUP_{MR} onset and that derived directly from the atmospheric observations. Error bars show the 1σ standard deviation.

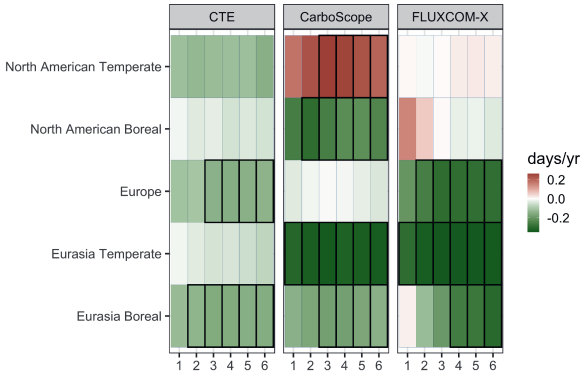


Figure 4.3: The spatial pattern of rolling-window trends in CUP_{NEE} onset across TransCom3 regions. The x-axis show the size of the averaging window (in years) and the y-axis shows the TransCom3 regions. Boxes with black borders indicate statistically significant trends ($p < 0.05$). Colours represent changes in CUP_{NEE} onset: red indicates that the CUP is starting later over time, and green indicates that is is starting earlier, as shown in the legend.

onset interannual variability, and fewer statistically significant trends. The weaker performance of FLUXCOM-X in reproducing the interannual variability of CUP_{MR} onset is consistent with known limitations of data-driven flux products (Nelson et al., 2024; Upton et al., 2024). The different datasets (Fig. 4.2) agree on the direction of change, with differences in trend magnitude and statistical significance likely arising from model framework differences (e.g., bottom-up vs. top-down approaches, optimization methods, and atmospheric transport models).

The mean CUP_{MR} onset trends (reported as the average of model and observation derived trends ± SD, $n = 4$) is –0.31 ± 0.02, –0.21 ± 0.05, –0.26 ± 0.07, –0.20 ± 0.03, and –0.27 ± 0.02 days yr^{-1} at ALT, BRW, ICE, SUM, and ZEP, respectively. Furthermore, a joint hemispheric estimate with these five northerly sites — calculated by first averaging trends across sites within each dataset and then across datasets — yields –0.25 ± 0.03 days yr^{-1} (95% CI: –0.30 to –0.2 days yr^{-1}). This result indicates a coordinated, large-scale advancement in the high-latitude Northern Hemisphere CUP onset that is consistently detected across observational and modeling frameworks.

4.4.2 Regional trends

The time-series analysis of atmospheric CO_2 mole fraction measurements provides insights into large-scale changes across the Northern Hemisphere. However, differences emerge among observation sites due to regional variations in CUP_{NEE} trends and dif-

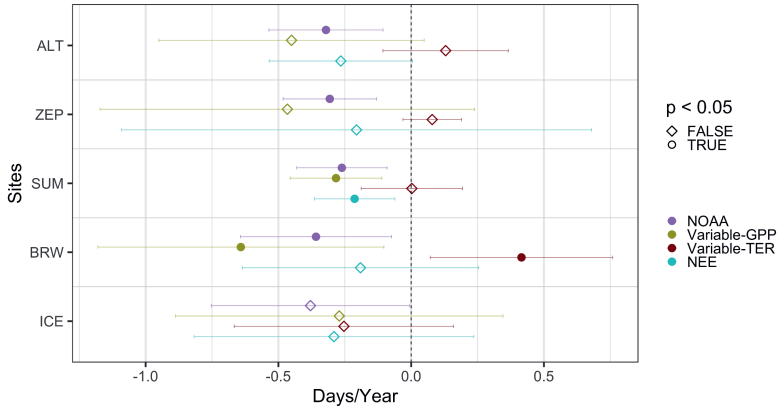


Figure 4.4: Trends in CUP_{MR} onset, derived from atmospheric observations (NOAA), from forward simulations using NEE and NEE with variable GPP or variable TER, derived using FLUXCOM-X fluxes (Sect 4.3.3). The trend is calculated as the slope of the fitted regression line (days yr^{-1}). Filled circles denote statistically significant trends ($p < 0.05$), whereas open diamonds indicate non-significant trends. Error bars show the 1-σ standard deviation.

ferences in atmospheric transport influencing the signals integrated at these locations (Kariyathan et al., 2025). Figure 4.3 focuses on the regional signals in NEE directly, showing a coherent advancement of CUP_{NEE} onset across Eurasian Boreal regions, while North American responses are weaker and less consistent across datasets. Across the three flux products, negative slopes, indicating earlier onset, dominate in Eurasia. The magnitude of the advancing trends is generally largest in FLUXCOM-X and CarboScope for the Eurasian Temperate region, with mean slopes of -0.34 and -0.33 days yr^{-1} (averaged across windows), while CTE shows more moderate and non-significant slopes that are nevertheless consistently negative. The persistence of negative slopes across a wide range of rolling window lengths indicates that the advancing signal is not an artefact of short-term variability but instead reflects a sustained shift in seasonal carbon dynamics. In contrast, North American regions are less consistent across years, and across models. North American Temperate shows weak and mostly non-significant trends, with CarboScope even indicating a delayed onset (positive slopes) across several window lengths. North American Boreal exhibits advancing trends in CarboScope, but these are less consistently reproduced in CTE and FLUXCOM-X.

4.4.3 Contribution of GPP and TER to CUP Timing

To determine if the negative trends in both CUP_{MR} and CUP_{NEE} onset are dominated by GPP or TER variability, we analysed simulations using the FLUXCOM-X partitioned

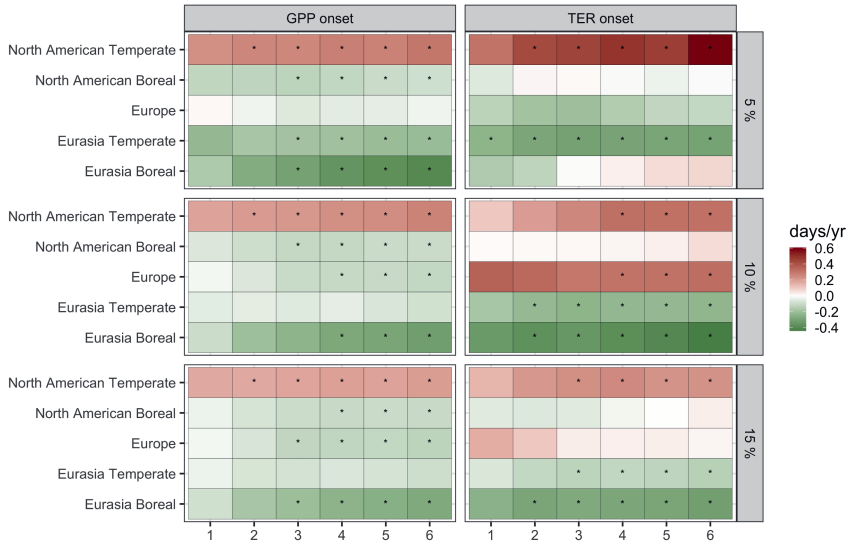


Figure 4.5: The spatial pattern of rolling-window (in years) trends in GPP and TER onset from the FLUXCOM-X product. The x-axis show the size of the averaging window and the y-axis shows the TransCom3 regions. The panel labels to the right show the threshold (percentage of maximum GPP/TER) used for estimating the onset. Red (green) tiles indicate that the CUP is starting later (earlier) over time. Tiles with asterisks represent statistically significant trends ($p < 0.05$).

fluxes, varying only one flux component at a time, as described in Sect. 4.3.3.

Our analysis shows that GPP fluxes from FLUXCOM-X reproduce the direction of the trend in CUP_{MR} onset. This is illustrated in Figure 4.4 where simulations of CUP_{MR} onset driven by variable-GPP reproduce the advancing onset trends observed at our subset of high-latitude sites. In contrast, simulations with variable-TER show either weak or even positive trends in CUP_{MR} onset over time (e.g., 0.42 ± 0.18 yr^{-1} (slope ± SD) at BRW). While the variable-GPP simulations capture the direction of the onset trends, they tend to overestimate the magnitude of the advancement. For example, at BRW analysis of the variable-GPP simulation (green) gives a trend of -0.64 ± 0.28 days yr^{-1}, whereas the NOAA-based trend (purple) is -0.36 ± 0.15 days yr^{-1} and NEE (variable GPP and TER) shows a trend of -0.19 ± 0.23 daysyr^{-1} (slope ± SD).

To better understand the regional contrasts in NEE that we described in Sect. 4.4.2, we examined trends in GPP and TER onset timing across TransCom3 regions for the FLUXCOM-X fluxes directly (Fig. 4.5). The onset of GPP and TER fluxes can advance or delay CUP_{NEE} onset depending on their relative magnitude. If GPP advances more strongly than TER, an earlier CUP_{NEE} onset is expected, whereas comparable or compensating shifts in both fluxes may result in little or no net change. However, in some regions, comparable advances in both fluxes are still associated with an earlier CUP_{NEE} onset, indicating that onset timing alone does not fully explain the observed changes. This suggests that GPP increases more rapidly in the early growing season, for example in response to warming.

In the Eurasian Boreal region, GPP onset shows a consistent advancing trend across thresholds and temporal windows. The magnitude of GPP onset trends ranges from -0.09 ± 0.15 to -0.40 ± 0.07 days yr^{-1} (mean ± SD). TER onset also indicates earlier timing at thresholds of 10% and 15%, while at 5% the trends are weak and highly sensitive to the temporal window. The greater consistency at higher thresholds suggests that TER onset is more reliably captured later in the seasonal progression. Although GPP and TER exhibit broadly similar advances in onset timing, the earlier CUP_{NEE} onset (Fig. 4.3, FLUXCOM-X) indicates that the transition to net carbon uptake is not governed by onset timing of GPP and TER alone, but by the relative evolution of the two fluxes. Even comparable shifts in onset timing can lead to an earlier crossing of GPP and TER, if GPP increases more rapidly or attains larger magnitudes earlier in the spring in response to warming. Similarly, in the Eurasian Temperate region, both GPP and TER exhibit advancing onset, with TER showing a stronger advance. Despite this, CUP_{NEE} onset also advances (Fig. 4.3, FLUXCOM-X), indicating that onset shifts alone do not determine the timing of net carbon uptake. Instead, increases in GPP during the early growing season are sufficient to offset the stronger advance in TER, leading to an earlier transition to net carbon uptake. In Europe, GPP onset shows advancing trends

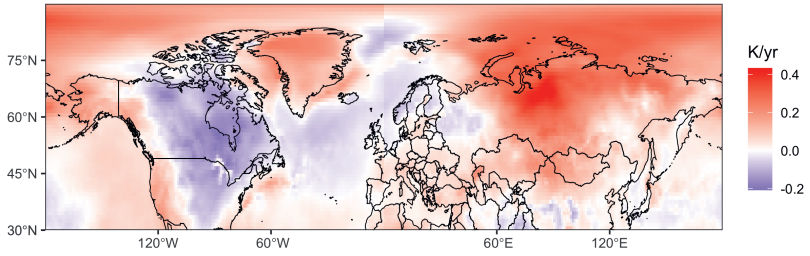


Figure 4.6: Spatial distribution of trends in monthly mean 2-m surface air temperature for the month of April over the period 2001–2021. Red and blue colours indicate positive and negative trends respectively.

that are statistically significant primarily at higher thresholds (10% and 15%) and for longer temporal windows. The TER onset shows delayed trend at higher thresholds. The GPP and TER onset trends for the thresholds, 10% and 15%, is consistent with the strong advancing CUP_{NEE} onset (Fig. 4.3, FLUXCOM-X).

In the North American Boreal region, GPP onset generally indicates earlier timing, particularly for longer temporal windows, while TER onset trends remain weak and variable across thresholds. Despite the advance in GPP onset, the lack of a coherent TER response likely introduces variability in the relative timing of the two fluxes, resulting in no robust trends in CUP_{NEE} onset (Fig. 4.3, FLUXCOM-X). In the North American Temperate region, both GPP and TER exhibit later onset across thresholds. GPP onset trends range from 0.17 ± 0.11 to 0.30 ± 0.05 days yr^{-1}, while TER onset trends range from 0.11 ± 0.29 to 0.61 ± 0.06 days yr^{-1} (slope $\pm$ SD). TER onset trends show more comparable values at higher thresholds (10% and 15%), suggesting reduced confidence in the lower-threshold estimates. In contrast to the Eurasian Boreal region, where similar advances in GPP and TER are associated with an earlier transition to net carbon uptake, no consistent trend in CUP_{NEE} onset is observed in the North American Temperate region (Fig. 4.3, FLUXCOM-X). This lack of a clear CUP_{NEE} response, together with delays in both GPP and TER, suggests that the two fluxes act in a compensating manner, and that changes in GPP magnitude or rate of increase are unlikely to dominate in this region, consistent with the weaker spring warming observed relative to Eurasian regions (Ding et al., 2025).

4.4.4 Spring temperature controls on regional CUP onset trends

Previous studies have identified spring temperature as a key driver of CUP timing, and have shown that regional contrasts in onset trends reflect spatial differences in spring

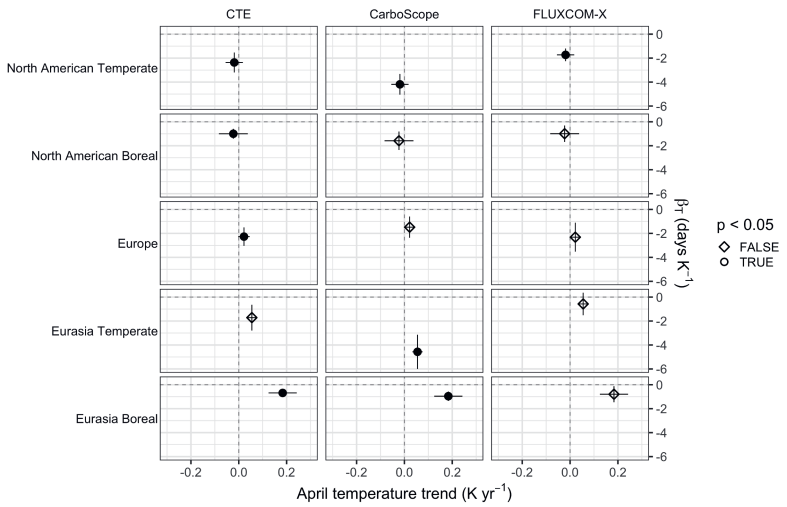


Figure 4.7: CUP$_{NEE}$ onset - Temperature sensitivity (β_T) against April temperature trend across the Transcom3 regions. Panel title (top) represents the various CUP$_{NEE}$ data sources.

warming (Barichivich et al., 2012). In particular, stronger spring warming over Eurasia relative to North America has been linked to a more pronounced advancement of CUP onset in Eurasian ecosystems (Barichivich et al., 2012). We analysed trends in ERA5 (Hersbach et al., 2020) monthly mean 2-m surface air temperature for Northern-Hemisphere spring months. Our results show that this pattern persists in the last two decades (2001–2021). Among all of the spring months (March–May), April shows the clearest hemispheric contrast (Fig. 4.6): Eurasia exhibits widespread warming, while large parts of North America show weak or even negative trends, particularly in central and eastern regions. In Eurasia, stronger April warming likely drives the advancing CUP$_{NEE}$ onset trend, whereas in North America the weaker warming may limit early-season photosynthetic activity, contributing to the weaker advance or delayed CUP$_{NEE}$ onset trends.

We further examined the temperature sensitivity of CUP$_{NEE}$ onset (β_T Sect. 4.3.4). Figure 4.7 shows β_T for each TransCom3 region plotted against the corresponding April temperature trend (K yr^{-1}), enabling an assessment of temperature-driven changes in onset trends. The onset trend can be determined by the combined effect ($\beta_T \times$ April temperature trend) of the temperature sensitivity and the April temperature trend. Figure 4.7 shows that temperature exerts a strong control on CUP$_{NEE}$ onset in Eurasian boreal and temperate regions. Across all regions and datasets, β_T is consistently negative. The magnitude of β_T is largest in the Eurasian and North American

temperate regions, particularly for CarboScope. April temperature trends exhibit a pronounced regional contrast. Eurasian regions show predominantly positive trends across all datasets, especially in the boreal and temperate zones, whereas North America exhibits weaker trends, including cooling signals. Europe shows only modest warming.

The combination of negative β_T and positive temperature trends in Eurasian boreal and temperate regions implies a robust, temperature-driven advancement of CUP_{NEE} onset across all datasets. In the Eurasian temperate region, FLUXCOM-X shows a weaker β_T but a strong advancement in CUP_{NEE} onset (Fig. 4.3). The stronger temperature sensitivity in CarboScope may reflect the incorporation of temperature variability within its flux optimization framework; however, this does not necessarily imply greater reliability, but rather highlights structural differences between flux products. In Europe, negative β_T values together with weak positive temperature trends suggest a small advancement in CUP_{NEE} onset. However, the stronger advancement seen, for example in FLUXCOM-X (Fig. 4.3), suggests that other factors, such as earlier snowmelt, favourable soil moisture or light availability, may contribute to the advancement in CUP_{NEE} onset. The weak CUP_{NEE} onset trend in CarboScope is consistent with the weak temperature trend in this region (0.022 K yr^{-1}) and its relatively low temperature sensitivity ($\beta_T = -1.48$ days K^{-1}).

In North America, the combination of negative β_T and weak or slightly negative temperature trends would be expected to result in weak or delayed trends in CUP_{NEE} onset. However, advancing trends are observed in the North American boreal region (CTE and CarboScope) and in the temperate region (CTE) as shown in Fig. 4.3), indicating the influence of non-temperature drivers. By contrast, the strong delayed trend in CarboScope, CUP_{NEE} onset is consistent with the magnitude of β_T.

4.5 Discussion

Our analysis (Fig. 4.1) reveals a pronounced and spatially coherent advancement of CUP_{MR} onset at multiple high-latitude stations over the period 2001–2021. The magnitude of this shift, ranging from approximately 2.6 to 3.9 days per decade, is comparable to earlier estimates (2–4 days per decade) of onset advancement derived from atmospheric CO_2 records for the late 20th century (e.g., 1980–2002, (Piao et al., 2008). The persistence of similar rates of advancement into the most recent two decades suggests that the shift toward earlier net carbon uptake in northern ecosystems remains an active and ongoing process. The observed trends reflect substantial shifts in high- and mid-latitude ecosystems, which exert a strong influence on the seasonal cycle of atmospheric CO_2 at the high latitude sites (Randerson et al., 1997; Parazoo et al., 2011). In contrast to the robust trend showing an earlier onset of CUP_{MR},

changes in the trend of CUP_{MR} termination over time are small and generally not statistically significant. As a result, the lengthening of the CUP_{MR} duration at high latitudes is primarily driven by an earlier onset. Previous studies have reported inconsistent termination trends, with some indicating a delayed termination of the carbon uptake period (Piao et al., 2008) and others an earlier termination (Barichivich et al., 2012), depending on the study period. The absence of a consistent termination signal across different study periods suggests that processes determining the end of the CUP in autumn are more variable over time than those determining its onset in the spring.

The strong and consistent advancement of CUP_{MR} onset at high latitudes, indicate a dominant shift toward earlier net carbon uptake across northern ecosystems. Independent flux products successfully reproduce the direction and large-scale structure of these trends, supporting their use for interpreting spatial variability in seasonal carbon dynamics. At the regional scale, the contrast in CUP_{NEE} onset trends, we find between Eurasian and North American regions is consistent with previously documented differences in vegetation dynamics between continents, namely greening trends in Eurasia and more heterogeneous or browning tendencies in parts of North America (Bi et al., 2013; Barichivich et al., 2012). In particular, Barichivich et al. (2012) identified a more pronounced advancement of the CUP in Eurasian ecosystems. However, unlike their approach, which relied primarily on a single observational stream (CO_2 mole fraction measurements) and indirect associations between CO_2 seasonality and temperature, our multi-dataset framework enables the identification of regions with consistent changes across data streams. Eurasian regions show relatively more consistent advancing CUP_{NEE} onset signals, making them a key driver of the earlier CUP_{MR} onset observed at high-latitude atmospheric stations. In contrast, Tran et al. (2024) did not detect a significant trend in CUP timing at the ZOTTO station in Siberia; this is likely as their analysis was based on a shorter observational period (2010-2021) and a single site.

4.5.1 Drivers of CUP_{MR} and CUP_{NEE}

Simulations driven by variable GPP reproduce the observed advancement in CUP_{MR} onset at high latitudes. In contrast, simulations driven by variable TER and fixed GPP yield weak or opposing trends relative to the observations. This indicates that GPP variability is a stronger driver of CUP_{MR} onset than TER. From the analysis of regional trends in GPP and TER onset, we find that the changes in CUP_{NEE} onset cannot be explained by temporal shifts in either flux alone. Rather, the transition to net carbon uptake reflects the relative evolution of the two fluxes during the early spring period. In particular, an earlier CUP_{NEE} onset can occur even when GPP and TER advance at similar rates, provided that GPP increases more rapidly than TER following onset. This highlights that the timing of net carbon uptake is governed not only by onset dates, but also by the early-season growth of photosynthetic activity. This interpretation is

consistent with broader Northern Hemisphere evidence that spring warming enhances early-season GPP, thereby promoting earlier net carbon uptake (Zheng et al., 2022). This framework helps explain why Eurasian regions exhibit a more coherent advancement of CUP_{NEE} onset. Quantitatively, the GPP onset in the Eurasian boreal region advances at approximately –2.5 ± 0.9 days decade^{-1} (multi-model mean), comparable to satellite-based spring phenology estimates for boreal forests reported by Deng et al. (2019) (3.38 ± 0.08 days decade^{-1} over 2001–2017), with the strongest contribution from Eurasian boreal forests. Despite a similar advancement in TER onset, the advancing CUP_{NEE} onset suggests that warming more effectively accelerates early-season photosynthetic development relative to respiration in this region. In contrast, the weak or absent trends in CUP_{NEE} onset in the North American temperate region arise from compensating GPP and TER onset trends, where delays in both fluxes limit any systematic change in their relative balance. This interpretation is consistent with evidence of a pronounced spring warming asymmetry between Eurasia and North America, with stronger warming over Eurasia during 1979-2021 (Ding et al., 2025). It is further supported by studies showing that Eurasian boreal ecosystems exhibit stronger photosynthetic responses to warming than their North American counterparts (Muccio et al., 2025). Here we have used GPP and TER fluxes from a single source (Fluxcom-X product), which limits our ability to address the varying response in CUP_{NEE} onset trends across the different models.

Earlier work by Barichivich et al. (2012) linked hemispheric differences in carbon uptake timing to variations in the thermal growing season between Eurasia and North America. Consistent with this, our analysis shows marked differences in spring surface air temperature trends, particularly in April, with widespread warming across Eurasia and weaker or regionally negative trends in North America, further corroborated by recent studies such as Ding et al. (2025). Figure 4.7 further demonstrates how CUP_{NEE} onset reflects the combined influence of regional warming and its temperature sensitivity (β_T). While β_T is consistently negative across regions, indicating earlier onset with warming, the direction of CUP_{NEE} onset trends is largely determined by the temperature trend itself. However, temperature alone does not fully explain the observed CUP_{NEE} onset trends, particularly in North America. Recent studies report stronger photosynthetic sensitivity to warming in Eurasian boreal ecosystems compared to North America (Muccio et al., 2025), but such differences in β_T are not evident here. This discrepancy likely arises from differences in the quantities being compared and the methodological framework. While Muccio et al. (2025) focus on the direct sensitivity of GPP to temperature, our analysis evaluates the timing of CUP_{NEE} onset, which is an emergent metric reflecting the interaction between GPP and TER. As a result, differences in GPP sensitivity may not translate directly into differences in CUP_{NEE} onset sensitivity.

In this study we used large-scale observational constraints from atmospheric CO_2 measurements to diagnose changes in CUP timing. Eddy-covariance flux towers provide

direct ecosystem-scale observations of NEE and therefore an important observational constraint on carbon exchange. However, their smaller footprints and sparse spatial coverage, particularly across high-latitude regions, limits their ability to resolve the hemispheric-scale signals investigated here. While our analysis examined how shifts in GPP and TER influence CUP timing, NEE can also be affected by disturbances and extreme climate events. Processes such as fire, insect outbreaks, droughts, and heatwaves can alter both photosythetic uptake and respiration (Mekonnen et al., 2025; Sippel et al., 2018), and may therefore affect the timing and interannual variability of the CUP. Future work could extend this approach by combining atmospheric observations with disturbance datasets and event-based analyses to assess whether large-scale atmospheric signals capture the impacts of regional extreme events, and whether the atmospheric response to disturbance differs across regions such as Eurasia and North America. We focused primarily on temperature because previous studies have identified spring temperature as the dominant large-scale driver of CUP timing. Other climate factors such as soil moisture and radiation can also influence ecosystem carbon exchange, but their effects tend to operate more locally or episodically. Our analysis show that in regions such in North America, other climate variable might contribute to evaluated trends. Consistent with the large-scale temperature control, our analysis reveals that the most coherent signal emerges from the Eurasian boreal region, where a correlation between spring warming, advancing GPP and TER onset, and earlier CUP_{NEE} onset is most evident. The robustness of this signal across independent models and atmospheric constraints indicates that this region plays a decisive role in driving the observed hemispheric shift toward earlier spring net carbon uptake.

4.6 Conclusion

This study assesses changes in the onset of the CUP across northern high latitudes by combining long-term atmospheric CO_2 records with estimates of NEE. Our analysis shows that CUP_{MR} exhibits a strong and consistent advancing trend in onset at high-latitude sites. This signal can be primarily attributed to high-latitude ecosystems, particularly the Eurasian boreal region. The agreement between observational records and inversion-based CUP_{MR} estimates indicates that current flux products capture the large-scale variability needed to interpret spatial changes in carbon uptake seasonality. Regional analyses of CUP_{NEE} reveal a robust and statistically significant advancement of onset across the Eurasian boreal region during the study period. In contrast, North American temperate regions exhibit weaker, inconsistent, or non-significant trends. Our analysis further shows that variability in GPP is the dominant driver of CUP_{MR} onset trends relative to TER. Regional analyses of GPP and TER fluxes show contrasts in their onset timing between the Eurasian boreal and North American temperate regions. However, differences in their timing alone cannot explain the regional contrast in CUP_{NEE} onset trends. Moreover,

our estimates of GPP and TER onset are based on a single product, limiting our ability to assess model inconsistencies in CUP_{NEE} onset trends. The advancing CUP_{NEE} onset in Eurasian boreal and temperate regions is consistent with spring warming in these regions. However, advancing trends in Europe and parts of North America are not fully explained by temperature, suggesting the influence of additional climatic drivers.

Appendix

Table A.1: Observational sites of NOAA/ESRL network used in this study

Weizmann Institute of Science at the Arava Institute, Ketura, Israel	WIS	29.96°N	35.06°E
Tudor Hill, Bermuda, United Kingdom	BMW	32.26°N	64.88°W
Mt. Waliguan, Peoples Republic of China	WLG	36.29°N	100.90°E
Tae-ahn Peninsula, Republic of Korea	TAP	36.74°N	126.13°E
Niwot Ridge, Colorado, United States	NWR	40.05°N	105.59°W
Shemya Island, Alaska, United States	SHM	52.71°N	174.13°E
Mace Head, County Galway, Ireland	MHD	53.33°N	9.90°W
Cold Bay, Alaska, United States	CBA	55.21°N	162.72°W
Storhofdi, Vestmannaeyjar, Iceland	ICE	63.40°N	20.29°W
Barrow Atmospheric Baseline Observatory, United States	BRW	71.32°N	156.61°W
Summit, Greenland	SUM	72.60°N	38.42°W
Ny-Alesund, Svalbard, Norway and Sweden	ZEP	78.91°N	11.89°E
Alert, Nunavut, Canada	ALT	82.45°N	62.51°W

Chapter 5

Synthesis

5.1 Discussion

This thesis set out to better understand the carbon uptake period (CUP), the time of the year when terrestrial ecosystems act as a net sink of atmospheric CO_2, by refining how it is calculated, interpreted, and linked to the underlying ecosystem processes. Through three complementary studies, we developed a new method to robustly extract the onset and termination of the CUP from atmospheric CO_2 records, examined the sensitivity of these metrics to atmospheric transport, and applied them to diagnose regional and temporal trends in the timing and extend of the CUP in the Northern Hemisphere.

Together, these studies explore the value of CUP metrics in carbon-cycle research by addressing the following questions:

- What do recent changes in the timing of the CUP tell us about ecosystem responses to climate variability?
- How sensitive are atmospheric CO_2 measurements to changes in the timing of the biospheric carbon uptake period?
- How can we reduce errors when estimating the timing of the CUP from atmospheric CO_2 time-series data?

The discussion below integrates the findings, outlines their broader implications, and identifies remaining challenges and directions for future research.

5.1.1 Relevance of the CUP in carbon cycle research

Understanding how the land carbon sink responds to climate change is crucial for improving our understanding of its spatial and temporal dynamics, with implications for Earth system models, the global carbon budget, and climate projections. A key indicator of the ecosystem response to climate variability is the seasonal timing of net carbon uptake. Below, we outline reasons why the CUP could become an important diagnostic in carbon cycle research, drawing on insights from our experiments.

The CUP has been shown to be a better proxy for annual NEE than traditional, related metrics such as the growing season length derived from vegetation phenology (Wu et al., 2012). This is because the CUP integrates multiple climate-driven processes governing the balance between photosynthesis and respiration, thereby capturing the combined effects of phenology, seasonal climate variability, and ecosystem physiology in a single metric describing the period of net carbon sequestration (Fu et al., 2017). White & Nemani (2003) investigated how canopy duration relates to yearly carbon storage in deciduous broadleaf forests. By combining eddy-covariance flux measurements with satellite-based phenology indicators, they found that annual NEE had only a weak

association with canopy duration but showed a stronger relationship with the CUP. Analyses of long-term flux-tower records show that anomalies in CUP and the maximum daily NEE together explain a large fraction of the interannual variability in annual NEE (Fu et al., 2017). Previous studies have shown that improving the representation of seasonal timing in terrestrial biosphere models enhances agreement with both eddy-covariance flux data and atmospheric CO_2 observations. For example, Jeong et al. (2012) demonstrated that biases in the modelled spring phenology contributed to mismatches in regional NEE inferred from atmospheric data, while Richardson et al. (2012) showed that improved representation of phenological transitions reduced discrepancies with flux-tower observations, with important implications for improving the representation of terrestrial carbon-cycle processes in Earth system models. Direct measurements of the CUP from eddy-covariance NEE measurements remain spatially limited, as flux towers have a limited footprint, are unevenly distributed and sparse at large scales. This underscores the need to explore complementary approaches and proxy data sources that allow CUP estimation beyond tower locations. Gonsamo et al. (2012) demonstrated how vegetation indices measured by satellites combined with temperature indices can provide CUP estimates at smaller spatial scales.

In this thesis, we investigate how atmospheric measurements integrate signals of NEE variability and how well the CUP derived from atmospheric observations (CUP_{MR}) represents these underlying surface flux dynamics. In Chapter 2, we show that, despite the influence of atmospheric transport, long-term atmospheric CO_2 dry-air mole-fraction records can be used to infer large-scale changes in the CUP. This highlights the value of expanding observational networks such as the Integrated Carbon Observation System (ICOS) to improve spatial coverage and strengthen constraints on continental-scale carbon-cycle processes. We discuss how discrepancies between atmospheric and surface-derived CUP estimates arise from the integration and redistribution of surface flux signals by atmospheric transport, and how this leads to different behaviour across observation sites (Chapter 3). Furthermore, by deriving CUP metrics from multiple data streams, including atmospheric CO_2 time series, atmospheric inversions, and data-driven upscaling products of biospheric fluxes, and systematically comparing these estimates, we establish a diagnostic framework for investigating regional differences in carbon cycle dynamics. We show that cross-dataset comparisons of CUP estimates can enable process-level diagnosis of CUP trends (Chapter 4). For example, differences in the seasonality of the optimized fluxes between the temperature-informed CarboScope inversion configuration and CarbonTracker Europe illustrate how alternative representations of temperature sensitivity can lead to divergent trends in the timing of the CUP (Fig. 4.3).

Here we focused on the long-term changes in CUP_{MR}. However, atmospheric CO_2 records have also been used to detect the impacts of large-scale climate anomalies on the terrestrial carbon cycle. For example, Langenfelds et al. (2002) showed that anomalies in

the atmospheric CO_2 growth rate during the 1997–1998 El Niño reflected a substantial weakening of the tropical land carbon sink, associated with drought conditions and increased fire activity. Extreme events such as droughts, heatwaves, or cold springs have been shown to reduce the terrestrial carbon sink (e.g. Wolf & Paul-Limoges, 2023; Ramonet et al., 2020; Ke et al., 2024). These can also be associated with a delay in the onset of uptake, an earlier termination, or an overall shortening of the uptake period. Because atmospheric CO_2 integrates flux signals over large spatial footprints, shifts in CUP_{MR} could be used to help quantify the timing of large-scale impacts from extreme events across regions and years. The methodological framework developed in this thesis supports such analyses by providing more robust estimates of CUP from atmospheric records, reducing methodological uncertainties relative to previous approaches, and offering insights into transport-related influences at the evaluated monitoring sites.

5.1.2 Reliability of CUP_{MR}

A key aspect of this thesis concerns the reliability of the CUP_{MR}. Establishing the methodological robustness of these estimates and understanding how atmospheric transport influences their interpretation form the foundation for all subsequent analyses: calculating large-scale CUP trends, regional attribution of atmospheric signals, and comparisons between atmospheric, inversion-based, and flux-derived CUP estimates in Chapter 4. Here we discuss how this thesis has contributed to improving the reliability of CUP_{MR} metrics and our recommendations for future studies.

In Chapter 2, we addressed the methodological reliability of CUP_{MR}. Extracting seasonal metrics from discrete atmospheric observations is inherently challenging because the records contain data gaps, measurement noise, and variability associated with synoptic transport (Nakazawa et al., 1997). These sources of variability propagate through the curve-fitting procedure used to isolate the seasonal cycle and can influence the identification of seasonal transition points. Earlier research has recognized these challenges and shown that seasonal metrics can be highly sensitive to the choice of curve-fitting approach (e.g., Pickers & Manning (2015); Barlow et al. (2015)). To evaluate how these uncertainties influence CUP_{MR} timing, we developed the EFD method, which generates an ensemble of plausible seasonal curves and allows uncertainty in seasonal cycle metrics to be quantified (Kariyathan et al., 2023). We further compared the EFD framework with the widely used CCG-CurveFit (Thoning et al., 1989) approach to evaluate structural uncertainty associated with different curve-fitting algorithms. Finally, we examined how alternative definitions of seasonal transition points, like the zero-crossing points, influence estimates of CUP timing. Together, these analyses disentangle uncertainty arising from data variability, curve-fitting methodology, and metric definition, and demonstrate that EFD-based CUP_{MR} estimates are less sensitive to methodological choices and more reproducible across sites.

The atmospheric signals integrate fluxes from multiple components of the carbon cycle, including terrestrial ecosystems, ocean–atmosphere exchange, and anthropogenic emissions, all of which can contribute to the observed seasonal cycle. While the methodological refinement proposed in Chapter 2 increased confidence in the statistical robustness of CUP_{MR}, the next question concerned how well CUP_{MR} reflects changes in surface fluxes. Although observational records from remote background stations have only weak local influence, they remain strongly shaped by atmospheric transport patterns that link each measurement site to upwind regional sources and sinks (Murayama et al., 2007). Previous studies have demonstrated that transport variability can substantially influence seasonal metrics derived from atmospheric CO_2, including the seasonal cycle amplitude (SCA), growth rate, and the timing of zero-crossing dates of the detrended seasonal cycle. For example, Lintner et al. (2006) showed that variability in large-scale circulation contributes significantly to observed SCA trends at Mauna Loa (MLO), complicating direct attribution to biospheric change. More recently, Jin et al. (2022) quantified that shifting wind patterns accounted for nearly 50% of the long-term SCA changes at MLO, illustrating how transport can amplify or dampen underlying surface flux signals. Likewise, analyses of the atmospheric CO_2 growth rate indicate that transport-driven redistribution of surface flux anomalies contribute to the interannual variability of the observed signal (Pandey et al., 2024). Murayama et al. (2007), who showed that nearly half of the observed variability in the downward zero-crossing date at Barrow (BRW) could be explained by changes in atmospheric circulation. Building on this literature, we extend the question specifically to CUP_{MR} by assessing how prescribed changes in CUP_{NEE} are propagated through atmospheric transport. The results show that transport not only introduces additional variability but, also strongly dampens the magnitude of surface-driven shifts. For example, at the well-studied high-latitude site BRW, only about 50% of the variability imposed at the surface is detectable in the resulting atmospheric CUP_{MR} signal (Fig. 3.4). We further show that certain stations, such as Zeppelin (ZEP), exhibit particularly strong regional and seasonal sensitivity, reflecting their changing exposure to distinct upwind flux regions throughout the year.

With this understanding of methodological and transport-related limitations, Chapter 4 evaluates how CUP_{MR} relates to CUP_{NEE} across regions. Previous studies have shown that high-latitude atmospheric stations are primarily influenced by high- and mid-latitude source regions (Randerson et al., 1997; Parazoo et al., 2011). The CO_2 mole-fraction simulations from inversions and data-driven flux products capture both the direction and magnitude of the observed CUP_{MR} onset trends at high-latitude sites reasonably well. However, the NEE products reveal pronounced regional differences in CUP_{NEE} onset across the evaluated Northern Hemisphere TransCom3 regions. A consistent advancement in CUP_{MR} onset is evident only at a subset of sites, primarily at high latitudes, whereas mid-latitude stations do not exhibit such coherence. This contrast

indicates that site sensitivity varies with latitude, reflecting differences in atmospheric footprint. The coherent signal observed at high-latitude sites does not imply uniform changes across both high- and mid-latitude regions, but instead points to a dominant influence from regions that exhibit an advancing CUP_{NEE} onset. By jointly analyzing CUP_{MR} and CUP_{NEE}, we show that the observed advancement in the onset of CUP_{MR} at high-latitude stations is predominantly linked to fluxes in Eurasian ecosystems. This comparison also reveals systematic differences between atmospheric and surface perspectives in the balance between long-term trends and interannual variability. In the atmospheric records, the advancing trend in CUP_{MR} onset generally exceeds year-to-year variability, resulting in robust and statistically significant trends at high-latitude sites as shown in Fig. 4.1. In contrast, CUP_{NEE} derived from surface flux products, particularly when evaluated over shorter rolling windows, exhibits substantial interannual variability and consequently non-significant trends (Fig. 4.3). Implying that the surface flux estimates retain a stronger imprint of local variability arising from short-term climate fluctuations.

These findings have broader implications for carbon-cycle synthesis efforts. Initiatives such as RECCAP-2 (Ciais et al., 2020) combine bottom-up inventories, dynamic vegetation models, atmospheric inversions, and observational constraints to evaluate regional carbon budgets and their uncertainties. Such intercomparison analyses show substantial spread in the simulated seasonal cycle of land–atmosphere CO_2 exchange. For example, Liu et al. (2017) demonstrated that models taking part in the fifth phase of the Coupled Model Intercomparison Project (CMIP5, Taylor et al. (2011)) exhibit large inter-model differences in the amplitude of the seasonal CO_2 cycle, particularly in the Northern Hemisphere extratropics, reflecting divergent representations of GPP and respiration responses to temperature and growing-season dynamics. Similarly, van der Woude et al. (2025a) reported considerable spread among global CO_2 inversion systems in regional flux estimates and seasonal characteristics, despite broadly comparable global annual carbon budgets.

Such intercomparisons have focused primarily on reconciling the magnitude of regional carbon sources and sinks (van der Woude et al., 2025a; Liu et al., 2017; Wenzel et al., 2014), while comparatively less attention has been given to the seasonal phase of CO_2 exchange. More recent work, including van der Woude et al. (2025a), has incorporated CUP-related metrics to better constrain regional uncertainty and highlights that agreement in the annual carbon budget does not necessarily imply consistency in the seasonal dynamics of land–atmosphere CO_2 exchange. The framework developed in this thesis directly supports such synthesis efforts. Our analysis shows inconsistencies in CUP_{NEE} timing across models, in particular in the North American boreal and temperate regions. Model inconsistencies in representing the seasonal timing may reflect differences in model sensitivity to driving factors. For example the temperature sensitivity analysis

showed that the β_T values and temperature trend explained the delayed CUP_{NEE} onset for CarboScope in North American temperate, and not the CUP_{NEE} onset trend for other models.

Analogous to how the amplitude of the atmospheric CO_2 seasonal cycle is commonly used to evaluate model performance, metrics describing the timing of terrestrial carbon exchange could provide an additional constraint on modeled fluxes, in intercomparison frameworks such as CMIP (Taylor et al., 2011) and TRENDY (the Trends and drivers of the regional scale terrestrial sources and sinks of carbon dioxide project, (Sitch et al., 2024)). Similar to the approach used in this study, evaluating whether models reproduce observed shifts in the timing of carbon uptake would complement existing comparisons based on seasonal amplitude and annual carbon budgets. Differences between CUP_{MR} and CUP_{NEE} could further help diagnose whether mismatches arise from biases in the seasonal timing of ecosystem fluxes, atmospheric transport effects, or regional differences in ecosystem responses.

5.1.3 Regional dynamics

The atmospheric record integrates signals from multiple regions with asynchronous seasonal cycle dynamics. The combined analysis of CUP_{MR} and CUP_{NEE} in Chapter 4 provides a consistent picture of how the timing of the CUP varies across latitude and region. While CUP_{MR} captures the large-scale latitudinal gradients (Fig. 4.1) and shows an advancing onset at high latitudes, CUP_{NEE} across models reveals distinct contrasts between Eurasia with advancing and weak or delayed onset trends in North American Temperate (Fig. 4.3). This indicates that regional climate and ecosystem characteristics exert differing controls on CUP timing. To better understand the drivers underlying these regional differences, we further examined the component fluxes, gross primary productivity (GPP) and terrestrial ecosystem respiration (TER). This decomposition shows that, consistent with spring warming trends (Fig. 4.6), both GPP and TER exhibit advancing onset trends in the Eurasian boreal region, whereas delayed onset trends are observed in temperate North America (Fig. 4.5). Given that the atmospheric CUP_{MR} also shows an earlier onset, this indicates that the observed CUP_{MR} trends are primarily driven by flux changes in Eurasia rather than North America (Mahecha et al., 2026). Our transport model experiments in Chapter 3 strengthen this interpretation by demonstrating how regional perturbations in surface flux timing propagate into atmospheric signals at remote sites. Much of the detected advancement in simulated CUP_{MR} onset can be attributed to early-season flux changes in Eurasia, as high-latitude sites such as ALT, BRW, and ZEP are predominantly influenced by Eurasian boreal fluxes (Fig. 3.7), and the advancing trends observed in their CUP_{MR} records are consistent with the earlier CUP_{NEE} onset diagnosed for the Eurasian boreal region. Similarly, SHM shows a significant influence from Eurasian boreal fluxes, yet an advancing CUP_{MR}

onset is not observed here. One possible explanation is that, although the same broad TransCom3 Eurasian boreal region influences SHM as well as sites such as ALT, BRW and ZEP, the relevant source areas within that region may differ. Given its location, SHM may be more strongly influenced by the eastern part of the Eurasian boreal region, where the seasonal signal and its trend may differ from the source areas affecting the high-latitude sites. In addition, the simulations in Chapter 3 isolate the influence of ecosystem fluxes, whereas the observed atmospheric CO_2 signal also reflects contributions from other processes, including ocean-atmosphere exchange. The mismatch between the strong Eurasian boreal influence and the absence of an advancing CUP_{MR} onset at SHM therefore suggests that non-ecosystem fluxes, or their interaction with transport, may also affect the timing signal at this site. A more detailed SHM centric attribution analysis would be needed to determine the relative importance of these possible reasons, which is beyond the scope of this study.

While this study identified clear continental-scale differences in CUP dynamics, particularly between Eurasia and North America, these trends likely also vary at finer ecological scales. A key remaining knowledge gap concerns how changes in CUP timing differ across biomes, and whether distinct ecosystem types contribute differently to the observed atmospheric signals. Continental aggregates can mask compensating or opposing responses among ecosystems that differ in vegetation structure, soil properties, hydroclimatic constraints, and temperature sensitivity. For example, water-limited ecosystems such as semi-arid grasslands and shrublands exhibit strong moisture control on both trends and interannual variability (IAV) of NEE (Jung et al., 2017; Ahlström et al., 2015). In contrast, boreal and temperate forest ecosystems are primarily temperature-limited. These regions have shown earlier spring carbon uptake and longer growing seasons in response to warming (Keenan et al., 2014; Gu et al., 2022). However, long-term eddy-covariance records (spanning more than a decade) remain sparse in Arctic and boreal regions (Pallandt et al., 2024), which limits the ability to systematically evaluate biome-scale changes in CUP dynamics at high latitudes.

The flux data products used in this study, namely NEE from global atmospheric inversions are optimized for continental to large regional scales. While these systems robustly capture large-scale gradients, their effective resolution is limited by transport smoothing and prior error structures, which reduce sensitivity to smaller or spatially heterogeneous biomes. Although FLUXCOM products provide finer spatial resolution, their performance depends on the representativeness of flux-tower training data and the quality of meteorological and remote-sensing drivers (Jung et al., 2020). Further, machine-learning-based upscaling can underestimate interannual variability in NEE, particularly in regions with sparse tower coverage or strong climate extremes (Nelson et al., 2024). High-latitude Eurasia and boreal North America remain especially uncertain in this respect, as relationships learned in mid-latitude regions must be extrapolated into

under-sampled ecosystems (Nelson et al., 2024). Similarly, global inversion systems have an effective flux resolution determined by their prior flux structure and the density of the observational network. Peylin et al. (2013) emphasize that the spatial scale at which fluxes are optimized should be considered relative to the region being analysed. Recent intercomparison of global inversions further demonstrates substantial disagreement in regional carbon flux estimates despite relatively consistent global totals (van der Woude et al., 2025b; Gaubert et al., 2019).

Future work could address this limitation by integrating higher-resolution regional inversion systems. Regional frameworks, such as those developed within the EUROCOM intercomparison (Monteil et al., 2020), operate at finer spatial scales and exploit denser observation networks, thereby improving sub-continental flux attribution. When combined with biome masks or plant functional type classifications, such inversions could enable a more direct assessment of biome-specific CUP trends.

While this thesis demonstrates that atmospheric CO_2 observations can provide robust information on large-scale changes in the timing of the terrestrial carbon uptake period, several limitations remain. The most robust result emerging from this work is the detection of coherent shifts in CUP_{MR} timing at high-latitude sites, particularly the advancing onset signal that appears consistently across stations and across independent datasets. However, the magnitude of these changes and their regional attribution remain more uncertain. Atmospheric transport redistributes and smooths surface flux signals before they reach monitoring sites, meaning that atmospheric records represent an integrated signal from broad source regions rather than local ecosystem changes. In addition, the existing sparse spatial coverage of atmospheric monitoring networks limits their ability to diagnose CUP dynamics at finer regional scales. Recent developments offer promising pathways to address these limitations, including the continued expansion of atmospheric monitoring networks such as ICOS and the growth of FLUXNET sites that enable analysis of CUP dynamics at finer spatial scales. The integration of additional atmospheric tracers, such as $\delta^{13}C$ and carbonyl sulfide (COS), may further help disentangle photosynthetic and respiratory contributions to seasonal carbon fluxes. Combining these emerging data streams with the uncertainty-aware CUP framework developed in this thesis could enable more robust attribution of seasonal carbon-cycle changes and improve our ability to diagnose ecosystem responses to climate variability and extreme events. The following section discusses such future research directions in detail.

5.2 Outlook

In addition to the potential future studies suggested in the preceding sections, several additional research directions emerge from this work. This thesis has primarily focused on the seasonal cycle of atmospheric CO_2 to investigate the timing of the CUP. However, the same analytical framework could be extended to other trace gases and isotopic tracers. A particularly promising extension involves the use of the stable isotope ratio $^{13}C/^{12}C$ in atmospheric CO_2 (reported as $\delta^{13}C$) as a complementary diagnostic of the carbon cycle. Plants preferentially assimilate ^{12}C over ^{13}C, and the degree of this discrimination depends on their photosynthetic pathway (C_3 vs. C_4 plants) as well as environmental conditions (Peters et al., 2018; Farquhar et al., 1982; Keeling, 1960). As a result, seasonal variations in atmospheric $\delta^{13}C$ are closely coupled to biospheric activity. During the growing season, when terrestrial photosynthesis dominates, ecosystems preferentially remove ^{12}C, leading to a relative enrichment of ^{13}C in the atmosphere. In contrast, during autumn and winter, the release of ^{12}C-enriched CO_2 through respiration produces an inverse seasonal relationship between CO_2 and $\delta^{13}C$ (Keeling et al., 2017; Peters et al., 2018; Wehr & Saleska, 2015). A joint analysis of CO_2 and $\delta^{13}C$ seasonal phase and amplitude within isotope-enabled transport frameworks could thus provide an additional consistency check on the large-scale biospheric origin of observed CUP shifts. Previous studies such as Gonsamo et al. (2017) have examined how changes in vegetation productivity and phenology, respiration, and air temperature affect both atmospheric CO_2 and $^{13}C/^{12}C$ seasonality. Including isotopic observations alongside CO_2 measurements would allow a direct comparison of trends and interannual covariation in CUP_{MR} derived from CO_2 with corresponding seasonal transition metrics in atmospheric $\delta^{13}C$ at the same stations. This would enable evaluation of whether shifts in the CO_2-derived CUP onset are accompanied by coherent changes in the timing or rate of seasonal $\delta^{13}C$ enrichment. For example, if an earlier CUP_{MR} onset is primarily driven by earlier activation of photosynthesis, a corresponding earlier onset or steeper spring increase in $\delta^{13}C$ would be expected, reflecting enhanced preferential removal of ^{12}C. In years when parallel changes in photosynthesis and respiration, occur, the atmospheric isotopic seasonality would be stabilized despite phenological advances (Gonsamo et al., 2017).

Further, the EFD method could be extended beyond the analysis of the CUP to identify other inflection points in the atmospheric CO_2 seasonal cycle. While considerable attention has been devoted to detecting changes in the onset and duration of the growing-season carbon uptake period, comparatively less emphasis has been placed on the systematic quantification of the carbon release period (CRP, the part of the year when respiration exceeds photosynthetic uptake) and its temporal evolution. This represents an important knowledge gap, particularly at high latitudes where winter warming is strongest (Gharun et al., 2025). A recent study by Tran et al. (2024)

demonstrated this potential by applying an adapted version of the EFD method to the CO_2 time series measured at the Zotino Tall Tower Observatory (ZOTTO) in central Siberia. They optimized the derivative-based threshold to 30% of the first derivative minimum to accommodate the broad and flattened CO_2 peaks typical of the ZOTTO record. Using this adjustment, they studied the onset and termination of the CRP and found a significant delay in the CRP termination over the 11-year analysis period. Their results show that the duration of the CRP has increased and suggests enhanced CO_2 release during the cold season. Warmer winters enhance microbial activity in soils, increasing CO_2 efflux (Commane et al., 2017), extending the EFD analysis to the CRP would thus provide a robust way to quantify how respiratory flux timing and intensity evolve alongside the growing-season uptake. Building on the work presented in this thesis, the EFD framework could be systematically applied to CRP detection across a broader network of observation sites and over longer time periods. The analyses could be extended to the evaluation of spatial patterns and temporal trends in the CRP, including how they respond to atmospheric transport processes and regional climatic drivers. Comparing the sensitivities of both CUP and CRP would help establish a more complete picture of the CO_2 seasonal cycle and its changing dynamics under warming conditions.

Future studies could extend the framework presented in this thesis to explicitly investigate short-term anomalies associated with extreme climate events. Applying the EFD-based diagnostics to individual event years would allow for quantification of how, for example, heatwaves, fires, droughts, or anomalous wet periods alter the timing, duration, and asymmetry of the carbon uptake and release periods. Such analyses could address several open questions: whether extreme drought delays CUP onset or primarily suppresses uptake intensity, and whether heat stress leads to earlier termination of the uptake period and extension of the release phase. Coupling atmospheric CO_2 records with complementary tracers would provide additional process-level insight, allowing anomalies driven primarily by changes in photosynthesis, respiration, or altered atmospheric transport to be separated, as discussed above. A similar atmospheric perspective was employed by Ramonet et al. (2020), who analyzed CO_2 records from the ICOS European network to identify the large-scale atmospheric fingerprint of the 2018 European drought. Their results showed a substantial reduction in summer carbon uptake and an earlier return to net release conditions, revealing a clear atmospheric signal of drought-induced weakening of the terrestrial carbon sink. Although their study focused mainly on the amplitude of the CO_2 seasonal cycle, a similar methodology could be extended to investigate changes in CUP timing during such events, providing additional insight into how ecosystem transitions respond to climate extremes. For example, atmospheric CO_2 mole fraction observations from the ZOTTO tall tower in central Siberia revealed anomalously early onset of carbon uptake during the 2020 heatwave (Tran et al., 2024). By analyzing event-specific atmospheric anomalies in conjunction with inversion-based flux estimates and isotopic tracers, researchers could evaluate the effects of climate

extremes on the timing and duration of net carbon uptake.

In summary, the methodological advances developed in this thesis provide a transferable framework for diagnosing seasonal carbon dynamics from atmospheric observations. Extending the EFD approach to the joint analysis of carbon uptake and release periods, to event-scale anomalies, and potentially to additional trace gases could improve the quantification of shifts in seasonal timing, duration, and intensity and drivers of seasonal carbon exchange. These seasonal diagnostics can support the evaluation of process-based models and atmospheric inversion systems and, when combined with complementary observational constraints, contribute to reducing uncertainties in regional and global carbon budget estimates.

References

Ahlström, A., Raupach, M. R., Schurgers, G., Smith, B., Arneth, A., Jung, M., Reichstein, M., Canadell, J. G., Friedlingstein, P., Jain, A. K. et al. (2015). The dominant role of semi-arid ecosystems in the trend and variability of the land CO_2 sink. *Science*, *348*, 895–899. doi:10.1126/science.aaa1668.

Anav, A., Friedlingstein, P., Beer, C., Ciais, P., Harper, A., Jones, C., Murray-Tortarolo, G., Papale, D., Parazoo, N. C., Peylin, P. et al. (2015). Spatiotemporal patterns of terrestrial gross primary production: A review. *Reviews of Geophysics*, *53*, 785–818. doi:10.1002/2015RG000483.

Angert, A., Biraud, S., Bonfils, C., Henning, C., Buermann, W., Pinzon, J., Tucker, C., & Fung, I. (2005). Drier summers cancel out the CO_2 uptake enhancement induced by warmer springs. *Proceedings of the National Academy of Sciences*, *102*, 10823–10827. doi:10.1073/pnas.0501647102.

Archer, D., Eby, M., Brovkin, V., Ridgwell, A., Cao, L., Mikolajewicz, U., Caldeira, K., Matsumoto, K., Munhoven, G., Montenegro, A. et al. (2009). Atmospheric lifetime of fossil fuel carbon dioxide. *Annual review of earth and planetary sciences*, *37*, 117–134. doi:10.1146/annurev.earth.031208.100206.

Bacastow, R., Keeling, C., & Whorf, T. (1985). Seasonal amplitude increase in atmospheric CO_2 concentration at Mauna Loa, Hawaii, 1959–1982. *Journal of Geophysical Research: Atmospheres*, *90*, 10529–10540. doi:10.1029/JD090iD06p10529.

Baker, D., Law, R. M., Gurney, K. R., Rayner, P., Peylin, P., Denning, A., Bousquet, P., Bruhwiler, L., Chen, Y.-H., Ciais, P. et al. (2006). TransCom 3 inversion intercomparison: Impact of transport model errors on the interannual variability of regional CO_2 fluxes, 1988–2003. *Global Biogeochemical Cycles*, *20*. doi:10.1029/2004GB002439.

Baldocchi, D., Chu, H., & Reichstein, M. (2018). Inter-annual variability of net and gross ecosystem carbon fluxes: A review. *Agricultural and Forest Meteorology*, *249*, 520–533. doi:10.1016/j.agrformet.2017.05.015.

Baldocchi, D. et al. (2001). Fluxnet: A new tool to study the temporal and spatial variability of ecosystem–scale carbon dioxide, water vapor, and energy flux densities. *Bulletin of the American Meteorological Society*, *82*, 2415–2434. doi:10.1175/1520-

0477(2001)082¡2415:fantts¿2.3.co;2.

Barichivich, J., Briffa, K., Osborn, T., Melvin, T., & Caesar, J. (2012). Thermal growing season and timing of biospheric carbon uptake across the northern hemisphere. *Global Biogeochemical Cycles*, *26*, 4015–. doi:10.1029/2012GB004312.

Barichivich, J., Briffa, K. R., Myneni, R. B., Osborn, T. J., Melvin, T. M., Ciais, P., Piao, S., & Tucker, C. (2013). Large-scale variations in the vegetation growing season and annual cycle of atmospheric co$_2$ at high northern latitudes from 1950 to 2011. *Glob Chang Biol*, *19*, 3167–83. doi:10.1111/gcb.12283.

Barlow, J. M., Palmer, P. I., & Bruhwiler, L. M. (2016). Increasing boreal wetland emissions inferred from reductions in atmospheric ch$_4$ seasonal cycle. *Atmospheric Chemistry and Physics Discussions*, *2016*, 1–38. doi:10.5194/acp-2016-752.

Barlow, J. M., Palmer, P. I., Bruhwiler, L. M., & Tans, P. (2015). Analysis of CO_2 mole fraction data: first evidence of large-scale changes in CO_2 uptake at high northern latitudes. *Atmospheric Chemistry and Physics*, (pp. 13739–13758). doi:10.5194/acp-15-13739-2015.

Barnes, E. A., Parazoo, N., Orbe, C., & Denning, A. S. (2016). Isentropic transport and the seasonal cycle amplitude of CO_2. *Journal of Geophysical Research: Atmospheres*, *121*, 8106–8124. doi:10.1002/2016JD025109.

Barnett, T. P., Adam, J. C., & Lettenmaier, D. P. (2005). Potential impacts of a warming climate on water availability in snow-dominated regions. *Nature*, *438*, 303–309. doi:10.1038/nature04141.

Beer, C. et al. (2010). Terrestrial gross carbon dioxide uptake: global distribution and covariation with climate. *Science*, *329*, 834–838. doi:10.1126/science.1184984. Epub 2010 Jul 5.

Bi, J., Xu, L., Samanta, A., Zhu, Z., & Myneni, R. (2013). Divergent arctic-boreal vegetation changes between north america and eurasia over the past 30 years. *Remote Sensing*, *5*, 2093–2112. doi:10.3390/rs5052093.

Black, T., Chen, W., Barr, A., Arain, M., Chen, Z., Nesic, Z., Hogg, E., Neumann, H., & Yang, P. (2000). Increased carbon sequestration by a boreal deciduous forest in years with a warm spring. *Geophysical Research Letters*, *27*, 1271–1274. doi:10.1029/1999GL011234.

Bond-Lamberty, B., Bailey, V. L., Chen, M., Gough, C. M., & Vargas, R. (2018). Globally rising soil heterotrophic respiration over recent decades. *Nature*, *560*, 80–83. doi:10.1038/s41586-018-0358-x.

Buermann, W., Forkel, M., O'sullivan, M., Sitch, S., Friedlingstein, P., Haverd, V., Jain, A. K., Kato, E., Kautz, M., Lienert, S. et al. (2018). Widespread seasonal compensation effects of spring warming on northern plant productivity. *Nature*, *562*, 110–114.

doi:10.1038/s41586-018-0555-7.

Byrne, B. et al. (2020). Improved Constraints on Northern Extratropical CO_2 Fluxes Obtained by Combining Surface-Based and Space-Based Atmospheric CO_2 Measurements. *Journal of Geophysical Research: Atmospheres*, *125*, e2019JD032029. doi:10.1029/2019JD032029.

Chan, Y. H., & Wong, C. S. (1990). Long-term changes in amplitudes of atmospheric CO_2 concentrations at Ocean Station P and Alert, Canada. *Tellus B*, *42*, 330–341. doi:10.1034/j.1600-0889.1990.t01-4-00003.x.

Chen, C., Riley, W. J., Prentice, I. C., & Keenan, T. F. (2022). CO_2 fertilization of terrestrial photosynthesis inferred from site to global scales. *Proceedings of the National Academy of Sciences*, *119*, e2115627119. doi:10.1073/pnas.2115627119.

Chen, H., Zhao, J., Zhang, H., Zhang, Z., Guo, X., & Wang, M. (2023). Detection and attribution of the start of the growing season changes in the Northern Hemisphere. *Science of the Total Environment*, *903*, 166607. doi:10.1016/j.scitotenv.2023.166607.

Chen, Z. et al. (2021). Linking global terrestrial CO_2 fluxes and environmental drivers: inferences from the Orbiting Carbon Observatory 2 satellite and terrestrial biospheric models. *Atmospheric Chemistry and Physics*, *21*, 6663–6680. doi:10.5194/acp-21-6663-2021.

Churkina, G., Schimel, D., Braswell, B. H., & Xiao, X. (2005). Spatial analysis of growing season length control over net ecosystem exchange. *Global Change Biology*, *11*, 1777–1787. doi:10.1111/j.1365-2486.2005.001012.x.

Ciais, P., Bastos, A., Chevallier, F., Lauerwald, R., Poulter, B., Canadell, P., Hugelius, G., Jackson, R. B., Jain, A., Jones, M. et al. (2020). Definitions and methods to estimate regional land carbon fluxes for the second phase of the REgional Carbon Cycle Assessment and Processes Project (RECCAP-2). *Geoscientific Model Development Discussions*, *2020*, 1–46. doi:10.5194/gmd-15-1289-2022.

Ciais, P., Reichstein, M., Viovy, N., Granier, A., Ogée, J., Allard, V., Aubinet, M., Buchmann, N., Bernhofer, C., Carrara, A. et al. (2005). Europe-wide reduction in primary productivity caused by the heat and drought in 2003. *Nature*, *437*, 529–533. doi:10.1038/nature03972.

Ciais, P., Sabine, C., Bala, G., Bopp, L., Brovkin, V., Canadell, J., Chhabra, A., DeFries, R., Galloway, J., Heimann, M. et al. (2013). Carbon and other biogeochemical cycles. Climate change 2013: the physical science basis. Contribution of Working Group I to the Fifth Assessment Report of the Intergovernmental Panel on Climate Change.

Ciais, P. et al. (2019). Five decades of northern land carbon uptake revealed by the interhemispheric co_2 gradient. *Nature*, *568*, 221–225. doi:10.1038/s41586-019-1078-6.

Ciais, P., Yao, Y., Gasser, T., Baccini, A., Wang, Y., Lauerwald, R., Peng, S., Bastos,

A., Li, W., Raymond, P. A. et al. (2021). Empirical estimates of regional carbon budgets imply reduced global soil heterotrophic respiration. *National Science Review*, *8*, nwaa145. doi:10.1093/nsr/nwaa145.

Cleveland, R. B., Cleveland, W. S., McRae, J. E., & Terpenning, I. (1990). STL: A Seasonal-Trend Decomposition Procedure Based on Loess (with Discussion). *Journal of Official Statistics*, *6*, 3–73.

Commane, R. et al. (2017). Carbon dioxide sources from alaska driven by increasing early winter respiration from arctic tundra. *Proceedings of the National Academy of Sciences*, *114*, 5361–5366. doi:10.1073/pnas.1618567114.

Copernicus Climate Change Service (C3S) (2023). ERA5 monthly averaged data on single levels from 1940 to present. doi:10.24381/cds.f17050d7 accessed: 27-12-2025.

Deng, G., Zhang, H., Guo, X., Shan, Y., Ying, H., Rihan, W., Li, H., & Han, Y. (2019). Asymmetric effects of daytime and nighttime warming on boreal forest spring phenology. *Remote Sensing*, *11*, 1651. doi:10.3390/rs11141651.

Ding, X., Chen, G., Wang, Y., & Sun, L. (2025). Demystifying the drivers of the spring warming asymmetry between Eurasia and North America. *Science Advances*, *11*, eadu2364. doi:10.1126/sciadv.adu2364.

Dlugokencky, E., Mund, J. W., Crotwell, M. J., A. M. andCrotwell, & Thoning, K. W. (2019). Atmospheric Carbon Dioxide Dry Air Mole Fractions from the NOAA GML Carbon Cycle Cooperative Global Air Sampling Network, 1968-2018, Version: 2019-07. doi:10.15138/wkgj-f215.

Dlugokencky, E., Mund, J. W., Crotwell, M. J., A. M. andCrotwell, & Thoning, K. W. (2020). Atmospheric Carbon Dioxide Dry Air Mole Fractions from the NOAA GML Carbon Cycle Cooperative Global Air Sampling Network, 1968-2019, Version: 2020-07. doi:10.15138/wkgj-f215.

Dragoni, D., Schmid, H. P., Wayson, C. A., Potter, H., Grimmond, C. S. B., & Randolph, J. C. (2011). Evidence of increased net ecosystem productivity associated with a longer vegetated season in a deciduous forest in south-central Indiana, USA. *Global Change Biology*, *17*, 886–897. doi:10.1111/j.1365-2486.2010.02281.x.

Endsley, K. A., Kimball, J. S., & Reichle, R. H. (2022). Soil respiration phenology improves modeled phase of terrestrial net ecosystem exchange in Northern Hemisphere. *Journal of Advances in Modeling Earth Systems*, *14*, e2021MS002804. doi:10.1029/2021MS002804.

Enting, I. G., Rayner, P. J., & Ciais, P. (2012). Carbon Cycle Uncertainty in REgional Carbon Cycle Assessment and Processes (RECCAP). *Biogeosciences*, *9*, 2889–2904. doi:10.5194/bg-9-2889-2012.

Fang, Z., Brandt, M., Wang, L., & Fensholt, R. (2022). A global increase in tree cover

extends the growing season length as observed from satellite records. *Science of the Total Environment*, *806*, 151205. doi:10.1016/j.scitotenv.2021.151205.

Farquhar, G., O'Leary, M., & Berry, J. (1982). On the relationship between carbon isotope discrimination and the intercellular carbon dioxide concentration in leaves. *Australian journal of plant physiology*, *9*, 121–137.

Farquhar, G. D., & Roderick, M. L. (2003). Pinatubo, diffuse light, and the carbon cycle. *Science*, *299*, 1997–1998. doi:10.1126/science.1080681.

Flato, G. et al. (2013). Evaluation of Climate Models. In: Climate Change 2013: The Physical Science Basis. Contribution of Working Group I to the Fifth Assessment Report of the Intergovernmental Panel on Climate Change. Cambridge University Press. doi:10.1017/CBO9781107415324.020.

Forkel, M., Carvalhais, N., Rödenbeck, C., Keeling, R., Heimann, M., Thonicke, K., Zaehle, S., & Reichstein, M. (2016). Enhanced seasonal CO_2 exchange caused by amplified plant productivity in northern ecosystems. *Science*, *351*, 696–699. doi:10.1126/science.aac4971.

Forster, P., Storelvmo, T., Armour, K., Collins, W., Dufresne, J.-L., Frame, D., Lunt, D. J., Mauritsen, T., Palmer, M. D., Watanabe, M., Wild, M., & Zhang, H. (2021). The earth's energy budget, climate feedbacks, and climate sensitivity. In V. Masson-Delmotte, P. Zhai, A. Pirani, S. L. Connors, C. Péan, S. Berger, N. Caud, Y. Chen, L. Goldfarb, M. I. Gomis, M. Huang, K. Leitzell, E. Lonnoy, J. B. R. Matthews, T. K. Maycock, T. Waterfield, O. Yelekçi, R. Yu, & B. Zhou (Eds.), *Climate Change 2021: The Physical Science Basis* (pp. 923–1054). Cambridge, United Kingdom and New York, NY, USA: Cambridge University Press. doi:10.1017/9781009157896.009.

Friedlingstein, P. et al. (2019). Global Carbon Budget 2019. *Earth System Science Data*, *11*, 1783–1838. doi:10.5194/essd-11-1783-2019.

Friedlingstein, P. et al. (2025). Global carbon budget 2024. *Earth System Science Data*, *17*, 965–1039. doi:10.5194/essd-17-965-2025.

Fu, Q., Lin, P., Solomon, S., & Hartmann, D. L. (2015). Observational evidence of strengthening of the Brewer-Dobson circulation since 1980. *Journal of Geophysical Research: Atmospheres*, *120*, 10,214–10,228. doi:10.1002/2015JD023657.

Fu, Z. et al. (2017). Climate controls over the net carbon uptake period and amplitude of net ecosystem production in temperate and boreal ecosystems. *Agricultural and Forest Meteorology*, *243*, 9–18. doi:10.1016/j.agrformet.2017.05.009.

Fu, Z., Stoy, P. C., Poulter, B., Gerken, T., Zhang, Z., Wakbulcho, G., & Niu, S. (2019). Maximum carbon uptake rate dominates the interannual variability of global net ecosystem exchange. *Global Change Biology*, *25*, 3381–3394. doi:10.1111/gcb.14731.

Garonna, I., de Jong, R., & Schaepman, M. E. (2016). Variability and evolution of global

land surface phenology over the past three decades (1982–2012). *Global change biology*, *22*, 1456–1468. doi:10.1111/gcb.13168.

Gaubert, B. et al. (2019). Global atmospheric CO_2 inverse models converging on neutral tropical land exchange, but disagreeing on fossil fuel and atmospheric growth rate. *Biogeosciences*, *16*, 117–134. doi:10.5194/bg-16-117-2019.

Gharun, M., Shekhar, A., Hörtnagl, L., Krebs, L., Arriga, N., Migliavacca, M., Roland, M., Gielen, B., Montagnani, L., Tomelleri, E. et al. (2025). Impact of winter warming on CO_2 fluxes in evergreen needleleaf forests. *Biogeosciences*, *22*, 1393–1411. doi:10.5194/bg-22-1393-2025.

Gill, A. L., Gallinat, A. S., Sanders-DeMott, R., Rigden, A. J., Short Gianotti, D. J., Mantooth, J. A., & Templer, P. H. (2015). Changes in autumn senescence in northern hemisphere deciduous trees: a meta-analysis of autumn phenology studies. *Annals of Botany*, *116*, 875–888. doi:10.1093/aob/mcv055.

Gonsamo, A., Chen, J. M., Wu, C., & Dragoni, D. (2012). Predicting deciduous forest carbon uptake phenology by upscaling FLUXNET measurements using remote sensing data. *Agricultural and Forest Meteorology*, *165*, 127–135. doi:10.1016/j.agrformet.2012.06.006.

Gonsamo, A., D'Odorico, P., Chen, J. M., Wu, C., & Buchmann, N. (2017). Changes in vegetation phenology are not reflected in atmospheric CO_2 and $^{13}C/^{12}C$ seasonality. *Global Change Biology*, *23*, 4029–4044. doi:10.1111/gcb.13646.

Goulden, M. L., Munger, J. W., Fan, S.-M., Daube, B. C., & Wofsy, S. C. (1996). Exchange of carbon dioxide by a deciduous forest: response to interannual climate variability. *Science*, *271*, 1576–1578. doi:10.1126/science.271.5255.1576.

Graven, H. D. et al. (2013). Enhanced seasonal exchange of co_2 by northern ecosystems since 1960. *Science*, *341*, 1085–9. doi:10.1126/science.1239207.

Gu, H., Qiao, Y., Xi, Z., Rossi, S., Smith, N. G., Liu, J., & Chen, L. (2022). Warming-induced increase in carbon uptake is linked to earlier spring phenology in temperate and boreal forests. *Nature Communications*, *13*, 3698. doi:10.1038/s41467-022-31496-w.

Gulev, S. K., Thorne, P. W., Ahn, J., Dentener, F. J., Domingues, C. M., Gerland, S., Gong, D., Kaufman, D. S., Nnamchi, H. C., Quaas, J. et al. (2021). Changing state of the climate system. Climate Change 2021 – The Physical Science Basis: Working Group I Contribution to the Sixth Assessment Report of the Intergovernmental Panel on Climate Change (pp. 287–422). Cambridge: Cambridge University Press. doi:10.1017/9781009157896.004.

Gurney, K. R. et al. (2002). Towards robust regional estimates of CO_2 sources and sinks using atmospheric transport models. *Nature*, *415*, 626–630. doi:10.1038/415626a.

Hanes, C. C., Wang, X., Jain, P., Parisien, M.-A., Little, J. M., & Flannigan, M. D.

(2019). Fire-regime changes in Canada over the last half century. *Canadian Journal of Forest Research*, *49*, 256–269. doi:10.1139/cjfr-2018-0293.

Heimann, H., & Körner, S. (2003). The global atmospheric tracer model TM3. *Technical Reports - Max-Planck-Institut für Biogeochemie 5*, *5*, 131. doi:10.4126/98-004424387.

Hersbach, H. et al. (2020). The ERA5 global reanalysis. *Quarterly Journal of the Royal Meteorological Society*, *146*. doi:10.1002/qj.3803.

Higuchi, K., Murayama, S., & Taguchi, S. (2002). Quasi-decadal variation of the atmospheric CO_2 seasonal cycle due to atmospheric circulation changes: 1979–1998. *Geophysical Research Letters - GEOPHYS RES LETT*, *29*. doi:10.1029/2001GL013751.

Hu, J., Moore, D. J., Burns, S. P., & Monson, R. K. (2010). Longer growing seasons lead to less carbon sequestration by a subalpine forest. *Global Change Biology*, *16*, 771–783. doi:10.1111/j.1365-2486.2009.01967.x.

Huntzinger, D., Michalak, A., Schwalm, C., Ciais, P., King, A., Fang, Y., Schaefer, K., Wei, Y., Cook, R., Fisher, J. et al. (2017). Uncertainty in the response of terrestrial carbon sink to environmental drivers undermines carbon-climate feedback predictions. *Scientific reports*, *7*, 4765. doi:10.1038/s41598-017-03818-2.

Jeong, S.-J., Ho, C.-H., Gim, H.-J., & Brown, M. E. (2011). Phenology shifts at start vs. end of growing season in temperate vegetation over the northern hemisphere for the period 1982–2008. *Global Change Biology*, *17*, 2385–2399. doi:10.1111/j.1365-2486.2011.02397.x.

Jeong, S.-J., & Medvigy, D. (2014). Macroscale prediction of autumn leaf coloration throughout the continental United States. *Global Ecology and Biogeography*, *23*, 1245–1254. doi:10.1111/geb.12206.

Jeong, S.-J., Medvigy, D., Shevliakova, E., & Malyshev, S. (2012). Uncertainties in terrestrial carbon budgets related to spring phenology. *Journal of Geophysical Research: Biogeosciences*, *117*. doi:10.1029/2011JG001868.

Jin, Y., Keeling, R. F., Rödenbeck, C., Patra, P. K., Piper, S. C., & Schwartzman, A. (2022). Impact of Changing Winds on the Mauna Loa CO_2 Seasonal Cycle in Relation to the Pacific Decadal Oscillation. *Journal of Geophysical Research: Atmospheres*, *127*, e2021JD035892. doi:10.1029/2021JD035892.

Jung, M., Reichstein, M., Margolis, H. A., Cescatti, A., Richardson, A. D., Arain, M. A., Arneth, A., Bernhofer, C., Bonal, D., Chen, J. et al. (2011). Global patterns of land-atmosphere fluxes of carbon dioxide, latent heat, and sensible heat derived from eddy covariance, satellite, and meteorological observations. *Journal of Geophysical Research: Biogeosciences*, *116*. doi:10.1029/2010JG001566.

Jung, M. et al. (2017). Compensatory water effects link yearly global land CO_2 sink changes to temperature. *Nature*, *541*, 516–520. doi:10.1038/nature20780.

Jung, M., Schwalm, C., Migliavacca, M., Walther, S., Camps-Valls, G., Koirala, S., Anthoni, P., Besnard, S., Bodesheim, P., Carvalhais, N. et al. (2020). Scaling carbon fluxes from eddy covariance sites to globe: synthesis and evaluation of the FLUXCOM approach. *Biogeosciences*, *17*, 1343–1365. doi:10.5194/bg-17-1343-2020.

Kariyathan, T., Bastos, A., Marshall, J., Peters, W., Tans, P., & Reichstein, M. (2023). Reducing errors on estimates of the carbon uptake period based on time series of atmospheric CO_2. *Atmospheric Measurement Techniques*, *16*, 3299–3312. doi:10.5194/amt-16-3299-2023.

Kariyathan, T., Bastos, A., Reichstein, M., Peters, W., & Marshall, J. (2025). Limitations in the use of atmospheric CO_2 observations to directly infer changes in the length of the biospheric carbon uptake period. *Atmospheric Chemistry and Physics*, *25*, 7863–7878. doi:10.5194/acp-25-7863-2025.

Kariyathan, T., Marshall, J., Bastos, A., Reichstein, M., & Peters, W. (). Advancing onset of the carbon uptake period: evidence from high-latitude CO_2 records driven by eurasian ecosystem shifts. *(In prep.)*, .

Kasischke, E. S. (2000). Boreal ecosystems in the global carbon cycle. In E. S. Kasischke, & B. J. Stocks (Eds.), *Fire, Climate Change, and Carbon Cycling in the Boreal Forest* (pp. 19–30). New York, NY: Springer. doi:10.1007/978-0-387-21629-4_2.

Ke, P. et al. (2024). Low latency carbon budget analysis reveals a large decline of the land carbon sink in 2023. *National Science Review*, *11*, nwae367. doi:10.1093/nsr/nwae367.

Keeling, C. D. (1960). The concentration and isotopic abundances of carbon dioxide in the atmosphere. *Tellus*, *12*, 200–203. doi:10.1111/j.2153-3490.1960.tb01300.x.

Keeling, C. D., Chin, J., & Whorf, T. (1996). Increased activity of northern vegetation inferred from atmospheric CO_2 measurements. *Nature*, *382*, 146–149. doi:10.1038/382146a0.

Keeling, R. F., Graven, H. D., Welp, L. R., Resplandy, L., Bi, J., Piper, S. C., Sun, Y., Bollenbacher, A., & Meijer, H. A. J. (2017). Atmospheric evidence for a global secular increase in carbon isotopic discrimination of land photosynthesis. *Proceedings of the National Academy of Sciences*, *114*, 10361–10366. doi:10.1073/pnas.1619240114.

Keenan, T. F., Gray, J., Friedl, M. A., Toomey, M., Bohrer, G., Hollinger, D. Y., Munger, J. W., O'Keefe, J., Schmid, H. P., Wing, I. S. et al. (2014). Net carbon uptake has increased through warming-induced changes in temperate forest phenology. *Nature Climate Change*, *4*, 598–604. doi:10.1038/nclimate2253.

Kou-Giesbrecht, S., Arora, V. K., Jones, C. D., Brovkin, V., Hajima, T., Kawamiya, M., Liddicoat, S. K., Winkler, A. J., & Zaehle, S. (2025). Rising nitrogen deposition leads to only a minor increase in CO_2 uptake in Earth system models. *Communications Earth & Environment*, *6*, 216. doi:10.1038/s43247-024-01943-1.

Kreiss, J.-P., & Lahiri, S. N. (2012). 1 - Bootstrap Methods for Time Series. In T. Subba Rao, S. Subba Rao, & C. Rao (Eds.), *Time Series Analysis: Methods and Applications* (pp. 3–26). Elsevier volume 30 of *Handbook of Statistics*. doi:10.1016/B978-0-444-53858-1.00001-6.

Krol, M. et al. (2018). Age of air as a diagnostic for transport timescales in global models. *Geoscientific Model Development*, *11*, 3109–3130. doi:10.5194/gmd-11-3109-2018.

Krol, M., Houweling, S., Bregman, B., Van den Broek, M., Segers, A., Van Velthoven, P., Peters, W., Dentener, F., & Bergamaschi, P. (2005). The two-way nested global chemistry-transport zoom model TM5: algorithm and applications. *Atmospheric Chemistry and Physics*, *5*, 417–432. doi:10.5194/acp-5-417-2005.

Kuhn, M. (2020). *caret: Classification and Regression Training*. doi:10.32614/CRAN.package.caret r package version 6.0-85.

van der Laan-Luijkx, I. T. et al. (2017). The CarbonTracker Data Assimilation Shell (CTDAS) v1.0: implementation and global carbon balance 2001–2015. *Geoscientific Model Development*, *10*, 2785–2800. doi:10.5194/gmd-10-2785-2017.

Lai, J., Kooijmans, L. M. J., Sun, W., Lombardozzi, D., Campbell, J. E., Gu, L., Luo, Y., Kuai, L., & Sun, Y. (2024). Terrestrial photosynthesis inferred from plant carbonyl sulfide uptake. *Nature (London)*, *634*. doi:10.1038/s41586-024-08050-3.

Lan, X., Tans, P., & Thoning, K. W. (2026). Trends in globally-averaged CO_2 determined from NOAA Global Monitoring Laboratory measurements. doi:10.15138/9N0H-ZH07.

Langenfelds, R. L., Francey, R. J., Pak, B. C., Steele, L. P., Lloyd, J., Trudinger, C. M., & Allison, C. E. (2002). Interannual growth rate variations of atmospheric CO_2 and its $\delta^{13}C$, H_2, CH_4, and CO between 1992 and 1999 linked to biomass burning. *Global Biogeochemical Cycles*, *16*, 21–1–21–22. doi:10.1029/2001GB001466.

Li, N., Sippel, S., Winkler, A. J., Mahecha, M. D., Reichstein, M., & Bastos, A. (2022). Interannual global carbon cycle variations linked to atmospheric circulation variability. *Earth System Dynamics*, *13*, 1505–1533. doi:10.5194/esd-13-1505-2022.

Li, W.-P., Zhang, Y.-W., Mu, M., Shi, X.-L., Zhou, W.-Y., & Ji, J.-J. (2023). Spatial and temporal variations of gross primary production simulated by land surface model BCC_AVIM2.0. *Advances in Climate Change Research*, *14*, 286–299. doi:10.1016/j.accre.2023.02.001.

Lian, X., Piao, S., Li, L. Z., Li, Y., Huntingford, C., Ciais, P., Cescatti, A., Janssens, I. A., Peñuelas, J., Buermann, W. et al. (2020). Summer soil drying exacerbated by earlier spring greening of northern vegetation. *Science advances*, *6*, eaax0255. doi:10.1126/sciadv.aax0255.

Linderholm, H. W. (2006). Growing season changes in the last century. *Agricultural and Forest Meteorology*, *137*, 1–14. doi:10.1016/j.agrformet.2006.03.006.

Lindsey, R. (2025). Climate change: atmospheric carbon dioxide. https://www.climate.gov/news-features/understanding-climate/climate-change-atmospheric-carbon-dioxide. NOAA Climate.gov, last access: 23 March 2026.

Lintner, B. R., Buermann, W., Koven, C. D., & Fung, I. Y. (2006). Seasonal circulation and Mauna Loa CO_2 variability. *Journal of Geophysical Research: Atmospheres*, *111*. doi:10.1029/2005JD006535.

Liu, M., Yu, H., Duan, W., & Wu, M. (2025a). Differential impacts of compound dry- and humid-hot events on global vegetation productivity. *Frontiers in Environmental Science*, *Volume 13 - 2025*. doi:10.3389/fenvs.2025.1597553.

Liu, Y., Piao, S., Lian, X., Ciais, P., & Smith, W. K. (2017). Seasonal Responses of Terrestrial Carbon Cycle to Climate Variations in CMIP5 Models: Evaluation and Projection. *Journal of Climate*, *30*, 6481 – 6503. doi:10.1175/JCLI-D-16-0555.1.

Liu, Z., Ciais, P., Peñuelas, J., Xia, J., Zhou, S., Zhang, Y., & Fu, Y. H. (2025b). Enhanced vegetation productivity driven primarily by rate not duration of carbon uptake. *Nature Climate Change*, (pp. 1–9). doi:10.1038/s41558-025-02311-3.

Liu, Z., Kimball, J. S., Ballantyne, A. P., Parazoo, N. C., Wang, W. J., Bastos, A., Madani, N., Natali, S. M., Watts, J. D., Rogers, B. M. et al. (2022). Respiratory loss during late-growing season determines the net carbon dioxide sink in northern permafrost regions. *Nature Communications*, *13*, 5626. doi:10.1038/s41467-022-33293-x.

Liu, Z. et al. (2020). Increased high-latitude photosynthetic carbon gain offset by respiration carbon loss during an anomalous warm winter to spring transition. *Global Change Biology*, *26*, 682–696. doi:10.1111/gcb.14863.

Liu, Z. et al. (2024). Seasonal CO_2 amplitude in northern high latitudes. *Nature Reviews Earth & Environment*, *5*, 802–817. doi:10.1038/s43017-024-00600-7.

Louis, J.-F. (1979). A parametric model of vertical eddy fluxes in the atmosphere. *Boundary-Layer Meteorology*, *17*, 187–202. doi:10.1007/BF00117978.

Luo, X., & Keenan, T. F. (2022). Tropical extreme droughts drive long-term increase in atmospheric CO_2 growth rate variability. *Nature communications*, *13*, 1193. doi:10.1038/s41467-022-28824-5.

Mahecha, M. D. et al. (2026). Accelerated north–east shift of the global green wave trajectory. *Proceedings of the National Academy of Sciences*, *123*, e2515835123. doi:10.1073/pnas.2515835123.

Manning, M. R. (1993). Seasonal Cycles in Atmospheric CO_2 Concentrations. (pp. 65–94). Berlin, Heidelberg: Springer Berlin Heidelberg.

Masson-Delmotte, V., Zhai, P., Pirani, A., Connors, S. L., Péan, C., Berger, S., Caud, N.,

Chen, Y., Goldfarb, L., Gomis, M. I. et al. (2021). Climate change 2021: the physical science basis. *Contribution of working group I to the sixth assessment report of the intergovernmental panel on climate change*, *2*, 2391. doi:10.1017/9781009157896.

Mekonnen, Z. A., Riley, W. J., Still, C. J., & Grant, R. F. (2025). Observations and modeling reveal that heatwaves reduce photosynthesis, plant carbon reserves, and net carbon uptake. *Environmental Research Letters*, *20*, 124079. doi:10.1088/1748-9326/ae2939.

Mercado, L., Bellouin, N., Sitch, S., Boucher, O., Huntingford, C., Wild, M., & Cox, P. (2009). Impact of changes in diffuse radiation on the global land carbon sink. *Nature*, *458*, 1014–7. doi:10.1038/nature07949.

Miller, S. M., & Michalak, A. M. (2020). The impact of improved satellite retrievals on estimates of biospheric carbon balance. *Atmospheric Chemistry and Physics*, *20*, 323–331. doi:10.5194/acp-20-323-2020.

Mirabel, A., Girardin, M., Metsaranta, J., Way, D., & Reich, P. (2023). Increasing atmospheric dryness reduces boreal forest tree growth. *Nature Communications*, *14*. doi:10.1038/s41467-023-42466-1.

Modak, A., & Mauritsen, T. (2021). The 2000–2012 Global Warming Hiatus More Likely With a Low Climate Sensitivity. *Geophysical Research Letters*, *48*, e2020GL091779. doi:10.1029/2020GL091779.

Monteil, G., Broquet, G., Scholze, M., Lang, M., Karstens, U., Gerbig, C., Koch, F.-T., Smith, N. E., Thompson, R. L., Luijkx, I. T. et al. (2020). The regional European atmospheric transport inversion comparison, EUROCOM: first results on European-wide terrestrial carbon fluxes for the period 2006–2015. *Atmospheric Chemistry and Physics*, *20*, 12063–12091. doi:10.5194/acp-20-12063-2020.

Moyano, F. E., Manzoni, S., & Chenu, C. (2013). Responses of soil heterotrophic respiration to moisture availability: An exploration of processes and models. *Soil Biology and Biochemistry*, *59*, 72–85. doi:10.1016/j.soilbio.2013.01.002.

Muccio, D., Keppel-Aleks, G., & Parazoo, N. (2025). Contrasting temperature sensitivity of boreal forest productivity in North America and Eurasia. *Journal of Geophysical Research: Biogeosciences*, *130*, e2024JG008634. doi:10.1029/2024JG008634.

Munassar, S., Monteil, G., Scholze, M., Karstens, U., Rödenbeck, C., Koch, F.-T., Totsche, K. U., & Gerbig, C. (2023). Why do inverse models disagree? A case study with two European CO_2 inversions. *Atmospheric Chemistry and Physics*, *23*, 2813–2828. doi:10.5194/acp-23-2813-2023.

Murayama, S., Higuchi, K., & Taguchi, S. (2007). Influence of atmospheric transport on the inter-annual variation of the CO_2 seasonal cycle downward zero-crossing. *Geophysical research letters*, *34*. doi:10.1029/2006GL028389.

Nakazawa, T., Ishizawa, M., Higuchi, K., & Trivett, N. B. (1997). Two curve

fitting methods applied to co$_2$ flask data. *Environmetrics: The official journal of the International Environmetrics Society*, *8*, 197–218. doi:10.1002/(SICI)1099-095X(199705)8:3<197::AID-ENV248>3.0.CO;2-C.

Nelson, J. A. et al. (2024). X-BASE: the first terrestrial carbon and water flux products from an extended data-driven scaling framework, FLUXCOM-X. *EGUsphere*, *2024*, 1–51. doi:10.5194/egusphere-2024-165.

Nemani, R. R., Keeling, C. D., Hashimoto, H., Jolly, W. M., Piper, S. C., Tucker, C. J., Myneni, R. B., & Running, S. W. (2003). Climate-driven increases in global terrestrial net primary production from 1982 to 1999. *science*, *300*, 1560–1563. doi:10.1126/science.1082750.

Nissan, A., Alcolombri, U., Peleg, N., Galili, N., Jimenez-Martinez, J., Molnar, P., & Holzner, M. (2023). Global warming accelerates soil heterotrophic respiration. *Nature Communications*, *14*, 3452. doi:10.1038/s41467-023-38981-w.

Niu, S. et al. (2024). Temperature responses of ecosystem respiration. *Nature Reviews Earth & Environment*, *5*, 559–571. doi:10.1038/s43017-024-00569-3.

O'Sullivan, M., Spracklen, D. V., Batterman, S. A., Arnold, S. R., Gloor, M., & Buermann, W. (2019). Have synergies between nitrogen deposition and atmospheric CO_2 driven the recent enhancement of the terrestrial carbon sink? *Global Biogeochemical Cycles*, *33*, 163–180.

Pallandt, M. M., Jung, M., Arndt, K., Natali, S. M., Rogers, B. M., Virkkala, A.-M., & Göckede, M. (2024). High-latitude eddy covariance temporal network design and optimization. *Journal of Geophysical Research: Biogeosciences*, *129*, e2024JG008406. doi:10.1029/2024JG008406.

Palmer, P. I., Feng, L., Baker, D., Chevallier, F., Bösch, H., & Somkuti, P. (2019). Net carbon emissions from African biosphere dominate pan-tropical atmospheric CO_2 signal. *Nature communications*, *10*, 3344. doi:10.1038/s41467-019-11097-w.

Pandey, S., Miller, J. B., Basu, S., Liu, J., Weir, B., Byrne, B., Chevallier, F., Bowman, K. W., Liu, Z., Deng, F. et al. (2024). Toward low-latency estimation of atmospheric CO_2 growth rates using satellite observations: Evaluating sampling errors of satellite and in situ observing approaches. *AGU Advances*, *5*, e2023AV001145. doi:10.1029/2023AV001145.

Parazoo, N., Denning, A., Berry, J., Wolf, A., Randall, D., Kawa, S., Pauluis, O., & Doney, S. C. (2011). Moist synoptic transport of CO_2 along the mid-latitude storm track. *Geophysical Research Letters*, *38*. doi:10.1029/2011GL047238.

Parazoo, N. C., Denning, A. S., Kawa, S. R., Corbin, K. D., Lokupitiya, R. S., & Baker, I. T. (2008). Mechanisms for synoptic variations of atmospheric CO_2 in North America, South America and Europe. *Atmospheric Chemistry and Physics*, *8*, 7239–7254. doi:10.5194/acp-8-7239-2008.

Park, H., Jeong, S.-J., Ho, C.-H., Park, C.-E., & Kim, J. (2018). Slowdown of spring green-up advancements in boreal forests. *Remote Sensing of Environment*, *217*, 191–202. doi:10.1016/j.rse.2018.08.012.

Park, T., Chen, C., Macias-Fauria, M., Tømmervik, H., Choi, S., Winkler, A., Bhatt, U. S., Walker, D. A., Piao, S., Brovkin, V., Nemani, R. R., & Myneni, R. B. (2019). Changes in timing of seasonal peak photosynthetic activity in northern ecosystems. *Global Change Biology*, *25*, 2382–2395. doi:10.1111/gcb.14638.

Park, T., Ganguly, S., Tømmervik, H., Euskirchen, E. S., Høgda, K.-A., Karlsen, S. R., Brovkin, V., Nemani, R. R., & Myneni, R. B. (2016). Changes in growing season duration and productivity of northern vegetation inferred from long-term remote sensing data. *Environmental Research Letters*, *11*, 084001. doi:10.1088/1748-9326/11/8/084001.

Parmentier, F.-J. W., Van Der Molen, M., Van Huissteden, J., Karsanaev, S., Kononov, A., Suzdalov, D., Maximov, T., & Dolman, A. (2011). Longer growing seasons do not increase net carbon uptake in the northeastern Siberian tundra. *Journal of Geophysical Research: Biogeosciences*, *116*. doi:10.1029/2011JG001653.

Patra, P. K. et al. (2008). TransCom model simulations of hourly atmospheric CO_2: Analysis of synoptic-scale variations for the period 2002–2003. *Global Biogeochemical Cycles*, *22*. doi:10.1029/2007GB003081.

Peng, J., Xie, S., Tang, J., Liao, J., Chen, C., Sun, C., Wang, Y., Zhou, Q., Yu, G., & Niu, S. (2025). Global Evidence of the Unimodal Response of Ecosystem Respiration to Soil Moisture. *Advanced Science*, (p. e09753). doi:10.1002/advs.202509753.

Peters, W., Miller, J. B., Whitaker, J., Denning, A. S., Hirsch, A., Krol, M. C., Zupanski, D., Bruhwiler, L., & Tans, P. P. (2005). An ensemble data assimilation system to estimate CO_2 surface fluxes from atmospheric trace gas observations. *Journal of Geophysical Research: Atmospheres*, *110*. doi:10.1029/2005JD006157.

Peters, W. et al. (2018). Increased water-use efficiency and reduced CO_2 uptake by plants during droughts at a continental scale. *Nature Geoscience*, *11*, 744–748. doi:10.1038/s41561-018-0212-7.

Peylin, P., Law, R., Gurney, K., Chevallier, F., Jacobson, A., Maki, T., Niwa, Y., Patra, P., Peters, W., Rayner, P. et al. (2013). Global atmospheric carbon budget: results from an ensemble of atmospheric CO_2 inversions. *Biogeosciences*, *10*, 6699–6720. doi:10.1002/advs.202509753.

Piao, S. et al. (2008). Net carbon dioxide losses of northern ecosystems in response to autumn warming. *Nature*, *451*, 49–52. doi:10.1038/nature06444.

Piao, S., Friedlingstein, P., Ciais, P., Peylin, P., Zhu, B., & Reichstein, M. (2009). Footprint of temperature changes in the temperate and boreal forest carbon balance. *Geophysical Research Letters*, *36*. doi:10.1029/2009GL037381.

Piao, S., Friedlingstein, P., Ciais, P., Viovy, N., & Demarty, J. (2007). Growing season extension and its impact on terrestrial carbon cycle in the northern hemisphere over the past 2 decades. *Global Biogeochemical Cycles*, *21*. doi:10.1029/2006GB002888.

Piao, S., Liu, Q., Chen, A., Janssens, I. A., Fu, Y., Dai, J., Liu, L., Lian, X., Shen, M., & Zhu, X. (2019). Plant phenology and global climate change: Current progresses and challenges. *Global Change Biology*, *25*, 1922–1940. doi:10.1111/gcb.14619.

Piao, S. et al. (2017). Weakening temperature control on the interannual variations of spring carbon uptake across northern lands. *Nature Climate Change*, *7*, 359–363. doi:10.1038/nclimate3277.

Piao, S., Liu, Z., Wang, Y., Ciais, P., Yao, Y., Peng, S., Chevallier, F., Friedlingstein, P., Janssens, I. A., Peñuelas, J., Sitch, S., & Wang, T. (2018). On the causes of trends in the seasonal amplitude of atmospheric co_2. *Global Change Biology*, *24*, 608–616. doi:10.1111/gcb.13909.

Pickers, P. A., & Manning, A. C. (2015). Investigating bias in the application of curve fitting programs to atmospheric time series. *Atmospheric Measurement Techniques*, *8*, 1469–1489. doi:10.5194/amt-8-1469-2015.

Platt, S. M. et al. (2022). Atmospheric composition in the European Arctic and 30 years of the Zeppelin Observatory, Ny-Ålesund. *Atmospheric Chemistry and Physics*, *22*, 3321–3369. doi:10.5194/acp-22-3321-2022.

Prentice, I. C., Farquhar, G. D., Fasham, M. J. R., Goulden, M. L., Heimann, M., Jaramillo, V. J., Kheshgi, H. S., Le Quéré, C., Scholes, R. J., & Wallace, D. W. R. (2001). The carbon cycle and atmospheric carbon dioxide. In J. T. Houghton, Y. Ding, D. J. Griggs et al. (Eds.), *Climate Change 2001: The Scientific Basis. Contribution of Working Group I to the Third Assessment Report of the Intergovernmental Panel on Climate Change* (pp. 183–237). Cambridge: Cambridge University Press.

Qu, G., Zhou, J., Shi, Y., Yang, Y., Su, M., Wu, W., & Zhou, Z. (2025). Assessment of the Impacts of Different Carbon Sources and Sinks on Atmospheric CO_2 Concentrations Based on GEOS-Chem. *Remote Sensing*, *17*, 1009. doi:10.3390/rs17061009.

Quan, Q., Tian, D., Luo, Y., Zhang, F., Crowther, T., Zhu, K., Zhou, Q., & Niu, S. (2019). Water scaling of ecosystem carbon cycle feedback to climate warming. *Science Advances*, *5*, eaav1131. doi:10.1126/sciadv.aav1131.

Ramonet, M. et al. (2020). The fingerprint of the summer 2018 drought in Europe on ground-based atmospheric CO_2 measurements. *Philosophical Transactions of the Royal Society B: Biological Sciences*, *375*, 20190513. doi:10.1098/rstb.2019.0513.

Randerson, J. T., Field, C. B., Fung, I. Y., & Tans, P. P. (1999). Increases in early season ecosystem uptake explain recent changes in the seasonal cycle of atmospheric CO_2 at high northern latitudes. *Geophysical Research Letters*, *26*, 2765–2768. doi:10.1029/1999GL900500.

Randerson, J. T., Thompson, M. V., Conway, T. J., Fung, I. Y., & Field, C. B. (1997). The contribution of terrestrial sources and sinks to trends in the seasonal cycle of atmospheric carbon dioxide. *Global biogeochemical cycles*, *11*, 535–560. doi:10.1029/97GB02268.

Raymond, P. A., & Cole, J. J. (2003). Increase in the export of alkalinity from North America's largest river. *Science*, *301*, 88–91. doi:10.1126/science.1083788.

Reichstein, M. et al. (2005). On the separation of net ecosystem exchange into assimilation and ecosystem respiration: review and improved algorithm. *Global Change Biology*, *11*, 1424–1439. doi:10.1111/j.1365-2486.2005.001002.x.

Riany, Welder, Grant, Kellou, Klönne, & Hare (2024). *The role of northern forests in limiting warming to 1.5°C*. Technical Report, .

Richardson, A. D. et al. (2012). Terrestrial biosphere models need better representation of vegetation phenology: results from the north american carbon program site synthesis. *Global Change Biology*, *18*, 566–584. doi:10.1111/j.1365-2486.2011.02562.x.

Rödenbeck, C., Houweling, S., Gloor, M., & Heimann, M. (2003). CO_2 flux history 1982–2001 inferred from atmospheric data using a global inversion of atmospheric transport. *Atmospheric Chemistry and Physics*, *3*, 1919–1964. doi:10.5194/acp-3-1919-2003.

Rödenbeck, C., Zaehle, S., Keeling, R., & Heimann, M. (2018). How does the terrestrial carbon exchange respond to inter-annual climatic variations? A quantification based on atmospheric CO_2 data. *Biogeosciences*, *15*, 2481–2498. doi:10.5194/bg-15-2481-2018.

Russell, G. L., & Lerner, J. A. (1981). A new finite-differencing scheme for the tracer transport equation. *Journal of Applied Meteorology (1962-1982)*, (pp. 1483–1498). doi:10.1175/1520-0450(1981)020<1483:ANFDSF>2.0.CO;2.

Schimel, D., Stephens, B. B., & Fisher, J. B. (2015). Effect of increasing CO_2 on the terrestrial carbon cycle. *Proceedings of the National Academy of Sciences*, . doi:10.1073/pnas.1407302112.

Schindlbacher, A., Wunderlich, S., Borken, W., Kitzler, B., Zechmeister-Boltenstern, S., & Jandl, R. (2012). Soil respiration under climate change: prolonged summer drought offsets soil warming effects. *Global Change Biology*, *18*, 2270–2279. doi:10.1111/j.1365-2486.2012.02696.x.

Schuh, A. E., Jacobson, A. R., Basu, S., Weir, B., Baker, D., Bowman, K., Chevallier, F., Crowell, S., Davis, K. J., Deng, F. et al. (2019). Quantifying the impact of atmospheric transport uncertainty on CO_2 surface flux estimates. *Global biogeochemical cycles*, *33*, 484–500. doi:10.1029/2018GB006086.

Schuldt, K. N. et al. (2023). Multi-laboratory compilation of atmospheric carbon dioxide data for the period 1957-2022; obspack_co2_1_globalviewplus_v9.1_2023-12-08. doi:10.25925/20231201.

Schuur, E. A. G. et al. (2015). Climate change and the permafrost carbon feedback. *Nature*, *520*, 171–179. doi:10.1038/nature14338.

Sharma, S., Andrews, E., Barrie, L., Ogren, J., & Lavoué, D. (2006). Variations and sources of the equivalent black carbon in the high Arctic revealed by long-term observations at Alert and Barrow: 1989–2003. *Journal of Geophysical Research: Atmospheres*, *111*. doi:10.1029/2005JD006581.

Shen, M. et al. (2022). Plant phenology changes and drivers on the Qinghai–Tibetan Plateau. *Nature Reviews Earth & Environment*, *3*, 633–651. doi:10.1038/s43017-022-00317-5.

Shi, S., Yang, P., Vrieling, A., & van der Tol, C. (2025). Vegetation optimal temperature modulates global vegetation season onset shifts in response to warming climate. *Communications Earth & Environment*, *6*, 203. doi:10.1038/s43247-025-02186-4.

Sippel, S., Reichstein, M., Ma, X., Mahecha, M. D., Lange, H., Flach, M., & Frank, D. (2018). Drought, heat, and the carbon cycle: a review. *Current Climate Change Reports*, *4*, 266–286. doi:10.1007/s40641-018-0103-4.

Sitch, S., O'sullivan, M., Robertson, E., Friedlingstein, P., Albergel, C., Anthoni, P., Arneth, A., Arora, V. K., Bastos, A., Bastrikov, V. et al. (2024). Trends and drivers of terrestrial sources and sinks of carbon dioxide: An overview of the trendy project. *Global Biogeochemical Cycles*, *38*, e2024GB008102. doi:10.1029/2024GB008102.

Stinziano, J. R., & Way, D. A. (2017). Autumn photosynthetic decline and growth cessation in seedlings of white spruce are decoupled under warming and photoperiod manipulations. *Plant, Cell & Environment*, *40*, 1296–1316. doi:10.1111/pce.12917.

Stohl, A. (2006). Characteristics of atmospheric transport into the Arctic troposphere. *Journal of Geophysical Research: Atmospheres*, *111*. doi:10.1029/2005JD006888.

Sun, Z., Wang, X., Yamamoto, H., Tani, H., Zhong, G., Yin, S., & Guo, E. (2018). Spatial pattern of GPP variations in terrestrial ecosystems and its drivers: Climatic factors, CO_2 concentration and land-cover change, 1982–2015. *Ecological Informatics*, *46*, 156–165. doi:10.1016/j.ecoinf.2018.06.006.

Taguchi, S., Murayama, S., & Higuchi, K. (2003). Sensitivity of inter-annual variation of CO_2 seasonal cycle at Mauna Loa to atmospheric transport. *Tellus B: Chemical and Physical Meteorology*, *55*, 547–554.

Tans, P. P. K. W. T., Elliott, W., & Conway, T. J. (1989). Background Atmospheric CO_2 patterns from weekly flask samples at Barrow, Alaska: Optimal signal recovery and error estimates, in The Statistical Treatment of CO_2 Data Records. *NOAA Technical Memorandum*, *173,131*, 112–123.

Taylor, K., Ronald, S., & Meehl, G. (2011). An Overview of CMIP5 and the Experiment Design. *Bulletin of the American Meteorological Society*, *93*, 485–498.

doi:10.1175/BAMS-D-11-00094.1.

Thoning, K. W., Tans, P. P., & Komhyr, W. D. (1989). Atmospheric carbon dioxide at Mauna Loa Observatory: 2. Analysis of the NOAA GMCC data, 1974–1985. *Journal of Geophysical Research: Atmospheres*, *94*, 8549–8565. doi:10.1029/JD094iD06p08549.

Tiedtke, M. (1989). A comprehensive mass flux scheme for cumulus parameterization in large-scale models. *Monthly weather review*, *117*, 1779–1800. doi:10.1175/1520-0493(1989)117<1779:ACMFSF>2.0.CO;2.

Tran, D. A., Gerbig, C., Rödenbeck, C., & Zaehle, S. (2024). Interannual variations in Siberian carbon uptake and carbon release period. *Atmospheric Chemistry and Physics*, *24*, 8413–8440. doi:10.5194/acp-24-8413-2024.

Trivett, N. B. A., K, H., & S., S. (1989). Trends and seasonal cycles of atmospheric CO_2 over Alert, Sable Island, and Cape St. James, as analyzed by forward stepwise regression technique. *NOAA Technical Memorandum ERL ARL- 173, Air Resources Laboratory, Silver Spring, Maryland, USA*, *173,131*, 27–42.

Tunved, P., Ström, J., & Krejci, R. (2013). Arctic aerosol life cycle: linking aerosol size distributions observed between 2000 and 2010 with air mass transport and precipitation at Zeppelin station, Ny-Ålesund, Svalbard. *Atmospheric Chemistry and Physics*, *13*, 3643–3660. doi:10.5194/acp-13-3643-2013.

Upton, S., Reichstein, M., Gans, F., Peters, W., Kraft, B., & Bastos, A. (2024). Constraining biospheric carbon dioxide fluxes by combined top-down and bottom-up approaches. *Atmospheric Chemistry and Physics*, *24*, 2555–2582. doi:10.5194/acp-24-2555-2024.

Vekuri, H., Tuovinen, J.-P., Kulmala, L., Papale, D., Kolari, P., Aurela, M., Laurila, T., Liski, J., & Lohila, A. (2023). A widely-used eddy covariance gap-filling method creates systematic bias in carbon balance estimates. *Scientific Reports*, *13*, 1720. doi:10.1038/s41598-023-28827-2.

Walker, X. J., Baltzer, J. L., Cumming, S. G., Day, N. J., Ebert, C., Goetz, S., Johnstone, J. F., Potter, S., Rogers, B. M., Schuur, E. A. G., Turetsky, M. R., & Mack, M. C. (2019). Increasing wildfires threaten historic carbon sink of boreal forest soils. *Nature*, *572*, 520–523. doi:10.1038/s41586-019-1474-y.

Walther, S., Besnard, S., Nelson, J. A., El-Madany, T. S., Migliavacca, M., Weber, U., Carvalhais, N., Ermida, S. L., Brümmer, C., Schrader, F. et al. (2022). A view from space on global flux towers by MODIS and Landsat: the FluxnetEO data set. *Biogeosciences*, *19*, 2805–2840. doi:10.5194/bg-19-2805-2022.

Wang, S., Zhang, Y., Ju, W., Chen, J. M., Ciais, P., Cescatti, A., Sardans, J., Janssens, I. A., Wu, M., Berry, J. A. et al. (2020). Recent global decline of CO_2 fertilization effects on vegetation photosynthesis. *Science*, *370*, 1295–1300. doi:10.1126/science.abb7772.

Wang, X., Liu, L., Piao, S., Janssens, I. A., Tang, J., Liu, W., Chi, Y., Wang, J.,

& Xu, S. (2014). Soil respiration under climate warming: differential response of heterotrophic and autotrophic respiration. *Global Change Biology*, *20*, 3229–3237. doi:10.1111/gcb.12620.

Wang, X., Sun, Z., Lu, S., & Zhang, Z. (2022). Comparison of Phenology Estimated From Monthly Vegetation Indices and Solar-Induced Chlorophyll Fluorescence in China. *Frontiers in Earth Science*, *10*. doi:10.3389/feart.2022.802763.

Wang, X., Xiao, J., Li, X., Cheng, G., Ma, M., Zhu, G., Altaf Arain, M., Andrew Black, T., & Jassal, R. S. (2019). No trends in spring and autumn phenology during the global warming hiatus. *Nature Communications*, *10*, 2389. doi:10.1038/s41467-019-10235-8.

Wang, Y., Sarmah, S., Singha, M., Chen, W., Ge, Y., Liang, L. L., Goswami, S., & Niu, S. (2024). Increasing optimum temperature of vegetation activity over the past four decades. *Earth's Future*, *12*, e2024EF004489. doi:10.1029/2024EF004489.

Watson, R. T., Noble, I. R., Bolin, B., Ravindranath, N. H., Verardo, D. J., & Dokken, D. J. (2000). *Land Use, Land-Use Change, and Forestry*. Cambridge, United Kingdom and New York, NY, USA: Cambridge University Press. A Special Report of the Intergovernmental Panel on Climate Change (IPCC). Summary for Policymakers also available from IPCC Secretariat, Geneva, Switzerland, 20 pp. Available in Arabic, Chinese, English, French, Spanish and Russian.

Wehr, R., & Saleska, S. (2015). An improved isotopic method for partitioning net ecosystem-atmosphere CO_2 exchange. *Agricultural and Forest Meteorology*, *214*, 515–531. doi:10.1016/j.agrformet.2015.09.009.

Wenzel, S., Cox, P. M., Eyring, V., & Friedlingstein, P. (2014). Emergent constraints on climate-carbon cycle feedbacks in the CMIP5 Earth system models. *Journal of Geophysical Research: Biogeosciences*, *119*, 794–807. doi:10.1002/2013JG002591.

White, M. A., & Nemani, R. R. (2003). Canopy duration has little influence on annual carbon storage in the deciduous broad leaf forest. *Global Change Biology*, *9*, 967–972. doi:10.1046/j.1365-2486.2003.00585.x.

Wolf, S., & Paul-Limoges, E. (2023). Drought and heat reduce forest carbon uptake. *Nature Communications*, *14*, 6217. doi:10.1038/s41467-023-41854-x.

van der Woude, A. et al. (2025a). Simulated CO_2 mole fractions from 14 atmospheric inversions in GCB2025. doi:10.18160/4MNF-W5DR.

van der Woude, A. et al. (2025b). A top-down view of global and regional carbon budgets from an ensemble of atmospheric inversions. . doi:10.22541/essoar.175376114.45413910/v1 working paper or preprint.

van der Woude, A. M. et al. (2023a). Near-real-time CO_2 fluxes from CarbonTracker Europe for high-resolution atmospheric modeling. *Earth System Science Data*, *15*, 579–605. doi:10.5194/essd-15-579-2023.

van der Woude, A. M. et al. (2023b). Temperature extremes of 2022 reduced carbon uptake by forests in Europe. *Nature Communications*, *14*, 6218. doi:10.1038/s41467-023-41851-0.

Wu, C. et al. (2012). Interannual and spatial impacts of phenological transitions, growing season length, and spring and autumn temperatures on carbon sequestration: A North America flux data synthesis. *Global and Planetary Change*, *92-93*, 179–190. doi:10.1016/j.gloplacha.2012.05.021.

Xiong, T., Du, S., Zhang, H., & Zhang, X. (2024). Decreasing temperature sensitivity of spring phenology decelerates the advance of spring phenology in northern temperate and boreal forests. *Ecological Indicators*, *161*, 111983. doi:10.1016/j.ecolind.2024.111983.

Yan, Z., Bond-Lamberty, B., Todd-Brown, K. E., Bailey, V. L., Li, S., Liu, C., & Liu, C. (2018). A moisture function of soil heterotrophic respiration that incorporates microscale processes. *Nature Communications*, *9*, 2562. doi:10.1038/s41467-018-04971-6.

Zani, D., Crowther, T. W., Mo, L., Renner, S. S., & Zohner, C. M. (2020). Increased growing-season productivity drives earlier autumn leaf senescence in temperate trees. *Science*, *370*, 1066–1071. doi:10.1126/science.abd8911.

Zeng, L., Wardlow, B. D., Xiang, D., Hu, S., & Li, D. (2020). A review of vegetation phenological metrics extraction using time-series, multispectral satellite data. *Remote Sensing of Environment*, *237*, 111511. doi:10.1016/j.rse.2019.111511.

Zeng, Z. et al. (2023). Increasing meteorological drought under climate change reduces terrestrial ecosystem productivity and carbon storage. *One Earth*, *6*, 1326–1339. doi:10.1016/j.oneear.2023.09.007.

Zhao, B., Zhuang, Q., Shurpali, N., Köster, K., Berninger, F., & Pumpanen, J. (2021). North American boreal forests are a large carbon source due to wildfires from 1986 to 2016. *Scientific Reports*, *11*, 7723. doi:10.1038/s41598-021-87343-3.

Zhao, C., & Zhu, W. (2025). Vegetation structure and phenology primarily shape the spatiotemporal pattern of ecosystem respiration. *Communications Earth & Environment*, *6*, 249. doi:10.1038/s43247-025-02240-1.

Zhao, F., & Zeng, N. (2014). Continued increase in atmospheric CO_2 seasonal amplitude in the 21st century projected by the CMIP5 Earth system models. *Earth System Dynamics*, *5*, 423–439. doi:10.5194/esd-5-423-2014.

Zheng, J., Xu, X., & Jia, G. (2022). Effects of shifting spring phenology on growing season carbon uptake in high latitudes. *Journal of Geophysical Research: Biogeosciences*, *127*, e2022JG006900. doi:10.1029/2022JG006900.

Zhou, L., Tucker, C. J., Kaufmann, R. K., Slayback, D., Shabanov, N. V., & Myneni, R. B. (2001). Variations in northern vegetation activity inferred from satellite data of vegetation index during 1981 to 1999. *Journal of Geophysical Research: Atmospheres*,

106, 20069–20083. doi:10.1029/2000JD000115.

Zhou, L., Wang, Y., Jia, Q., & Zhou, G. (2021). Increasing temperature shortened the carbon uptake period and decreased the cumulative net ecosystem productivity in a maize cropland in northeast china. *Field Crops Research*, *267*, 108150. doi:10.1016/j.fcr.2021.108150.

Zhou, X., Geng, X., Yin, G., Hänninen, H., Hao, F., Zhang, X., & H. Fu, Y. (2020). Legacy effect of spring phenology on vegetation growth in temperate china. *Agricultural and Forest Meteorology*, *281*, 107845. doi:10.1016/j.agrformet.2019.107845.

Zhu, W., Chen, G., Jiang, N., Liu, J., & Mou, M. (2013). Estimating carbon flux phenology with satellite-derived land surface phenology and climate drivers for different biomes: A synthesis of ameriflux observations. *PLOS ONE*, *8*, 1–10. doi:10.1371/journal.pone.0084990.

Zhu, W., Tian, H., Xu, X., Pan, Y., Chen, G., & Lin, W. (2012). Extension of the growing season due to delayed autumn over mid and high latitudes in North America during 1982–2006. *Global Ecology and Biogeography*, *21*, 260–271. doi:10.1111/j.1466-8238.2011.00675.x.

Zou, H., Chen, J., Shao, C., Dong, G., Duan, M., Zhu, Q., & Li, X. (2022). Model Selection for Ecosystem Respiration Needs to Be Site Specific: Lessons from Grasslands on the Mongolian Plateau. *Land*, *11*. doi:10.3390/land11010087.

Netherlands Research School for the
Socio-Economic and Natural Sciences of the Environment

D I P L O M A

for specialised PhD training

The Netherlands research school for the
Socio-Economic and Natural Sciences of the Environment
(SENSE) declares that

Theertha Kariyathan

born on 08th October 1996 in Kochi, India

has successfully fulfilled all requirements of the
educational PhD programme of SENSE.

Wageningen, 19 November 2026

SENSE coordinator PhD education

Dr Ir Peter Vermeulen

The SENSE Director

Dr Jampel Dell'Angelo

The SENSE Research School declares that **Theertha Kariyathan** has successfully fulfilled all requirements of the educational PhD programme of SENSE with a workload of 42.9 EC, including the following activities:

SENSE PhD Courses

- A2 Research in context activity: Organizing a three day international webinar 'Land–Atmosphere CO_2 Dynamics: From Measurements to Models' (2024)

Other PhD and Advanced MSc Courses

- Biogeochemical cycles in the Earth System-an Overview, Max Planck Institute für Biogeochemistry (MPI-Bgc) (2020)
- Terrestrial Biosphere, MPI-Bgc (2020)
- Eddy covariance, MPI-Bgc, Germany (2020)
- R course advance modules, MPI-Bgc, Germany (2020)
- Applied statistics and data analysis, MPI-Bgc, Germany (2020)
- Python, MPI-Bgc, Germany (2021)
- Modelling and numerical techniques, MPI-Bgc, Germany (2021)
- Remote sensing, MPI-Bgc, Germany (2023)
- R data visualisation, MPI-Bgc, Germany (2023)
- Atmosphere, Ocean and Land, MPI-Bgc (2023)
- ICOS Summer School, ICOS (2023)

General Skill courses

- Academic writing – How to create good text, MPI-Bgc (2021)
- Transition from scientist to Data scientist, MPI-Bgc (2023)

Management and Organisational activities

- Department PhD representative at Max Planck Institute(2022-2023)

Oral Presentations

- *The use of multi-tracer flask-measurements to understand changes in the land-surface processes*. EGU 2021, 27 April 2021, Online,
- *Constraining the uncertainty in CO_2 seasonal cycle metrics by residual bootstrapping*. EGU 2022, 25 May 2022, Vienna, Austria
- *Estimating start and end of carbon uptake period with reduced uncertainty from time-series of atmospheric CO_2 concentrations*. AGU 2021, 13 December 2021, Online,
- *Robust estimation of the carbon uptake period based on time series of atmospheric CO_2*. ICOS 2022, 14 September 2022, Online,

The presented research was financially supported by funding from the International Max Planck Research School for Global Biogeochemical Cycles (IMPRS-gBGC).

Cover design by Ishwar Venugopal
Cover photo by Eldho Elias

